Karlsruhe Institute of Technology

Simulation of charge transport in amorphous organic semiconductors

Zur Erlangung des akademischen Grades eines

DOKTORS DER NATURWISSENSCHAFTEN

(Dr. rer. nat.)

von der KIT-Fakultät für Chemie und Biowissenschaften
des Karlsruher Instituts für Technologie (KIT)

genehmigte

DISSERTATION

von

Samaneh Inanlou

1. Referent: Prof. Dr. Marcus Elstner
2. Referent: Prof. Dr. Wolfgang Wenzel
Tag der mündlichen Prüfung: 20/07/2022

Karlsruher Institut für Technologie
Fakultät für Chemie und Biowissenschaften
Kaiserstraße 12
76131 Karlsruhe

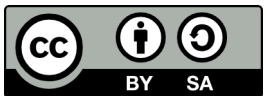

Abstract

This thesis consists of 5 chapters: In Chapter 1, we provide an introduction to OLEDs. In Chapter 2, we briefly discuss the basics of quantum chemical methods and provide an overview of Molecular Dynamics.

Simulation of charge transport in amorphous organic semiconductors requires the analysis of the electronic structures. Therefore, in Chapter 3 we provide a fundamental background describing the mechanism of charge transport in organic semiconductors. In particular, we focus more on amorphous organic semiconductors which is a primary focus of my research. The way we model charge transfer in organic semiconductors is based on charge hopping transfer which occurs at a certain rate. These rates can be calculated based on the Marcus rate theory. Therefore, we briefly describe the Marcus rate theory and also discuss some of the important properties of organic semiconductors.

In Chapter 4, we simulate absorption spectra of 4,4-Bis(carbazol-9-yl)-2,2-biphenyl (CBP), which is widely used as a host material in phosphorescent organic light-emitting diodes (PhOLEDs), using the efficient time-dependent long-range corrected tight binding density functional theory (TD-LC-DFTB). The accuracy of the condensed-phase absorption spectra computed using the structures obtained from classical molecular dynamics (MD) and quantum mechanical/molecular mechanical (QM/MM) simulations is examined by comparison with the experimental absorption spectrum. We observe that there is a good agreement between the CC2, GW-BSE, and TD-LC-DFTB results, indicating TD-LC-DFTB is an accurate and robust method for calculating the excitation energies of CBP. The good agreement between computed and experimental absorption spectra is therefore an indicator for the structural model developed. Concerning dynamic disorder, we find that molecular changes occur on long timescales in the nanosecond-regime, which requires the use of fast computation approaches to reach convergence. Furthermore, in order to see how dihedral angles affect the excitation energies, we compute vertical excitation energies and consequently obtain absorption spectra for different dihedral angles.

Finally, in Chapter 5 which is still an ongoing project, we study the impact of molecular structures and dynamical fluctuations on the charge transfer rate constant. The research question of interest is whether saving snapshots of a molecule from QM/MM simulations and consequently computing electronic coupling using a static method can be a reliable approach for calculating the rate constant. In addition, we discuss the critical timescales which play an important role in charge transfer reactions with fluctuating behavior. This topic is very well studied in biological systems and we aim to investigate it in amorphous organic semiconductors.

Zusammenfassung

Diese Arbeit besteht aus 5 Kapiteln: In Kapitel 1 wird eine Einführung zu OLEDs gegeben. In Kapitel 2 werden kurz die Grundlagen quantenchemischer Methoden erörtert und ein Überblick über die Molekulardynamik gegeben.

Die Simulation des Ladungstransports in amorphen organischen Halbleitern erfordert die Analyse der elektronischen Strukturen. Daher wird in Kapitel 3 der theoretische Hintergrund zum Mechanismus des Ladungstransports. Dabei konzentrieren wir uns insbesondere auf amorphe organische Halbleiter, die einen Schwerpunkt meiner Forschung darstellen. Die Art und Weise, wie wir den Ladungstransport in organischen Halbleitern modellieren, basiert auf dem sogenannten charge hopping transfer, der mit einer bestimmten Rate erfolgt. Diese Raten können auf der Grundlage der Marcus-Raten-Theorie berechnet werden. Daher beschreiben wir kurz die Marcus-Raten-Theorie und erörtern einige der wichtigsten Eigenschaften organischer Halbleiter.

In Kapitel 4 simulieren wir die Absorptionsspektren von 4,4-Bis(carbazol-9-yl)-2,2-biphenyl (CBP), das weithin als Wirtsmaterial in phosphoreszierenden organischen Leuchtdioden (PhOLEDs) verwendet wird, mit Hilfe der effizienten zeitabhängigen long-range corrected Dichtefunktionaltheorie (TD-LC-DFTB). Die Genauigkeit der Absorptionsspektren in der kondensierten Phase, die mit Hilfe der aus klassischen Molekulardynamik- (MD) und quantenmechanischen/molekularmechanischen (QM/MM) Simulationen gewonnenen Strukturen berechnet wurden, wird durch Vergleich mit dem experimentellen Absorptionsspektrum untersucht. Wir stellen fest, dass es eine gute Übereinstimmung zwischen den CC2-, GW-BSE- und TD-LC-DFTB-Ergebnissen gibt, was darauf hinweist, dass TD-LC-DFTB eine genaue und robuste Methode zur Berechnung der Anregungsenergien von CBP ist. Die gute Übereinstimmung zwischen berechneten und experimentellen Absorptionsspektren ist daher ein Indikator für das entwickelte Strukturmodell. Hinsichtlich der dynamischen Unordnung stellen wir fest, dass die molekularen Veränderungen im Nanosekunden-Regime auf langen Zeitskalen stattfinden, was den Einsatz von schnellen Berechnungsansätzen erfordert, um Konvergenz zu erreichen. Um zu sehen, wie sich Flächenwinkel auf die Anregungsenergien auswirken, berechnen wir vertikale Anregungsenergien und erhalten so Absorptionsspektren für verschiedene Flächenwinkel.

Schließlich untersuchen wir in Kapitel 5, das noch ein laufendes Projekt ist, den Einfluss von Molekülstrukturen und dynamischen Fluktuationen auf die Ladungstransferratenkonstante. Die Forschungsfrage, die uns interessiert, ist, ob die Speicherung von Momentaufnahmen eines Moleküls aus QM/MM-Simulationen und die anschließende Berechnung der elektronischen Kopplung mit einer statischen Methode ein zuverlässiger Ansatz für die Berechnung der Geschwindigkeitskonstante sein kann. Darüber hinaus diskutieren wir

die kritischen Zeitskalen, die bei Ladungstransferreaktionen mit fluktuierendem Verhalten eine wichtige Rolle spielen. Dieses Thema ist in biologischen Systemen sehr gut untersucht und wir wollen es in amorphen organischen Halbleitern untersuchen.

Acknowledgement

First and foremost, I would like to express my special appreciation and thanks to my advisor Prof. Marcus Elstner. I am very grateful to him for his unwavering support throughout the past 3 years, for his patience and understanding while I was going through tough times of my Ph.D. life and for his drive to push me to be a better researcher and person.

I am also very grateful to Dr. Weiwei Xie who has been a great mentor, reliable support, and someone to go to when I faced challenges during my Ph.D. Weiwei always made himself available for help and advice to me. I have learned something insightful through every interaction with him during my Ph.D..

I would also like to thank Prof. Wolfgang Wenzel, Prof. Wim Klaper and Prof. Sebastian Höfener for all the discussions and conversations we had in our P2 monthly meetings during my Ph.D. which have helped me to gain an improved perspective on research problems. I would like to extend my sincere thanks to my committee members, Prof. Marcus Elstner, Prof. Wolfgang Wenzel, Prof. Hans-Achim Wagenknecht and Prof. Annie K. Powell for serving on my Ph.D. committee and for their valuable insights and questions. I also wish to show my appreciation for my collaborators, Rodrigo, etc. for receiving their perspective, and feedback on technical, writing, and presentation aspects while we were working on excited states properties of organic semiconductors.

Other huge thanks to my colleagues Monja, Deepak and Philipp, and all my KIT friends, for their friendship, pleasant conversations and making some of my best memories during the past few years.

I would like to express my deepest gratitude to my husband and family for their unrelenting support and everlasting love during the ups and downs of my Ph.D. journey.

Contents

Abstract . . . . . **i**

Zusammenfassung . . . . . **iii**

1 Introduction **1**

2 Computational Toolbox **3**
2.1 Born-Oppenheimer approximation 4
2.2 Quantum mechanical Method 5
2.2.1 Density Functional Theory (DFT) 5
2.3 Density function approximation 8
2.3.1 Time-dependent density functional theory (TD-DFT) 11
2.3.2 Density Functional Tight binding (DFTB) 12
2.3.3 Time-dependent density functional bight binding (TD-DFTB) . . 15
2.3.4 Long-range corrected DFTB (LC-DFTB) 16
2.4 Molecular Dynamics Simulation 17
2.4.1 Molecular Mechanics 17
2.4.2 Verlet integration method 18
2.5 Quantum Mechanics/Molecular Mechanics 19

3 Fundamentals of charge transfer in organic semiconductors **21**
3.1 Electronic structure of OSCs and OLEDs 21
3.2 Charge hopping in amorphous organic materials 23
3.3 Marcus theory of electron transfer 25
3.3.1 Electronic coupling 26
3.3.2 Reorganization energy 27
3.3.3 Site energy 28

4 Understanding excited state properties of host materials in OLEDs **31**
4.1 Introduction 31
4.2 Methodology 32
4.2.1 Benchmark of TD-LC-DFTB 32
4.2.2 Molecular dynamics simulations 34
4.3 Results 37
4.3.1 Bond length alternation and excitation energies 37
4.3.2 Absorption spectra in gas phase 41
4.3.3 Absorption spectra in condensed phase using force field geometries 43
4.4 Conclusions 53

5 Effects of dynamic disorder on eletron transfer for OSCs **55**
5.1 Introduction 55
5.2 Computational Details 59
5.3 Results and Discussion 60
5.3.1 Site energy (ϵ_i) 60
5.3.2 Electronic coupling (T_{DA}) 62
5.4 Conclusion and outlook 68

Bibliography **69**

List of Figures **79**

List of Tables **83**

6 Appendix **85**
6.1 Site energy (ϵ_i) 85
6.2 Electronic coupling (T_{DA}) 88
6.3 Instantaneous Marcus rate 95

1 Introduction

Over the last few decades, there has been a significant increase in popularity of electronic components made from amorphous solids or crystalline organic materials. These amorphous solids or crystalline organic materials are regarded as organic semiconductors (OSCs) [1, 2]. OSCs are made from hydrogen, carbon and some other hetero-atoms such as oxygen, sulfur, nitrogen. These materials have properties which are generally associated with semiconductors. They transport energy and charge when grown as a thin film which is designed with suitable optical band gap. The semiconductors materials are commonly used in organic light emitting diodes (OLEDs) [3, 4], organic photovoltaic devices (OPVs) [5, 6], and organic field effect transistors (OFETs) [7, 8], due to their sufficient high degree of conductivity, which is result from the injection of charge at the electrode or dissociation of photogenerated electrons.

OLEDs are considered as highly efficient light sources which are used in various electronic devices such as displays in smart watches, mobile phones and flat screen televisions. Thin film thickness in the order of 100nm, can be used to make ultra thin and bendable displays. In comparison to inorganic semiconductors, OSCs have lower brightness level and shorter life span. In an OLED, the first step to creating light is the injection of charge carriers from the electrodes. Holes and electrons are typically injected into the hole-transport layer (HTL) and the electron transport layer (ETL), respectively. Afterwards, these charge carriers migrate toward the center of the device under the influence of the applied field. The rates of charge migration are field-dependent and depend on the mobilities of both holes in the HTL and electrons in the ETL. In the center of the device, at the HTL/ETL interface, these injected charges meet each other and recombine to form an excitonic (excited) state, from which emission occurs to create light in an OLED display. Exciton migration and following decay of an exciton produce the light (Fig. 1.1).

OPVs are another example where charge and energy transport properties are relevant for the performances of the device. OLEDs emit light in response to an electric current, while solar cell does the opposite: it converts the energy of sunlight directly into electric current. This process can be described by the following steps: (1) absorption of an incoming photon leading to the formation of a exciton, a bound electron-hole pair; (2) exciton diffusion; (3) exciton dissociation (charge separation); and (4) migration of separated electrons and holes within the organic semiconductor to the respective electrodes. The longer it takes for an electron-hole pair to reach the electrodes, the higher the chances of premature deexcitation as well as charge recombination. Organic solar cells are cheap and environmentally friendly alternatives to inorganic solar cells, which have lower power conversion ratio. The organic solar cells are not only scalable in chemical synthesis but also the materials required for the synthesis are available cheaply. These solar cells are 1000 times thinner than traditional silicone solar cells which also makes transportation much easier. Flexibility of organic

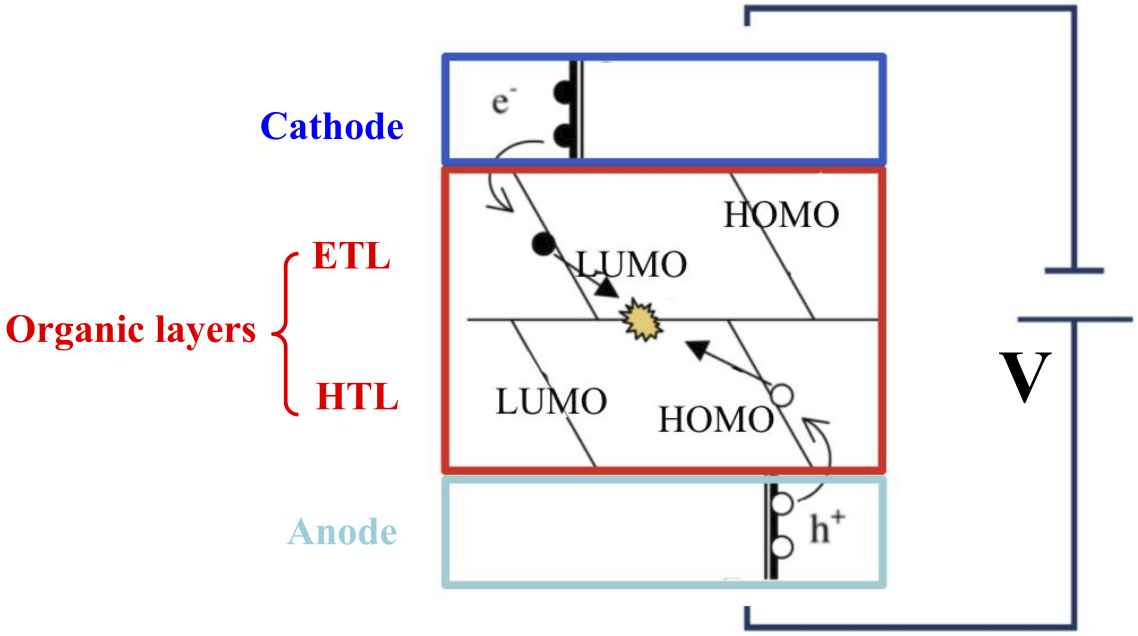

Figure 1.1: The working principle of a typical OLED: 1. injection of electrons and holes, 2. transport of the two types of carriers, 3. formation of the exciton between the two organic layers, 4. the emission of light.

solar cells allows them to be used in variety of opto-electronics devices applications such as clothing, baggage and many more.

Despite having many advantages, there are several underlying problems and open questions regarding selection of materials and tuning their properties. The major drawback of an organic solar cell is that it has low efficiency (5%), which is lower than inorganic solar cells (15%). Also, organic solar cells have less lifetime in comparison to the inorganic solar cells. Due to long exposure to the ambient light, they degrade faster than inorganic solar cells. Other major problems include low stability, low-strength and color balance. To design and build better OLEDs, it is important to understand the charge transport mechanism, which can be a complex phenomenon. This is the primary focus of my research. Distribution of electrons and holes are important factors for the efficiency of the electron and hole combination.

Theoretical tools can play a vital role in quantitative and material prediction of the transport properties, which can further support the development of improved complex materials. A complete model of any system involves electron-hole injection/ejection, electron- hole combination and dissociation, charge propagation, exciton transport and decay, as well as other interacting molecules in the simulations.

Although, the fundamentals of charge and energy transport are known but the predictive and detailed quantitative model is still lacking at microscopic and mesoscopic level. One of the main problems with simulation of these systems is the size of the realistic representation of the system.

2 Computational Toolbox

In the past few decades, there has a vast development in the experimental techniques as well as mathematical description of the matter at the atomistic level. One of the main aspects of the mathematical description is to determine the degree of precision to which it reproduces the observed experimental behaviour. Computational simulations have become the most important tool to imitate the gap between experimental observations and atomistic resolutions.

Considering the molecule as ball and connected with springs and modelled with an approach molecular mechanics (MM). Molecular dynamics (MD) is a numerical approach which can be used to calculate trajectory of many systems such amorphous organic solids. These trajectories can be used to extract relevant information or properties at the atomistic scale, which is beyond feasibility of experiments. By solving the Newton's equation iteratively, the trajectories can be generated.

Using MM formalism, it is difficult to describe the bond breaking and bond formations, molecualar or atomic spectra obtained due to interaction of matter with light, effect observed due to electronic delocalisation and other effects which require the concept of electronic states. In order to study these phenomena, quantum mechanics was specifically developed to describe the interactions between nuclei, electrons and other subatomic particles.

QM formalism takes into account the wave and particle duality nature of the matter. QM description can potentially describe the behaviour of atoms and molecules. However, computational costs associated with QM studies are very high.

The combination of quantum mechanics/molecular mechanism (QM/MM) can bring the cost down whereas at the same time it can provide relevant information of the system under observation.

Several methods have been developed to perform simulations on many solids including the amorphous solids such as Hartree-Fock(HF), density functional theory(DFT) and others.

This chapter briefly recapitulates the basics of quantum chemical methods for the excited states as well as basic understandings of Born-Oppenheimer approximation and Molecular Dynamics. Density functional theory applies the stationary electronic Schrödinger equation to solve for a system of interacting electrons and nuclei using several approximations. Interacting electrons are replaced by non-interacting quasi particle which implies that field approximations and other assumptions can lead to systematic error, where can be further corrected.

2.1 Born-Oppenheimer approximation

The Born-Oppenheimer approximation assumes that electronic and nuclear motion in a molecule can be separated. Thus, the molecular wave function can separated in terms of electronic position and nuclear positions which involves the following assumptions:

1. The electronic wave function solely depends upon the nuclear position of the atom but not their velocities as nuclear motion is much lower than electronic motion, thus it can be considered to be fixed.

2. Nuclear motion such as rotation and vibration is tainted by the speedy electron motion.

The basis for the Born-Oppenheimer approximation is due to the fact that mass of the nuclei is much larger than the mass of the electron. Thus, nuclei moves much slower than electron. The Hamiltonian of a system of n electrons described by coordinates $\mathbf{r}_1, \mathbf{r}_2, \mathbf{r}_3, ..., \mathbf{r}_N = \mathbf{r}$ and N nuclei described by coordinates $\mathbf{R}_1, \mathbf{R}_2, \mathbf{R}_3, ..., \mathbf{R}_N = \mathbf{R}$ and momenta is described by $\mathbf{P}_1, \mathbf{P}_2, \mathbf{P}_3, ..., \mathbf{P}_N = \mathbf{P}$ is given by:

$$\hat{H}(\mathbf{r}, \mathbf{R}) = \hat{T}_e(\mathbf{r}) + \hat{T}_N(\mathbf{R}) + \hat{V}_{NN}(\mathbf{R}) + \hat{V}_{eN}(\mathbf{r}, \mathbf{R}) + \hat{V}_{ee}(\mathbf{r}) \tag{2.1}$$

where $\hat{T}_N$ denotes kinetic energy of the nuclei, $\hat{T}_e$ kinetic energy of the electrons and $\hat{V}_{NN}$, $\hat{V}_{eN}$ and $\hat{V}_{ee}$ denotes the interactions of nucleus-nucleus, nuclei-electron, and electron-electron respectively. These terms are further expanded as:

$$\hat{T}_e = \sum_{i=1}^{N_e} \frac{\mathbf{P}_i^2}{2M_i} \tag{2.2}$$

$$\hat{T}_N = \sum_{I=1}^{N} \frac{\mathbf{P}_I^2}{2M_I} \tag{2.3}$$

$$\hat{V}_{NN} = \sum_{I>J} \frac{Z_I Z_J e^2}{\mathbf{r}_{IJ}} \tag{2.4}$$

$$\hat{V}_{eN} = -\sum_{I>J} \frac{Z_I e^2}{\mathbf{r}_{Ii}} \tag{2.5}$$

$$\hat{V}_{ee} = -\sum_{I>J} \frac{e^2}{\mathbf{r}_{ij}} \tag{2.6}$$

Overall equation of the atomic Hamiltonian can be written as

$$\hat{H} = \hat{T}_e(\mathbf{r}) + \hat{V}_{NN}(\mathbf{R}) + \hat{V}_{eN}(\mathbf{r}, \mathbf{R}) + \hat{V}_{ee}(\mathbf{r}) \tag{2.7}$$

This equation is very complicated but intractable. Therefore, we require several approximations to solve the Eq. 2.7 for heavier element.

The kinetic energy of the electron nuclei is proportional to the ratio of the mass of the electron $(M_e) = 1$ to the mass of the nucleus $(M_p) = 1836.15$, which is approximately 0.00054. This leads to strong separation of time scale between the electronic and nuclear motion. Thus, the two wave form can be separated using quasi-separable ansatz of the form

$$\psi(r, R) = \phi_e(\mathbf{r}, \mathbf{R})\phi_N(\mathbf{R}) \tag{2.8}$$

where $\phi_N(\mathbf{R})$ represents the nuclear wave function and $\phi_e(\mathbf{x}, \mathbf{R})$ represents an electronic wave function which depends on the nuclear coordinates. But Eq. 2.5 can prevents us from applying this concept for the separation of the variable. In a dynamical sense, electrons are much lighter than the mass of the proton, thus nuclear motion governs the motion of the electron. The electrons are dragged along the with nuclei with requiring a finite relaxation time. After this consideration, 2 terms from the Eq. 2.7 can be neglected.

$$\hat{H} = -\sum_{i=1}^{n} \frac{1}{2}\nabla_i^2 + \sum_{i<j} \frac{1}{|\vec{r}_i - \vec{r}_j|} - \sum_{i,I}^{n,N} \frac{Z_I}{|\vec{r}_i - \vec{R}_I|} + \sum_{I<J} \frac{Z_I Z_J}{|\vec{R}_i - \vec{R}_j|} \tag{2.9}$$

such that

$$\hat{H}_{el}\psi(\mathbf{r};\mathbf{R}) = E_{el}\psi(\mathbf{r};\mathbf{R}) \tag{2.10}$$

This Eq. 2.9 is called "clamped-nuclei" Schrödinger equation. Also, $\hat{V}_{NN}$ term is also neglected form this equation, which is justified since $\mathbf{R}$ is just a parameter and therefore it yields a constant and only shifts the eigenvalues only by some constant amount. Thus, Leaving out $\hat{V}_{NN}$ from the Eq. 2.1 gives:

$$\hat{H}(\mathbf{r}, \mathbf{R}) = \hat{T}_e(\mathbf{r}) + \hat{V}_{eN}(\mathbf{r}, \mathbf{R}) + \hat{V}_{ee}(\mathbf{r}) \tag{2.11}$$

such that

$$\hat{H}_e\psi(\mathbf{r};\mathbf{R}) = E_e\psi(\mathbf{r};\mathbf{R}) \tag{2.12}$$

As of now, we will assume that $\hat{V}_{NN}(\mathbf{R})$ is included in the electronic Hamiltonian.

In the next section, the solution of the electronic Schrödinger equation using density functional theory along with development in DFT is presented.

2.2 Quantum mechanical Method

2.2.1 Density Functional Theory (DFT)

DFT is one of the advanced method and the most popular method which is available in computational physics, computational chemistry and condensed-matter physics. DFT was considered as an inefficient method for the quantum calculation of the molecules until late 1990s. DFT has one major advantage in comparison to the traditional methods such as Hartree–Fock theory and that is because of its very low computational cost. Despite

recent development in the DFT, there are still challenges in describing the intermolecular interactions, charge transfer excitation, transition state, etc.

Traditional methods attempt to approximate the solution of Schrödinger equation of N interacting electrons moving in external potential. This traditional approach has some issues:

1. Even for the smallest system having N number of electrons, the resultant wave length is very complicated. So the problem is highly nontrivial.

2. The computational support and cost even for a smaller system is very high, so the description of larger systems seems impossible.

So, in order to find a possible solution to the aforementioned problems, a different approach has been suggested by the DFT. According to DFT approach, instead of considering many-body wave-function, one-body density is used as a functional variable. The density function $n(\mathbf{r})$ is a function of three spatial coordinate rather than 3N coordinate wave-function as in traditional approach. Using density functional theory approach, description of larger systems are possible to investigate. The foundation of density functional theory was led by Hohenberg-Kohn and Kohn-Sham theorem, which will be explained in details in the following sections. Furthermore, the various levels of approximation to the exchange-correlation energy functional are discussed. In the next section, the extension of original Hohenberg-Kohn and Kohn-Sham therorem, are presented to cover a wide range of physical situations.

Hohenberg-Kohn and Kohn-Sham theorem

For a system of N interacting electrons, ground state DFT is described by given Hamiltonian:

$$\begin{aligned}\hat{H} &= \hat{T} + \hat{V} + \hat{V}_{ee} \\ &= -\sum_{i=1}^{N} \frac{\nabla_i^2}{2} + \sum_{i=1}^{N} v(\mathbf{r}_i) + \frac{1}{2}\sum_{i=1}^{N}\sum_{\substack{j=1 \\ i\neq j}}^{N} \frac{1}{|\mathbf{r}_i - \mathbf{r}_j|}\end{aligned} \tag{2.13}$$

where $\hat{T}$, $\hat{V}$ and $\hat{V}_{ee}$ represents the kinetic energy, potential energy and electron-electron interaction energy, respectively.

The central idea of density functional theory for non-degenerate ground states is given by Hohenberg-Kohn theorem [9], which is given by the following assumptions.

1. The ground state electron density of a system of interacting electrons $\rho(\mathbf{r})$ uniquely determines the external potential v(**r**) of the system and thus all physical properties of the system and the Hamiltonian can be determined.

2. Using theory of variational principle, the ground-state energy E_0 having ground-state density $\rho_0(\mathbf{r})$ and ground-state potential $v_0(\mathbf{r})$ can be obtained. It only involves the density of the system which further implies that ground state energy of the system can be described as the function of density $E_{v_0}[n]$. The ground state energy

is E_0 if and only if the true value of the ground-state density is put. For all the other densities $n(\mathbf{r})$

$$E_{v_0}[\rho_0] < E_{v_0}[\rho] \tag{2.14}$$

According to Rayleigh-Ritz variational principle, ground state wave function minimizes the energy expectation value.

3. Functional energy of the system can be written as

$$E_{v_0}[\rho] = F[n] + \int d^3 r v_0(\mathbf{r})\rho(\mathbf{r}) \tag{2.15}$$

where functional $F(\rho)$ is a universal functional depicting the particle-particle interaction, which is independent of particular system under investigation. This implies that the same functional can be used irrespective of how big or small the system can be.

From Hohenberg-Kohn variational principle which is explained in the second assumption can be obtained as the solution of the euler equation, which is given as

$$\frac{\delta E_v[\rho]}{\delta\rho(\mathbf{r})} = \frac{\delta F[\rho]}{\delta\rho(\mathbf{r})} + v(\mathbf{r}) = 0 \tag{2.16}$$

This equation can be treated as an alternative to the time-independent Schrödinger equation. Hohenberg-Kohn therorem is exact, but no explicit form of $E[\rho]$ is known. Therefore, it can lead to the complexity in solving the exact wave functions and ultimately nothing would be gained as of now. Density function theory employs several approximations leading to very efficient and reasonable results for big or small systems.

The Hohenberg-Kohn functional $F[\rho]$ is given by:

$$\begin{aligned} F[\rho] &= \hat{T}[\rho] + \hat{V}_{ee}[\rho] \\ &= \langle\psi[\rho]|\,\hat{T}\,|\psi[\rho]\rangle + \langle\psi[\rho]|\,\hat{V}_{ee}\,|\psi[\rho]\rangle \end{aligned} \tag{2.17}$$

where $\psi[\rho]$ denotes the wave function of n-interacting electrons, which yields the density ρ which minimises the expectation value of $\hat{T}+\hat{V}_{ee}$ of the system under observation. The explicit density dependence of the Hohenberg-Kohn functional $F[\rho]$ is still unknown. For this purpose, Thomas-Fermi approximation has been suggested. Nevertheless, the accuracy of these kind of approximation is limited to practical uses. Thus, the Eq. 2.16 is hardly used in electronic structure calculation.

Hohenberg-Kohn theorem provides the basis for the constructions of the single particle scheme which effectively allows the calculation of density as well as energy of the interacting electrons. This improvement to the Hohenberg-Kohn theorem is well known as the Kohn-Sham equation, which is now considered as the heart of modern density functional theory. Kohn-Sham equation is given by:

$$\left[-\frac{\nabla^2}{2} + v_{ks}(\mathbf{r})\right]\phi_i(\mathbf{r}) = \epsilon_i\phi_i(\mathbf{r}) \tag{2.18}$$

Density of the N-interacting particles occupied in orbital can be computed by using Slater determinant:

$$\rho(\mathbf{r}) = \sum_{i}^{occupied} |\phi(\mathbf{r})|^2 \tag{2.19}$$

The principal idea of the Kohn-Sham scheme is to build the single-particle potential $v_{ks}(\mathbf{r})$, such that the density of the interacting system of interest is equal to the density of the auxiliary non-interacting system. Thus, the Hohenberg-Kohn functional can be described as:

$$F[\rho] = T_{ks}[\rho] + U[\rho] + E_{exc}[\rho] \tag{2.20}$$

where $U[\rho]$ represents the classical electrostatic energy of the charge distribution $\rho(\mathbf{r})$ which is further expressed as:

$$U[\rho] = \frac{1}{2} \int d^3r \int d^3r' \frac{\rho(\mathbf{r})\rho(\mathbf{r'})}{|r - r'|} \tag{2.21}$$

and $E_{exc}[\rho]$ is called exchange energy-correlation energy and defined as follows:

$$E_{exc}[\rho] = T[\rho] + V_{ee}[\rho] - U[\rho] - T_{ks}[\rho] \tag{2.22}$$

Using the above equation, we can derive the effective potential of the system by putting back to the Eq. 2.18

$$v_{ks}[\rho](\mathbf{r}) = v(\mathbf{r}) + \int d^3r' \frac{\rho r'}{|r - r'|} + v_{exc}[\rho](\mathbf{r}) \tag{2.23}$$

where v_{exc} is the exchange-correlation potential, which is described as:

$$v_{exc}[\rho](\mathbf{r}) = \frac{\delta E_{exc}\rho(\mathbf{r})}{\delta\rho(\mathbf{r})} \tag{2.24}$$

Eq. 2.21 $v_{ks}[\rho](\mathbf{r})$ depends on the density of the system, thus all the equations have to be solved self-consistently. The Eq. 2.23 is called Kohn-Sham equation. Using this equation, the orbitals can be found and further energy can be calculated through reinsertion of into the functional. For the orthonormal condition, orbital eigenvalues are entered as Lagrangian multipliers [10, 11]. Moreover, the principal definition of exchange-correlation energy is not useful for the practical implications. Thus, we use an approximation for this quantity, which is further discussed in the following section.

2.3 Density function approximation

Though, DFT provides accurate results for big or small system under observation, however it is yet not clear how to construct the exchange-correlation functional. The most challenging task concerning E_{exc} is that, it is a universal function of density, meaning that it has to be the same for all the systems. The first practical attempt to provide approximation to

exchange-correlation functional predate the foundations of DFT by Hohenberg and Kohn. Thomas and Fermi propose a model where kinetic energy of the electrons are expressed in terms of density [12, 13]. Moreover, the model predicts that there is no stable molecules, thus it is unfit for the quantum mechanical calculations. Continuous development has been made in quantitative performance of DFT, which is computationally efficient and cost effective.

Exchange correlation function has two major consequences, first, it promises to construct an approximate functional according to the system of interest and second, it is challenging as a good approximation should perform the calculation of different systems as well as different physical situations.

Local density approximation

Both aforementioned promises and challenges can be reflected in the local density approximation (LDA) which goes back to the Kohn-Sham theorem [14]. This kind of approximation has become popular for solid-state systems, though it is very inaccurate for molecules. In LDA approach the exchange-correlation energy is given by

$$E_{exc}^{LDA}[\rho] = \int d^3r \rho(\mathbf{r}) e_{exc}^{ud}(\rho(\mathbf{r})) \tag{2.25}$$

where $e_{exc}^{ud}(\rho(\mathbf{r}))$ represents the exchange-correlation energy of an electron in a homogeneous electron gas of the same density $\rho(\mathbf{r})$. LDA can also be generalised to the polarised systems, which then known as local spin density approximation (LSDA). The most accurate data can be obtained from the Quantum Monte Carlo calculations [15].

LDA approximation is expected to be a good approximation especially for molecules with low varying densities. Although, this condition is hardly ever met for real electronic systems. Nevertheless, LDA has proved to be exceptionally accurate for a wide variety of systems where the densities are varying slowly. In a system where LDA works well, it often consists of sp bonds, geometries are good, bond lengths and angles are accurate within a few percent.

The principal advantages of this approximation in DFT over the other method such as Hartree-Fock is that it performs well and many experimentally observed physical properties can be determined to a great level of accuracy. In weakly bonded systems these inaccuracy are exaggerated and bond lengths are too short. The question is whether LDA is applicable or not. For example, LDA works well with the group IV semiconductors, but the performance using this approximation was unclear.

Generalise gradient approximation

LDA is exceptionally accurate for small molecule where density does not vary much due to adoption of uniform electron gas. For this reason, improved functional has to be developed to take into account the density fluctuation through the inclusion of density gradient $\nabla\rho(\mathbf{r})$. This approximation is called generalized gradient approximations (GGAs). Exchange-correlation energy using GGA approximation is given by:

$$E_{exc}^{GGA}[\rho] = \int d^3r f(\rho(\mathbf{r}), \nabla\rho(\mathbf{r})) \tag{2.26}$$

In LDA, E_{exc}^{ud} was unique, however in GGA, it is not unique, thus many different approaches are possible depending on the system of interest. While constructing the GGA, one should keep in mind the properties one tries to incorporate using the exact functional into the restricted functional approximation. GGA has gained a lot of popularity and been quite accurate in quantum calculation, especially in chemistry, and it is also less computationally expensive.

One of the most popular GGA approximations is the Perdew-Burke-Ernzerhof (PBE) functional [16]. It is derived by using a certain condition which holds true for the exact functional that can be reproduce by using approximative form. Thus, it is free from fitted parameters, which holds true for broad range of systems. GGA functional also employs fits to the reference data, which limits their applicability.

In recent years, GGA has been further developed into a new class of "meta-GGA" functional. In addition to the LDA and GGA functional depends of the kinetic energy of the Kohn-Sham orbitals, which is given by:

$$\tau(\mathbf{r}) = \frac{1}{2} \sum_{i}^{occupied} |\nabla \phi_i(\mathbf{r})| \tag{2.27}$$

The "meta-GGA" functional is given by:

$$E_{exc}^{mGGA}[\rho] = \int d^3 r f(\rho(\mathbf{r}), \nabla\rho(\mathbf{r}), \tau(\mathbf{r})) \tag{2.28}$$

The additional flexibility in the mGGA functional gained by introducing a new variable, which is used to incorporate more exact properties into the approximation. Unlike LDA and GGA, mGGA also depends explicitly on the Kohn-Sham orbitals.

Hybrid functional

Despite the improvement in LDA and GGA, both the functionals suffer from error due to self-interaction. Both failed to remove the interaction of interaction with themselves or with other electrons which has the same spin following the pauli exclusion principle, from the energy contribution. This can lead to underestimation of the band gap and the artificial delocalisation of the electron. LDA and GGA functionals are local as the energy is integral over the function of the density at a specific point of the system and also independent of all other spatial locations. Some non-locality is introduced using gradient information, but it can not be accounted for the interaction over the larger distances. On the contrary, exchange term in Hartree-Fock theory (HF) method cancels the self-interaction specifically, but it is non-local i.e., it is calculated as an integral over two spatial coordinate. The hybrid functional is a mix fraction of the exact exchange and the GGA exchange, which is given by:

$$E_{exc}^{HYB}[\rho] = \alpha E_{exc}^{HF}[\rho] + (1-\alpha) E_{exc}^{GGA}[\rho] \tag{2.29}$$

where α is a parameter which controls the HF exchange. Different values of α is used for different functionals, which can further improve the performance for the system under observation.

The original theory given by Hohenberg, Kohn and Sham can only be applied to the non-degenerate quantum system. Hohenberg-Kohn formalism establishes the connection

between the density of ground state and the Hamiltonian, thus the variational principle only yields an equation for the ground state. The central idea of full time-dependent extension of DFT (TD-DFT) was given by Runge-Gross theorem, which is briefly explained further in this section.

2.3.1 Time-dependent density functional theory (TD-DFT)

Time-dependent Schrödinger equation is given by:

$$i\frac{\partial}{\partial t}\psi(\underline{\mathbf{r}}, t) = \hat{H}(t)\psi(\underline{\mathbf{r}}, t) \tag{2.30}$$

where ψ is the many-body wave-function of N interacting electrons with coordinates $\underline{\mathrm{r}} = (\mathbf{r}_1, \mathbf{r}_2, .., \mathbf{r}_N)$ and $\hat{H}(t)$ time dependent external potential . This equation describes the time evolution of a system which satisfies the given initial condition:

$$\psi(\underline{\mathbf{r}}, t = t_0) = \psi(\underline{\mathbf{r}}) \tag{2.31}$$

The Runge-Gross theorem states that, there is one-to-one correspondence between the time-dependent density $\rho(\mathbf{r}, t)$ and the external time-dependent potential, $v(\mathbf{r}, t)$, which ultimately lead to the time evolution of $\rho(\mathbf{r}, t)$. All the observable of the system can be written as a function of density. The practical framework of the Runge-Gross theorem was give by Kohn-Sham scheme.

Let's define a system of non-interacting electrons, obeying Schrödinger equation:

$$i\frac{\partial}{\partial t}\phi(\underline{\mathbf{r}}, t) = \left[-\frac{\nabla^2}{2} + v_{ks}(\mathbf{r}, t) \right] \phi_i(\mathbf{r}, t) \tag{2.32}$$

Similarly, Kohn-Sham potential is given by

$$v_{ks}[\rho](\mathbf{r},t) = v(\mathbf{r},t) + \int d^3r' \frac{\rho r', t}{|r - r'|} + v_{exc}[\rho](\mathbf{r},t) \tag{2.33}$$

where $v(\mathbf{r},t)$ denotes the Coulombic potential of the nuclei as well as the time-dependent contribution of an external electromagnetic field. Further, the time-dependent exchange-correlation potential is given function is chosen in such a way that the density of the Kohn-Sham orbital electrons is equal to density of the electrons in the interacting system.

$$\rho(\mathbf{r},t) = \sum_{i}^{occupied} |\phi(\mathbf{r},t)|^2 \tag{2.34}$$

Exchange-correlation potential v_{exc} is a complex quantity, which has to approximated. The most common approximation is known as adiabatic local density approximation (ALDA). In ALDA approximation, it is assumed that exchange-correlation potential at time t is equal to the ground-state LDA potential, which is given by:

$$E_{exc}^{ALDA}[\rho](\mathbf{r},t) = E_{exc}^{ud}[\rho](\mathbf{r},t) \tag{2.35}$$

In the similar fashion, we can derive the adiabatic GGA or meta-GGA. In the adiabatic approximation, the time-dependent density is simply introduced into the time-independent exchange-correlation function. This approximation performs quite well, but there are also some failures which have been reported in the literature.

Time-dependent DFT proves to be effective for the simulation of time-independent quantum mechanical process in solids and in molecules. It provides a theoretical background of the charge transfer and calculation of the properties of the excited states.

2.3.2 Density Functional Tight binding (DFTB)

Despite, DFT is accurate in quantum calculations and computationally efficient in comparison to most of the electronic structure based methods, there has been a major concern regarding simulation of large system with thousands of atoms. Another major concern is regrading expanding applicability of this method from a single molecular dynamics to simulation of chemical reaction at an active site of a protein in aqueous solution. Further, the time scale of these kind of simulation requires millions of QM calculations and can be nanosecond scale. These QM calculations are well beyond the scope of the DFT calculation.

In order to overcome this limitation, semi-empirical methods with some approximation can be applied at the cost of some accuracy but with a low computational cost. These methods rely on fitting parameters to reference data, which limits the transferability. The Density Functional based Tight binding method is derived from the second-order expansion of Kohn-Sham total energy. DFTB [17, 18] is originally based on the minimal basis set, which means that only valence electrons are considered explicitly, whereas the core electrons are treated by two-center potential. DFTB performs well with organic molecules as the underlying assumptions are fulfilled. Starting form the energy expression of Kohn-Sham system of non-interacting electrons:

$$E[\rho] = \sum_i f i \langle \phi_i | \left(-\frac{1}{2}\nabla^2 + V_{ext} + \frac{1}{2}\int d^3r' \frac{\rho(\mathbf{r})\rho(\mathbf{r'})}{|r - r'|} \right) |\phi_i\rangle + E_{exc}[\rho] + E_{nu} \tag{2.36}$$

This is another way of writing Kohn-Sham orbitals $|\phi_i\rangle$ and f_i represents the orbital occupation and the last term can be expanded as:

$$E_{nu} = \sum_{A,B} \frac{Z_A Z_B}{|R_A - R_B|} \tag{2.37}$$

It can be further expanded as follows:

$$\begin{aligned} E[\rho] = & \sum_i f i \langle \phi_i | -\frac{1}{2}\nabla^2 + \int d^3r' \frac{\rho_0(\mathbf{r'})}{|r - r'|} + \frac{\delta E_{exc}[\rho_0]}{\delta\rho(\mathbf{r})} + V_{ext}(\mathbf{r}) |\phi_i\rangle \\ & + \frac{1}{2}\int d^3r \int d^3r' \left(\frac{1}{|r - r'|} + \frac{\delta^2 E_{exc}[\rho_0]}{\delta\rho(\mathbf{r})\delta\rho(\mathbf{r'})} \right) \\ & + E_{exc}[\rho] + E_{nu} - \frac{1}{2}\int d^3r d^3r' \frac{\delta\rho(\mathbf{r})\delta\rho(\mathbf{r'})}{|r - r'|} - \int d^3r \frac{\delta E_{exc}[\rho]}{\delta\rho(\mathbf{r})}\rho_0(\mathbf{r}) \\ & = E^0[\rho 0] + E^1[\rho 0, \delta\rho] + E^2[\rho 0, (\delta\rho)^2] + E^3[\rho 0, (\delta\rho)^3] + \ldots \end{aligned} \tag{2.38}$$

where, $\delta\rho$ is fluctuation in density and ρ_0 is atomic reference density. Overall density can be given as $\rho = \rho_0 + \delta\rho$. The first line of the equation represents the band structure energy(BSE), which is given by:

$$E_{BSE}[\delta\rho] = \sum_a f_i \langle \phi_a | H[\rho_0] | \phi_b \rangle \tag{2.39}$$

where the Hamiltonian $H^0 = H[\rho_0]$ and it does not contain any charge. It only depends on the reference density. The second line in the equation represents the Coulomb interaction and not exchange contribution, which is given by:

$$E_{colmb}\delta\rho = \frac{1}{2}\int d^3r \int d^3r' \left(\frac{1}{|r - r'|} + \frac{\delta^2 E_{exc}[\rho_0]}{\delta\rho(\mathbf{r})\delta\rho(\mathbf{r'})} \right) + O(\delta\rho^3) \tag{2.40}$$

And finally the third line represents the collective repulsive energy, which is given by:

$$E_{rep} = E_{exc}[\rho] + E_{nu} - \frac{1}{2}\int d^3r d^3r' \frac{\delta\rho(\mathbf{r})\delta\rho(\mathbf{r'})}{|r - r'|} - \int d^3r \frac{\delta E_{exc}[\rho]}{\delta\rho(\mathbf{r})}\rho_0(\mathbf{r}) \tag{2.41}$$

Finally the overall equation can be given as:

$$E[\rho] = E_{BSE}[\delta\rho] + E_{colmb}\delta\rho + E_{rep} \tag{2.42}$$

The three energy contributions in the Eq. 2.42 will be further approximated.

As mentioned before, in the DFTB method we only consider the valence electrons and the core electrons effects only contribute to the repulsive energy. The different methods

of DFTB correspond to different levels of truncation of the Taylor series. The truncation after the first-order term produces the original form of DFTB. Further, the inclusion of second-order term in the Eq. 2.38 leads to the DFTB2 [18] method. Consequently, the inclusion of third term produces the DFTB3.

In DFTB, matrix elements are listed in tables in such a manner that they do not have to be integrated explicitly for each geometry. LACO approach is used for KS orbital which separates the density into the atomic contribution and is given by:

$$\rho_0(\mathbf{r}) = \sum_i |\phi(\mathbf{r})|^2 = \sum_a \rho_a(\mathbf{r}) \tag{2.43}$$

Usually, the three center contributions are neglected as in the DFTB method these expanded terms are approximated as a pairwise potential, which are set to produce the DFT energies. In Eq. 2.38, the first term represents the Hamiltonian matrix-element, which are approximated using minimal basis set of slater type for the KS orbital, which is given by:

$$\begin{aligned} E^0[\rho 0] &= \sum_i^{occupied} \langle \phi_i | \hat{H}_0 | \phi_i \rangle \\ &= \sum_i^{occupied} \sum_\mu \sum_\nu c_i^\mu c_i^\nu H_{\mu\nu}^0 \end{aligned} \tag{2.44}$$

All the four terms in Eq. 2.41 depend only on the reference density ρ_0 and are categorised as the repulsion energy, which is given by:

$$E_{rep} = \frac{1}{2} \sum_a \sum_b V_{ab}^{rep}[\rho_a^0, \rho_b^0, r_{ab}](a) \tag{2.45}$$

In this case, fluctuation in the density is not taken into account, which is generally referred as original DFTB. Additional approximation are required to speed up the calculations. In order to do this, density fluctuation $\delta\rho$ is used to express as a sum of the atomic density fluctuations, which is given by:

$$\delta\rho = \sum_a \delta\rho_\alpha \tag{2.46}$$

where α represents the alpha atom and the equation describes the fluctuation in charge, which is given by $\delta_{q_\alpha} = q_\alpha - q_\alpha^0$, where q_α is the Mulliken charge and q_α^0 is the valence electron of the neutral atom α. Using these approximation, the second order term can be written as:

$$E^{2nd} = \frac{1}{2} \sum_{\alpha\beta} \gamma_{\alpha\beta}\gamma_{q\alpha}\gamma_{q\beta} \tag{2.47}$$

$$\gamma_{\alpha\beta} = \frac{1}{R_{\alpha\beta}} - S(R_{\alpha\beta}, U_\alpha, U_\beta) \cdot h \tag{2.48}$$

$\gamma_{\alpha\beta}$ in the Eq. 2.48 represents the integral over the product of two normalised Slater-type charge densities. The interaction between two atoms having fluctuating charge densities is mediated via $\gamma_{\alpha\beta}$, where $\gamma_{\alpha\alpha}$ represents the electron-electron interaction confined to a single atom, which is further described by Hubbard parameter U_α. For the system having larger interatomic distances, the exchange-correlation terms vanishes and $\gamma_{\alpha\beta}$ reduced to the coulombic interaction between the two partial charges.

The function S denotes a complicated expression, which is responsible for the correct convergence of $\gamma_{\alpha\beta}$ at $R_{\alpha\beta} = 0$. DFTB2 approach is widely used in QM calculation in inorganic, organic, molecules and solids. However, DFTB2 has a direct relation between the chemical hardness and atomic size. Furthermore, the Hubbard parameter does not depend on the charge fluctuation of the atom, which leads to substandard description of systems where charge atoms are involved.

In order to tackle this problem, approximation are employed. This is led to the development of DFTB3 approach, which take into account the third energy term, where charge atoms are involved. This improves the descriptions of the charged molecules and the E^{3rd} are given by:

$$E^{3rd} = \frac{1}{3}\sum_{\alpha\beta}\Gamma_{\alpha\beta}\delta q_\alpha^2\delta_{q\beta} \tag{2.49}$$

The matrix Γ contains the derivative of γ function with respect to the charge and is given by the following equation:

$$\Gamma_{ab} = \left.\frac{\partial\gamma_{\alpha\beta}}{\partial q_\alpha}\right|_{q_\alpha^0} = \left.\frac{\partial\gamma_{\alpha\beta}\partial U_\alpha}{\partial U_\alpha\partial q_\alpha}\right|_{q_\alpha^0} \tag{2.50}$$

$$\Gamma_{ab} = \left.\frac{\partial\gamma_{\alpha\alpha}}{\partial q_\alpha}\right|_{q_\alpha^0} = \left.\frac{\partial\gamma_{\alpha\alpha}\partial U_\alpha}{\partial U_\alpha\partial q_\alpha}\right|_{q_\alpha^0} \tag{2.51}$$

The Hubbard parameter is given by $U_\alpha^d = \partial U_\alpha/\partial_{qa}\big|_{q_\alpha^0}$ is calculated analytically, which is the third derivative of the total energy w.r.t. charge. With this approximation, the Kohn-Sham equation can be formulated in a matrix form which is given by:

$$H_{\mu\nu} = H^0_{\mu\nu} + S_{\mu\nu}\sum_c \delta_{q_c}\Big(\frac{1}{2}(\gamma_{\alpha c} + \gamma_{\beta c}) + \frac{1}{3}(\delta q_\alpha\Gamma_{\alpha c} + \delta q_\beta\Gamma_{\beta c}) + \frac{1}{6}\delta_{q_c}(\Gamma_{c\alpha} + \Gamma_{c\beta})\Big) \tag{2.52}$$

Using this description, biological or organic systems with charge have been improved.

2.3.3 Time-dependent density functional bight binding (TD-DFTB)

Self-consistent DFTB provides the calculation of ground-state, however we are also interested in the excited state calculation. Within the limit of DFT, excited state calculation can be done using TD-DFT formulation. Using the same approach, DFTB method is further extended in a time-dependent (TD-DFTB) approach, which is analogous to the linear

response theory of the Kohn-Sham DFT approach to compute the excitation energy of the system. TD-DFTB methods refer to the Casida's equation, which is given by:

$$\sum_{mn}\left[((\epsilon_s-\epsilon_i)^2\delta_{im}\delta_{sn}+4\sqrt{\epsilon_s-\epsilon_i}K_{is,mn}\sqrt{\epsilon_m-\epsilon_n})F_{mt}\right]=\Omega^2F_{is} \tag{2.53}$$

The above equation is Hermitian eigenvalue problem on the space of orbital excitation. where, indices i,m,.. are occupied orbital, whereas s,n,.. refer to the unoccupied virtual orbital, Ω represents the eigenvalues excitation energies, $K_{is,mn}$ describes the Coulombic interaction between orbital excitations, which can be approximated in DFTB.

$$K_{is,mn}=\sum_{A,B}q_A^{is}q_B^{mn}\gamma_{AB} \tag{2.54}$$

where q_A^{is} is Mulliken transition charges which is given by:

$$q_A^{is}=\frac{1}{2}\sum_{\nu\in A,\mu}(c_{\nu i}c_{\mu s}+c_{\mu i}c_{\nu s})S_{\mu\nu} \tag{2.55}$$

Finding the solution for eigenvalues is very expensive as it requires $O((N_{occ.}\cdot N_{virt.})^3)$ operations. Davidson algorithm can be used if low lying eigenvalues are required, which allows the problem to be restricted to a small space. Thus, application to the excitation transport is particularly easy using TD-DFTB approximation.

2.3.4 Long-range corrected DFTB (LC-DFTB)

The long range corrected functional improves the original DFT functional by removing asymptotically self-interaction error via the long range contribution. Taking this idea into consideration, DFTB approach can be further extended to long-range separated functionals which is led to development of the LC-DFTB.

Baer, Neuhauser and Livshits functionals are used to extend the DFTB, which splits the Coulomb interaction (v) into short-range and long-range, which is given by:

$$\begin{aligned}v&=\frac{1}{r_{12}}=v^{sr}+v^{lr}\\&=\frac{exp(-\omega r_{12})}{r_{12}}+\frac{1-exp(-\omega r_{12})}{r_{12}}\end{aligned} \tag{2.56}$$

The functional is dependent on ω. The DFTB formalism has to be modified slightly w.r.t. the reference density matrix P_0. Energy is expanded with reference to the reference density matrix and fluctuation up to the second order. Eq. 2.38 is re-written as:

$$\begin{aligned}E_{exc}^{\omega}&=E_{exc}^{\omega}[\rho_0]+\sum_{\mu\nu}\Delta_{\mu\nu}v_{\mu\nu}^{\omega,exc}[\rho_0]\\&+\frac{1}{2}\sum_{\mu\nu\alpha\beta}\Delta P_{\mu\nu}\Delta P_{\alpha\beta}f_{\mu\nu\alpha\beta}^{\omega,exc}[\rho_0]+O(\delta\rho^3)\end{aligned} \tag{2.57}$$

where $v^{\omega,exc}$ and $f^{\omega}_{\mu\nu\alpha\beta}$ denote the first and second order derivative of the atomic orbital functional, respectively. The Greek letters denote the Slater-type atom-centered basis function (Φ_μ). Density matrix ($P_\mu\nu$) for a closed shell si is given as:

$$\rho(\mathbf{r},\mathbf{r'}) = \sum_{\mu\nu}\left[2\sum_{i=1}^{N/2} n_i c_{\mu,i} c_{\nu,i}\right]\Phi_\mu(\mathbf{r})\Phi_\nu(\mathbf{r'}) \tag{2.58}$$

After re-arrangement of the above equation:

$$\begin{aligned} E = &\sum_{\mu\nu} P_{\mu\nu}H^0_{\mu\nu} + \frac{1}{2}\sum_{\mu\nu\alpha\beta}\Delta P_{\mu\nu}\Delta P_{\alpha\beta}[(\mu\nu|\alpha\beta) + f^{\omega,exc}_{\mu\nu\alpha\beta}[\rho_0]] \\ &- \frac{1}{4}\Delta P_{\mu\nu}\Delta P_{\alpha\beta}(\mu\alpha|\beta\nu)^{lr} + E_{rep} \end{aligned} \tag{2.59}$$

where E_{rep} denotes the repulsive energy and it only depends on the reference density. The matrix elements are calculated and tabulated for various internucleic distances. Mulliken approximation is applied and four center integral are reduced and thus two-center integral becomes

$$(\mu\alpha|\beta\nu)^{lr} = \frac{1}{4}S_{\mu\nu}S_{\alpha\beta}[\gamma^{lr}_{\mu\alpha} + \gamma^{lr}_{\mu\beta} + \gamma^{lr}_{\nu\alpha} + \gamma^{lr}_{\nu\beta}] \tag{2.60}$$

$\gamma^{lr}_{\mu\alpha}$ are parameterized as in the standard DFTB, but with a long-range contribution. Finally, the Hubbard parameter in LC-DFTB is obtained as:

$$U^{LC-DFTB}_{\alpha} = \gamma^{fr}_{\alpha\alpha} - \frac{1}{2(2l+1)}\gamma^{lr}_{\alpha\alpha} \tag{2.61}$$

where $\gamma^{fr}_{\alpha\alpha}$ denotes the full-range γ integral which contains the $f^{\omega,exc}$. $\gamma^{fr}_{\alpha\alpha}$ and $\gamma^{lr}_{\alpha\alpha}$ contain the ω are a separation parameter. Moreover, l represents the angular moment of the highest occupied orbital.

2.4 Molecular Dynamics Simulation

2.4.1 Molecular Mechanics

Molecular mechanics have become very popular to envisage biological system using the laws of classical mechanics. The principle idea is to describe the energy of the system as a function of nuclear position of the system and not considering the electrons as individual particles. The potential energy of the system is measured by using empirical force field.

Force fields describes the energy of the molecules by atom specific parameters obtained by experiments or by some quantum mechanical calculations. Energy measured by force field method contains mainly two parts which correspond to the parameterization of bonded as well as non-bonded interactions between the atoms. The bonded interactions are described by the chemical bond between two atoms, angles and torsion angle of the molecules. Whereas the non-bonded interactions are described by the Van der Waals (VdW) interactions and the coulombic interaction using Coulomb's law. Van der Waals

interactions consist of two parts, namely Pauli repulsion and the London dispersion, which is described as Lennard Jones potential.

The overall equation of total energy of a force field is given as:

$$E = \underbrace{\frac{1}{2}\sum_{i} k_i (r_i - r_i^0)^2}_{E_{bonds}} + \underbrace{\frac{1}{2}\sum_{j} k_j^{\upsilon} (\upsilon_i - \upsilon_i^0)^2}_{E_{angle}} + \underbrace{\frac{1}{2}\sum_{n} V_n \cdot \cos[n\omega - \gamma_n]}_{E_{torsion}}$$
$$+ \sum_{i}^{N} \sum_{j=i+1}^{N} \left\{ \underbrace{4\epsilon_{ij} \left(\left(\frac{\sigma_{ij}}{r_{ij}} \right)^{12} - \left(\frac{\sigma_{ij}}{r_{ij}} \right)^{6} \right)}_{E_{vdw}} + \underbrace{\frac{1}{4\pi\epsilon_0} \frac{q_i q_j}{r_{ij}}}_{E_{coulomb}} \right\} \tag{2.62}$$

The first term in the above equation describes the potential energy curve of the bonded atoms, which can be measured using the Morse potential. Morse potential potential is given as:

$$V(r) = D_e [1 - exp(-\alpha(r - r_0))]^2 \tag{2.63}$$

where D_e denotes the depth of the potential energy well, r_0 denotes the equilibrium distance, $\alpha = \omega\sqrt{1/2D_e}$, μ is the reduced mass of the bonded atoms and ω is the bond vibration. Harmonic approximation is applied on the taylor expansion, at equilibrium bond length r_0. The Taylor series expansion is truncated after second order which gives the energy of the bonds (E_bonds), and κ is the spring constant.

Second term in the force field equation represents the total energy contribution due to a bonded angle of a molecule, which can be also described analogous to the harmonic potential, where υ_0 is equilibrium angle and κ_υ is bending frequency at equilibrium.

The third term in the above equation represents the energy contribution due to the torsion angle which is expressed as the periodic function of several cosine functions. V_n represents the amplitude, γ_n represents the phase shift and n is the periodicity.

The last two terms represent the energy contribution due to non-bonded atoms, which are given by VdW potential and the Coulomb potential. The VDW is given by the Lennard-Jones-(12,6) potential, whereas the electrostatic interaction is given by using the Coulomb's law. Lennard-Jones-(12,6) potential consists of two parts: First part describes the repulsive interaction at short distances by r^{-12} term and second, the attractive interactions due to the induced dipole interaction which is known as the London interaction and described as r^{-6} term.

2.4.2 Verlet integration method

Newton's second law of motion is solved numerically to progress the Molecular dynamics simulations. The second laws of equation motion is given by:

$$\frac{\partial^2 r_i}{\partial t^2} = -\frac{1}{m_i}\frac{\partial V_{pot}}{\partial r_i} = \frac{1}{m_i}\overrightarrow{F} \tag{2.64}$$

In the above equation, $\overrightarrow{F}$ is the derivative of the potential energy V_{pot}. Forces are calculated at t_0 and r_0, which are followed by calculation at new positions and new velocities at time $t + \partial t$. This is an iterative process and in every cycle the former coordinates are used to calculate the energy and force.

To obtain the new positions and velocities, Verlet integrator in the equation is used. This method uses virtual time steps in positive and negative time. Taylor expansion up to a second order of the Verlet scheme is given by:

$$r(t + \Delta t) = r(t) + v(t) \cdot \Delta t + \frac{1}{2}a(t) \cdot \Delta t^2 \tag{2.65}$$

$$v(t + \Delta t) = v(t) + \frac{1}{2}(a(t) + a(t + \Delta t) \cdot \Delta t \tag{2.66}$$

where Δt is the time step, often chosen in accordance with the fastest motion in the molecule. Usually, it should be $\Delta \leq 0.1$ of the fastest period which results most of the time step of 1fs.

2.5 Quantum Mechanics/Molecular Mechanics

Warshel and Levitt developed a Quantum mechanical method combined with a molecular method, popularly known as QM/MM which leads to efficient description of a molecule. The chemical reaction like bond breaking, bond forming or an electron transfer reaction can be explained using quantum mechanical calculations. QM methods are very expensive for large system, thus it can be applied to a small system. Thus, a combined quantum mechanical and molecular mechanics can be used to study a large system where active site calculation is done by semi-empirical, ab initio or density functional methods whereas the remaining larger part of the molecule can interact via non-covalent interactions by classical force field.

The Hamiltonian of a system with QM/MM scheme can be divided into three parts:

$$H_{tot} = H_{QM} + H_{MM} + H_{QM/MM} \tag{2.67}$$

Subsequently, the total energy of the hybrid system is given by:

$$E_{tot} = E_{QM} + E_{MM} + E_{QM/MM} \tag{2.68}$$

where E_{QM}, E_{MM}, $E_{QM/MM}$ are the energies of the QM region, MM region and QM and MM interacting system, respectively. The interaction between the QM and MM regions can be treated in various ways.

Mechanical embedding describes unpolarized interactions between QM and MM regions by the means of force field as described in the equation. Both kind bonded and non-bonded interaction between QM and MM can be described as classical force field equation. To

be specific treating non-bonding interaction between QM and MM with Lennard-Jones parameters. Furthermore, there is no Coulomb interactions between the QM and MM atoms, which leads to problems with having polar surroundings.

In order to solve the problem faced by mechanical embedding, electronic embedding is used to improve the description of the QM and MM interactions. In this case, MM atoms are allowed to polarise the atoms in the QM regions. QM atoms feel the electric potential for the atom present in the MM region, due to inclusion of the point charges of the MM atoms in the Hamiltonian of the QM calculations.

$$\hat{H}'_{QM} = \hat{H}_{QM} - \sum_{A}^{QM} \sum_{B}^{MM} \left(\frac{q_B}{r_{AB}} \right) \tag{2.69}$$

Subsequently, the total interaction energy of QM/MM region is:

$$E_{QM/MM} = \sum_{A}^{QM} \sum_{B}^{MM} \frac{Q_B \cdot q_A}{|\overrightarrow{R}_A - \overrightarrow{R}_B|} \tag{2.70}$$

Further improvement of the interaction between QM and MM atoms can be done by using polarizable embedding, where QM atoms are also allowed to polarise the MM atoms. In this case, polarizable force fields are also necessary, that the respond to the changes in the electron density. This method incurs high costs but provides high accuracy.

The highest occupied molecular orbital (HOMO) of molecules is considered to represent the site energy ϵ_i (ionization potential (IP)). The electronic couplings between HOMO's ϕ_i and ϕ_j of neighboring molecules i and j are calculated as follows:

$$T_{ij} = |\langle \phi_i | \hat{H_{KS}} | \phi_j \rangle| \tag{2.71}$$

By applying the atomic orbital (AO) basis ($\phi_i = \sum_\mu c_\mu^i \eta_\mu$) the coupling in molecular-orbital (MO) basis are evaluated as:

$$T_{ij} = \sum_{\mu\nu} c_\mu^i c_\nu^i \langle \eta_\mu | \hat{H_{KS}} | \eta_\nu \rangle = \sum_{\mu\nu} c_\mu^i c_\nu^i H_{\mu\nu} \tag{2.72}$$

The effect of environment, i.e., the electrostatic interaction with the remainder molecules is taken into account as classical point charges (the second term in the parentheses).

$$H_{\mu\nu} = H^0_{\mu\nu} + \frac{1}{2} S^{\alpha\beta}_{\mu\nu} \left(\sum_\delta \Delta q_\delta (\gamma_{\alpha\delta} + \gamma_{\beta\delta}) + \sum_A Q_A \left(\frac{1}{r_{A\alpha}} + \frac{1}{r_{A\beta}} \right) \right) \tag{2.73}$$

3 Fundamentals of charge transfer in organic semiconductors

In this chapter, a fundamental background of the charge transfer in the amorphous organic semiconductors is presented. Section 2.1 gives a summary of the electronic structure of amorphous organic material which leads to charge hopping between two localized states. Section 2.2 explains about the charge hopping mechanism in amorphous organic materials. Further, Section 2.3 introduces the Marcus hopping rates for charge and energy transport using the quantum mechanical approach.

3.1 Electronic structure of OSCs and OLEDs

Organic semiconductors materials are generally formed by the small covalently bonded organic molecules. These materials are mostly made up by carbon and hydrogen atom along with a few hetero-atoms such as oxygen, nitrogen and sulfur. These materials absorb and emit light in the visible spectrum and their conductivity is sufficient for the operation of semiconductor devices such as light-emitting diodes and solar cells. Despite they show semiconducting properties, but still the semiconducting nature varies strongly between organic and inorganic materials.

Traditional inorganic semiconductors such as silicon and germanium have low band gaps. Free charge can be created by thermal excitation from valence band to conduction band. Intrinsic conductivities of inorganic semiconductors are in the range of 10^{-8} to 10^{-2} $\Omega^{-1}\ cm^{-1}$. Dielectric constant for these materials is large ϵ_r = 11, thus the coulomb effect between electrons and holes are insignificant due to dielectric screening. Consequently, light absorption at room temperature can create free electron and hole.

On the contrary, organic semiconductors are extrinsic in nature which result from the formation of electron-hole pairs due to absorption of the light. In this case, absorption and emission take place in the range of 600 - 400 nm, which creates significant charge carrier concentration at thermal excitation at room temperature. Moreover, dielectric constant is low which is around ϵ_r = 3.5. Thus, coulombic interaction can be ignored, which is significant. It also implies that electron-hole pair generated by optical excitation is bound by a coulomb energy of about 0.5 - 1.0 eV. Thin film of OSCs can be made by vacuum sublimation, ink-jet printing and spin coating. Broadly, organic semiconductor materials can be classified into three categories.

1. Amorphous organic films are created by organic molecules deposited as amorphous molecules through the process of evaporation or spin coating. These type of materials are used in devices like LED and molecularly doped polymer (MDP).

2. Molecular crystals films consist of a lattice and a basis. Molecules such as polyacenes in particular naphthalene and anthracene, can form the basis of the molecular crystal, which is held together by weak van-der-Waal interactions. The charge mobilities are higher in comparison to the noncrystalline organic materials, which makes it suitable for the use in transistor applications.

3. Polymer films can be considered as the repeated unit of covalently bonded molecules. These are usually processed from solution, which allows the deposition techniques including ink-jet deposition and spin-coating. These type of films are suitable for the blending due to thermodynamic stability.

In order to conduct electricity, both electrons and ions can be served as charge carriers for the conductivity inside any organic or inorganic solids. These materials can be regarded as good or bad electrical conductors based on the energy gap between the valence band and conduction band. As far as organic semiconductors are concerned, the energy gaps between the valence band and the conduction band is not high. Thus, it is possible to overcome this energy gaps by thermal process or chemical doping of the semiconductors.

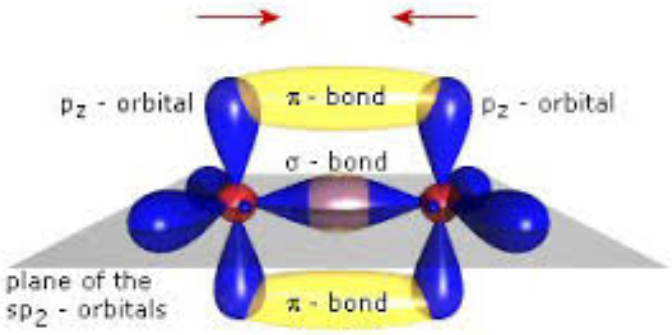

Figure 3.1: Illustration of the formation of delocalized π orbitals in ethene. Both carbon atoms contribute in the formation of sp^2 (s, p_x and p_y) hybrid orbitals. These hybrid orbitals are aligned in the xy-palne, whereas p_z orbital is perpendicular to the sp^2 plane. (source:https://www.heftfilme.de/)

Organic materials conduct electricity due to excess or vacancy of electron which are free to move across the solids. Electrons present in the sp^2 hybrid orbitals are aligned in the plane with an angle of 120°. Organic conducting molecules have π - electrons which are delocalised out of the plane, which is formed by the p_z orbitals of the carbon atom.

It is important to have a small energy gap between valence band and the conduction band respectively derived from the highest occupied molecular orbital (HOMO) and the lowest unoccupied molecular orbital (LUMO) of the organic molecules, to be a good candidate semiconductor.

With increasing number of carbon atoms and the π-electrons, the energy levels of the delocalized π orbital's will get closer due to larger overall splitting among the π orbitals.

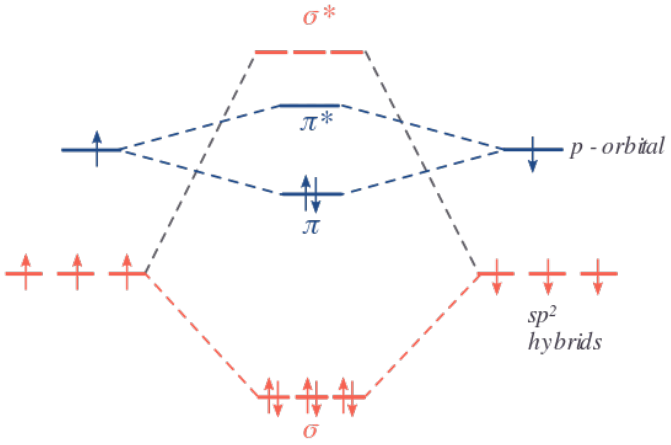

Figure 3.2: Illustration of the energy between the HOMO and LUMO in ethene. The gap between the HOMO and LUMO determines the semicondution nature of the organic material. (source:https://chem.libretexts.org/)

consequently, the gaps between the valence band and the conduction band decrease. Therefore, the energy gaps between the HOMO and LUMO lead to smaller energy gaps.

In small molecular organic semiconductors, band structures are evolved and charges are localised over the several molecules. Due to amorphous nature of the material, it has spatial disorder which leads to unique morphology. The disorder in an amorphous solid can be given by the Gaussian distribution and the corresponding energy levels of different molecules is given by the below equation:

$$D_s(E) = \frac{n}{\sqrt{2\pi}\sigma_s} \exp -\frac{(E_s - E)^2}{2\sigma_s^2} \tag{3.1}$$

where n is the number density, σ_s is the standard deviation of the distribution, E_s is the average value of energy levels over all the molecules. Due to different environments of each molecule in amorphous organic materials, the energy levels are shifted. Weak electronic coupling of π-systems of different molecules lead to another phenomenon called Anderson localization on individual molecules. Since π orbitals are delocalised over the entire molecule, occupied π-orbitals can donate their electrons and unoccupied π-orbitals can accept the electrons. Consequently, the overlap of wave function between the π orbitals of different molecules can lead to the hopping of charge from one molecule to another.

3.2 Charge hopping in amorphous organic materials

In disordered organic semiconductors, the reorganization of the molecule upon charging prevents the hybridisation between the different electronic state, due to weak van der waals and electronic coupling interactions. This leads to strong localization of charge in a molecular semiconductor thus charge transfers from one site to another is possible if there

is sufficient quantum-mechanic overlap between the two states. The process of transfer from one localised state to another is generally referred as "hopping". One electron state on different small molecules are coupled weakly and the hopping rate can be calculated by Fermi's Golden rule.

$$\omega = \frac{2\pi}{\hbar} \sum_i \sum_f p_i \langle \psi_f | H | \psi_i \rangle^2 \delta(E_f - E_i) \tag{3.2}$$

where i and f represent initial and final states and p_i is the occupation probability of the initial state, $\langle \psi_f | H | \psi_i \rangle$ is the coupling wave function between the initial and the final state and $\delta(E_f - E_i)$ is the resonance condition for the energy transfer.

In the case of polaronic transport between the identical molecules, there is no difference between a forward jump from i to j or vice-versa. Both sites have the same polaronic binding energy and isoenergetic, which lead to the same hopping rate for the forward and backward jumps. This symmetry is broken when static energetic disorder is introduced into the semiconductor. Consequently, the forward and backward jumps will no longer be the same. In such disordered medium, the use of dipole coupling can be appropriate to describe the incoherent hopping of excitons. This approximation is expressed by Miller and Abrahams:

$$\omega_{if} = \omega_0 J_{if}^2 \begin{cases} exp - \dfrac{(E_f - E_i)}{k_B T} & E_f > E_i \\ 1 & E_f \leq E_i \end{cases} \tag{3.3}$$

where i and f are the initial and final electronic states and E_f and E_i are the final and initial total energies, respectively. J_{if}^2 denotes the electronic coupling, T is the temperature and k_B is the Boltzmann constant. For the downhill hopping, the excess energy is dissipated while for uphill hopping, an activation energy is required in the form of Boltzmann factor. This introduces an energy dependence which need to be multiplied with the hopping rate due to the electronic coupling between the two sites. This approximation assume that the Boltzmann factor is equal to 1 for the downhill hopping.

Hopping transport can also be quantitatively described in several other ways. Modeling approach such as master equation approach (ME) can be used to describe the amorphous system in a coarse grained fashion. In advanced approaches, a distribution of points are used which follows the same neighbouring molecules as the center of mass position in disordered material.

The below equation describes the time derivative of the occupation probability:

$$\frac{dp_i(t)}{dt} = \sum_j (p_j(t) Jk_{ji} - p_i(t) Jk_{ij}) \tag{3.4}$$

where $p_i(t)$ and $p_j(t)$ are the occupation probabilities at site i and j, respectively. The term $p_j(t) Jk_{ji}$ describes the probability flux from neighbouring site j to site i whereas $p_i(t) Jk_{ij}$ describes the probability flux away from site i to neighbouring site j. $k_i j$ denotes the hopping from site i to site j. This equation can be solved analytically as well as numerically.

Another modelling approach is the Kinetic Monte Carlo (KMC) method where all charge hopping processes are modelled explicitly. In this case, certain number of electrons are distributed in the system and rates k of all possible process are calculated. One rate is chosen with a probability corresponding to the sum of all the rates. Further, chosen step is carried out and time is updated and this way, a random but representative trajectory of the system is obtained. This trajectory obeys thermodynamic laws and it can used to extract important information such as equilibrium charge density, charge mobility and percolation path.

A more detailed and advanced hopping rate is given by Rudolph A. Marcus where he describes how an electron transfers from a donor to an acceptor molecule in a solution. Marcus theory of charge transfer will be explained in detail in the next section.

3.3 Marcus theory of electron transfer

Marcus theory was originally proposed by Rudolph A. Marcus in 1956 to explain the rate of electron transfer processes taking place in a solution. Since its development, the Marcus theory has been applied in a number of important processes in chemistry, biology, solar cells and many more. This theory can also be applied to describe the charge transfer process in localized states in organic semiconductors.

Marcus considered the electron transfer to progress via a solvent rearrangement coordinate, such that solvent reorganise itself in the direction of the field of charge, which is termed as orientation polarisation. At the same time, atoms and electron in the solvent are slightly displaced from their initial position. Marcus emphasised that the system will fluctuate in the conformational transition state where either of the charges species are in resonance. This implies that energy is conserved during the process and the Franck-Condon principal is hold true.

Marcus theory uses the concept of parabolic approximation of the Gibbs free energy of the system as a function of multi-dimensional reaction coordinate ($\bar{q}$). In case of frozen, molecular orientation such as in condensed amorphous system, entropic contribution is negligible. Thus, total energy of the entire system can be approximated for the calculation of the Gibbs free energy.

The energy barrier or the activation energy for the electron transfer is calculated by the below equation:

$$E_A = \frac{1}{4\lambda}(\lambda + E_f - Ei)^2 \tag{3.5}$$

where E_A denotes the activation energy barrier, λ is the reorganisation energy (energy required for the vertical electron transfer without change of the nuclear frame) and $E_f - E_i$ is the difference of the energies between the final and the initial states for the charge transfer process. The activation energy for the entire process can be calculated as the intersection of the two parabolas. Marcus formulated the hopping rate [19, 20, 21, 22] using the Boltzmann occupation ratio, which is given as:

$$k = \frac{2\pi}{\hbar}\left\langle |H_{if}|^2 \right\rangle \frac{1}{\sqrt{4\pi\lambda k_B T}} exp\left(- \frac{(\lambda + \Delta E)^2}{4\lambda k_B T} \right) \tag{3.6}$$

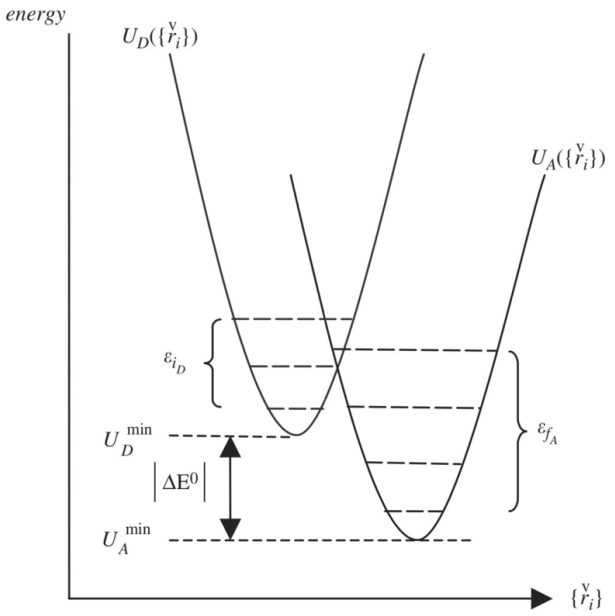

Figure 3.3: Donor and acceptor potential surfaces and accepting mode vibrational energies (Reprinted from [24]).

where T_{DA} is the electronic coupling between the initial and the final states and ΔE is the total free energy change for the electron transfer reaction. The Marcus rate theory (eq. 2.6) is valid when the difference of the internal and external phonons are small as compared to the thermal energy of the environment ($\hbar\omega << kT$). The energy difference between initial and final states of the system in the Marcus theory, is equivalent to the effects of energetic disorder in a polaron model. The nonadiabatic ET rate, Eq. 5.2, takes both vibrational overlap and the electronic coupling between reactant and product states into account (Fig. 3.3). $|D\rangle$ and $|A\rangle$ are the D and A electronic states and P_{i_D} represents initial vibrational population at thermal equilibrium of state i when the electron is on the donor. The total energies of $|i_D\rangle$ and $|f_A\rangle$ are $U_D^{min} + \varepsilon_{i_D}$ and $U_A^{min} + \varepsilon_{f_A}$, consisting of the minimum electronic state energies (U_D^{min} / U_A^{min}) and vibrational state energies (ε_{i_D} / ε_{f_A})[23]. The DA electronic coupling T_{DA} is the overlap between the initial and final vibrational levels (the total initial to final vibronic state coupling). The electronic part $|\langle i_D|\hat{T}|f_A\rangle|^2$ indicates that the molecular structure with large T_{DA}^2 contributes to k_{ET} more efficiently.

In the following sections, detailed explanations of the molecule and system dependent parameters such as electronic coupling (H_{if}), reorganisation energy (λ) and energy difference (ΔE) are provided, which are required for the Marcus rate calculation.

3.3.1 Electronic coupling

For electron transport in a disordered system, electronic coupling between two states can be calculated using the Löwdin orthogonalization method. In this case, HOMO represents

the wave function of the missing electron(hole), whereas the LUMO represents the wave function of electron. The electronic coupling T_{ij} is calculated as given below:

$$T_{if} = \frac{\hat{H}_{if} - \frac{1}{2}(\hat{H}_{ii} + \hat{H}_{ff})S_{if}}{1 - S^2{}_{if}} \tag{3.7}$$

where $\hat{H}_{ii}$ represents HOMO or LUMO eigenvalues of molecule A, $\hat{H}_{jj}$ represents HOMO or LUMO eigenvalues of molecule B, $\hat{H}_{ij}$ represents the matrix elements calculated using Fock and overlap matrices of molecule A and B. $\hat{H}_{ij}$ matrix elements are given by :

$$\hat{H}_{if} = \langle \phi_i | \hat{H}_{PQ} | \phi_f \rangle \tag{3.8}$$

where $\hat{H}_{PQ}$ denotes the effective Hamiltonian of the neutral dimer system, ϕ_i and ϕ_f represents the HOMO (LUMO) orbitals of the molecule A and B. S_{if} is the overlap matrix element of the HOMO (LOMO) orbitals.

$$S_{if} = \langle \phi_i | \phi_f \rangle \tag{3.9}$$

The basis function of the molecule A and molecule B are non-orthogonal and thus it is non-zero.

3.3.2 Reorganization energy

Reorganisation energy (λ) is the energy cost due to the geometry modification while going from a neutral to charge molecule in presence of a solution. Lower the reorganisation term, implies the lower the geometrical modification and vice-versa and thus higher the chances of electron transfer. For example, if the initial ionized molecule have the same geometry as that of the geometry of the final neutral molecule, then the electron transfer will happen swiftly, without waiting for the vibration. Similarly, if the difference between the geometry between the initial and the final molecule is more, then the electron transfer will only happen if there is vibration or thermal fluctuations.

As stated in the equation 3.5, reorganisation of the charge transfer between two states can be calculated using Nelsen's four-point-procedure. So for the calculation of the reorganisation energy, the charge transfer has to be partitioned into different processes, which decouple the fast electronic process from the slower ionic response of the system. This procedure is generally regarded as the Nelsen's four-point-procedure and described as follows:

1. Total energy (E_i) of the confrontationally relaxed molecule in vacuum is calculated.
2. An electron is added to the molecule to step 1 and total energy (E_{ur}) of the molecule is calculated.
3. In third step, step 2 structure is relaxed and total energy (E_r) of the relaxed structure is calculated.
4. In the last step, extra electron is removed from the step 3 structure and total energy (E_f) is calculated.

Finally, the reorganisation energy of a system is given by the below equation:

$$\lambda = (E_{ur} - E_r) + (E_f - E_i) \tag{3.10}$$

Reorganisation energy can be separated into two parts,inner part λ_{inner} as well as outer part λ_{outer}. The λ_{inner} includes the relaxation of the donor and the acceptor molecules, whereas the λ_{outer} includes the relaxation from the environment. If the electron transfer happens between two different types of systems then the overall reorganisation energy is given by:

$$\lambda_{1,2} = \frac{1}{2}(\lambda_{1,1} + \lambda_{2,2}) \tag{3.11}$$

where $\lambda_{1,1}$ and $\lambda_{2,2}$ are the reorganisation energies between two different types of molecules 1 and 2, respectively.

3.3.3 Site energy

The rates of charge transport are generally determined by onsite energy difference between the molecules. The difference of electron affinity (EA) from hopping site i to hopping site f is given by:

$$\Delta EA_{if} = [EA_f^0 + |q|\Phi_f^{dyn}] - [EA_i^0 + |q|\Phi_i^{dyn}] + |q|\vec{F} \cdot \vec{r_{if}} \tag{3.12}$$

where q denotes the electron charge, EA_x^0 denotes the electron affinity of the specific molecule x at zero charge concentration, Φ_x^{dyn} is the electrostatic charge potential at the site x which is developed by the other neighbouring charges in the given boundary condition, $\vec{F}$ is the electric field applied and r_{if} is the direction from site i to site f. Similarly, the Ionization potential (IP) difference for a hopping from site i to site f is given by:

$$\Delta IP_{if} = [IP_f^0 + |q|\Phi_f^{dyn}] - [IP_i^0 + |q|\Phi_i^{dyn}] + |q|\vec{F} \cdot \vec{r_{if}} \tag{3.13}$$

All the terms in the equ. 3.13 represent the same parameters which are used in the equ. 3.12 except the term IP_x^0, which represents the ionization potential of molecule x at zero charge concentration.

Quantum patch method is used to calculate the EA_x^0 and IP_x^0 for a sample of few hundred molecules. In an isotropical material, onsite energy is assumed to follow a Gaussian distribution which is given by:

$$g(E) = \frac{1}{\sigma\sqrt{2\pi}} e^{-\frac{E^2}{2\sigma^2}} \tag{3.14}$$

There are two contributions to the site energy, first due to the conformational changes or disorder and the second contribution is due to the inhomogeneous electrostatic potential which is created by another neighboring molecule.

The electrostatic contribution to the EA/IP on site i considered as first order due to the monopol-dipole interactions which results from the added charge with the dipole moments of the environment.

$$V^{EA^0/IP_i^0} = \pm \sum_{f \neq i} \frac{|q|}{4\pi\epsilon_0\epsilon_r} \frac{\vec{r_{fi}} \cdot \vec{d_j}}{|r_{if}|^3} \tag{3.15}$$

where sum is taken over all the molecules and $\vec{d_f}$ denotes the dipole moment of the molecule f and r_{if} is the distance between f and i. In the similar way, neighbouring sites also feels the similar electrostatic environment, which is spatially correlated.

4 Understanding excited state properties of host materials in OLEDs

Chapter 4 is reprinted with permission from Ref. [25]:

- Samaneh Inanlou, Rodrigo Cortés-Mejıa, Ali Deniz Özdemir, Sebastian Höfener, Wim Klopper, Wolfgang Wenzel, Weiwei Xie, and Marcus Elstner. "Understanding excited state properties of host materials in OLEDs: simulation of absorption spectrum of amorphous 4, 4-bis (carbazol-9-yl)-2, 2-biphenyl (CBP)". In: Physical Chemistry Chemical Physics 24.7 (2022), pp. 4576–4587.

Author Contributions: This work was done in cooperation with Ali Deniz Özdemir and Rodrigo Cortés-Mejıa. Ali Deniz Özdemir generated the amorphous morphology of OSCs. Rodrigo Cortés-Mejıa performed Bethe–Salpeter equation (BSE) method from the GW approximation (GW-BSE) to assess the accuracy of TD-LC-DFTB. Samaneh Inanlou computed the absorption spectrum and performed QM/MM MD simulations.

4.1 Introduction

Nowadays, organic light-emitting diodes (OLEDs) have been considered as a new generation of technologies due to their high brightness, low-cost, low energy consumption, light weight and mechanical flexibility [26, 27, 28, 29]. They can be used in many devices such as televisions, mobile phones, and other lighting resources [30, 31]. Among different types of OLEDs, the phosphorescent OLEDs (PhOLEDs), serving as the second-generation OLEDs, have recently attracted much attention because they can generate light from both singlet and triplet states and thus allow the internal quantum efficiency to reach nearly 100% [32, 33]. In PhOLEDs, the heavy metal-based phosphorescent emitter is doped in an appropriate host material, which is used to transfer excitation energy to the emitter and confine the exciton in the emissive layer.

Amorphous materials have been widely used as host materials in PhOLEDs, because the emitter is uniformly distributed in the amorphous matrix to minimize the concentration quenching effect [34]. In addition, the absence of grain boundaries in amorphous materials further minimizes the exciton recombination [35]. The excited-state properties of the host material play an important role in photoluminescence characteristics of OLEDs. For instance, it has been found that the excited-state molecular aggregation in the vicinity of host material/emitter layer interfaces limits the operation lifetimes of PhOLEDs [36]. Therefore, the fundamental understanding of the excited-state properties of host materials

is the key for the design of highly efficient PhOLEDs. In the present work, we explore the excited-state properties of a representative host material using reliable and efficient quantum chemistry methods. Hence, we obtain an accurate description of excited states energies and exciton couplings, where the phase space has been sufficiently sampled.To achieve this, we first benchmark semi-empirical quantum chemical methods, the so-called density functional based tight-binding method (DFTB), as well as its long-range corrected version called LC-DFTB, which allows us to describe excited state properties with reasonable accuracy.

In the past decades, DFTB has been used as an alternative to the widely used density functional theory (DFT) to compute molecular properties. DFTB is 2–3 orders of magnitude faster than DFT and can reach the accuracy of DFT methods by using careful parameterization approaches [37, 38]. However, DFTB uses semilocal PBE functionals [39, 40] for calculations of the Hamiltonian matrix and thus inherits the errors of typical DFT functionals using generalized gradient approximations (GGA) [41, 42]. Recently, the LC-DFTB approach was developed by the incorporation of arbitrary LC functionals in the DFTB to partly cure the DFT-GGA errors [43]. The time-dependent scheme of LC-DFTB (TD-LC-DFTB) has been successfully parameterized and benchmarked for a test set of small organic molecules involving charge-transfer excitations [44], rhodopsins and light-harvesting complexes [45] and biological molecules. In the present study, we will examine the quantitative accuracy of TD-LC-DFTB in calculating the absorption spectra of a most widely used host material in PhOLEDs, [32, 46] 4,4- bis(9-carbazolyl)-biphenyl or CBP.

By combining classical MD simulations with quantum mechanical/molecular mechanical methods (QM/MM), where the DFTB methods are used in the QM part, we will be able to address the effects of static and dynamic disorders on the absorption spectra of CBP. The paper will proceed as follows: first, the benchmark calculations of TD-LC-DFTB approach are performed by comparing the excitation energies of CBP molecules using various quantum chemistry methods. Second, the absorption spectra of CBP in the gas and condensed phase are computed using TD-LC-DFTB and different structure sampling methods are discussed. Finally, the aggregation effect on the optical properties of amorphous CBP has been addressed.

4.2 Methodology

4.2.1 Benchmark of TD-LC-DFTB

The bond length alternation (BLA) is defined as the difference in average single and double bond lengths along extended p systems. In the present study, the p-conjugated chain marked with red color in Fig. 4.1b is used to evaluate BLA of CBP. To compare the accuracy of different quantum chemistry methods, geometry optimizations of CBP molecule at the ground state are performed using HF, DFT functionals (B3LYP, PBE, ωB97XD) and MP2 with 6-31+g* basis set, respectively. The geometry optimization using DFTB is performed using the third-order DFTB (DFTB3) with 3OB parameter set [47]. In the constrained optimizations, the central, side and improper dihedral angles are fixed at 45°, 60°and 0°,

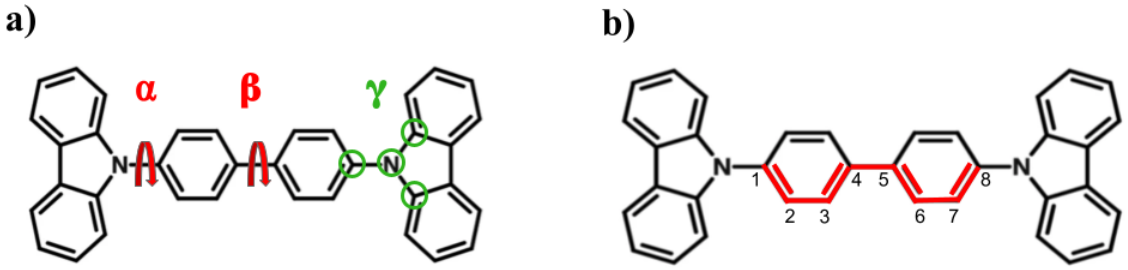

Figure 4.1: (a) Schematic representation of the 4,4'-bis(N-carbazolyl)-1,1'- biphenyl (CBP). α , β and γ are the side dihedral angle, central dihedral angle, and improper dihedral angle. (b) Marked bonds in red are considered in calculation of BLA.

respectively, which are obtained by fully optimization by ωB97XD/6-31+g*, while the other degrees of freedom are relaxed. The excitation energies are computed using CIS, TD-DFT, ADC(2), CC2 and the Bethe–Salpeter equation (BSE) from the GW approximation (GW-BSE) method with 6-31+g* basis set and TD-LC-DFTB with mio-0.8 parameter set, [48] respectively. All DFTB and TD-LC-DFTB calculations in the present study are performed using the DFTB+ program suite[49], if not specified otherwise. The GW-BSE and ADC(2) calculations are performed using the TURBOMOLE v7.4 computational chemistry package [50]. All other calculations are carried out with the GAUSSIAN 09 package [51].

Recently, the gas phase single-point absorption spectrum of CBP has been studied using GW-BSE method [52]. The GW-BSE method is an accurate and reliable approach for calculating the excited-state properties of extended systems [53, 54] and thus it is used to assess the performance of TD-LC-DFTB in this work. Therefore, the geometry is adopted from ref. [52] which is optimized at the ground state using PBE0 functional [55] with the def2-TZVP basis set [56, 57] . Afterward, vertical excitation energies and oscillator strengths of the lowest 25 excited singlet states are computed using TD-LC-DFTB with mio-0.8 parameter set. The energy lines are broadened by a Lorentzian function with a width of 0.05 eV and summed up to provide the absorption spectra normalized to the highest peak. Note that the inclusion of the dielectric screening into LC corrected functional can lead to significant shifts in the condensed-phase adsorption spectra. However, we would expect that the inclusion of the dielectric screening makes negligible differences in the adsorption spectra for the systems with strongly localized excitations. The small exitonic couplings between the CBP monomers (shown below) indicates that the localized electronic structure of CBP, which justifies the use of LC corrected functional with bare (i.e., unscreened 1/r) electron–hole interaction.

The self-consistent eigenvalue-only GW method with def2-TZVP basis set is performed to benchmark the accuracy of TD-LC-DFTB for the calculation of the adsorption spectrum of CBP. We use the spectral representations for the response and Green's function [54, 58], which enables an analytic evaluation of energy integrals and derivatives. The advantage of this approach is that it avoids the uncertainties that may arise from the widely used plasmon-pole models and prevents additional computational parameters needed in numerical frequency integration methods.

4.2.2 Molecular dynamics simulations

The force field parameters are taken from the general AMBER force field (GAFF) [59, 60], where the atomic charges are generated by the restrained electrostatic potential [61, 62] fitting procedure (RESP) calculated at the HF/6-31g* [63, 64] level using the Gaussian 09 package [51]. The force field parameterizations are imposed on two types of dihedral angles (see Fig. 4.2). The first are the proper dihedral angles between two central phenyl groups and the dihedral angle between carbazole moiety and phenyl group (henceforth, referred to as "central angle" and "side angle" or α and β) and the second type is improper dihedral angles (referred to as γ). The dihedral constants for α, β and γ are parametrized by fitting to the relaxed potential energy scan along each angle using ωB97XD/6-31+g* method.

4.2.2.1 Force field reparameterization

This section presents the reparametrization of dihedral angles which is restricted to the proper and improper dihedral angles. The reason behind this is that the excitation energies and consequently the absorption bands can be affected by the dihedral angles. Force-field reparameterization can be performed by matching the quantum mechanical potential energy surface (PES) scans with the corresponding force-field based scans. To reparametrize the parameters of the general AMBER force field (GAFF), three sets of parameters are considered: side/central dihedral angles (α and β) and improper dihedral angle (γ) (Fig. 4.1a).

The potential energy scans for the corresponding angles are performed using density functional theory (DFT) methods (ωB97XD functional) and 6-311g+(d,p) basis set. The potential energies are obtained from rotational scans where the corresponding angle is fixed (e.g., α in Fig. 4.1). Throughout the calculations, all the geometrical parameters are simultaneously relaxed while their respective dihedral angles vary from 0° to 180° for side and central angles and from 0° to 30° for improper angles in steps of 5°. The difference between DFT and force-field based energies is then fitted, yielding the parameterization constants of the dihedral using the GAUSSIAN package, and all force-field computations are carried out using the GROMACS package. For the proper and improper dihedral angles, the periodic and harmonic functions are used as per equations 4.1 and 4.2, respectively.

$$V_d(\phi_{ijkl}) = k_\phi(1 + \cos(n\phi - \phi_s)) \tag{4.1}$$

$$V_{id}(\zeta_{ijkl}) = \frac{1}{2}k_\zeta(\zeta_{ijkl} - \zeta_0)^2. \tag{4.2}$$

After fitting, the coefficients of the periodic and harmonic functions (k) for side (α), central (β) and improper (γ) dihedral angles are 4.25, 2.883 and 11.88 respectively. The results are shown in Fig. 4.2b). For the side angle, the DFT scan shows that the torsional potential has 2 minima when $\alpha \approx 60°$ and another local minimum at $\alpha \approx 120°$. The geometry at $\alpha \approx 90°$ has a barrier to planarity of about 3 kcal/mol. Concerning the central angle, the rotational barrier at 0° and 90° of biphenyl originate from two factors, the interaction between π orbitals of the benzene rings, which makes biphenyl planar and repulsion between ortho-hydrogen atoms to makes the molecule to rotated the geometry with $\beta \approx$

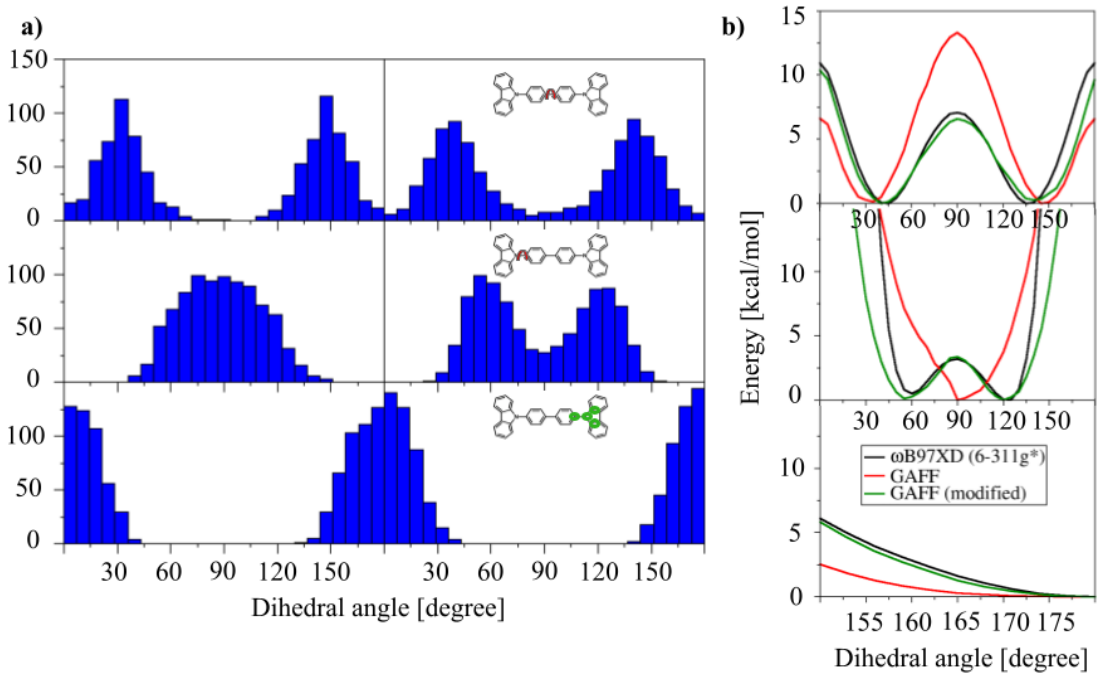

Figure 4.2: a) Distributions of central (upper panel), and side (center panel) and improper (lower panel) angles obtained by MD sampling using original GAFF and reparameterized GAFF force fields. b) Potential energy relaxed scans along central (upper panel), and side (center panel) and improper (lower panel) angles using ωB97XD/6-311g+(d,p) (black) and original GAFF (red) and reparameterized GAFF (green).

40° or 140° [65]. The barrier at $\beta = 90°$ is about 6 kJ/mol. For the improper angle, as the out-of-plane angle decreases, the electronic conjugation increases. Therefore, the planar geometry ($\gamma \approx 0°$ or 180°) has an extended electronic conjugation of π-electrons which facilitates extended conjugation of CBP. The rotational barrier at $\gamma \approx 30°$ or 150°, is a result of breakage of the electronic conjugation.

The van der Waals (vdW) interactions are represented by a 6–12 Lennard-Jones potential,

$$E_{nonbonded} = \sum_{nonbonded} \varepsilon \left[\left(\frac{R_{min,ij}}{r_{ij}} \right)^{12} - 2 \left(\frac{R_{min,ij}}{r_{ij}} \right)^{6} \right] \tag{4.3}$$

where the parameters ϵ and $R_{min,ij}$ are derived from the GAFF force field. Since we take the structures from the MD-trajectories, vdW effects are included. This also holds for the QM/MM simulations, where the vdW interactions are included in the QM/MM Hamiltonian.

In gas-phase classical MD simulation, a CBP molecule is first minimized using the steepest descent algorithm and then equilibrated at 300 K for 5 ns with a time step of 1 fs. The Nose–Hoover thermostat [66] is employed to control the temperature. 5000 structures are saved during the equilibrium simulation. For each CBP structure, 25 excitation energies are computed using TD-LC-DFTB and the absorption spectrum is given by the sum of

all energy lines broadened by a Lorentzian function with a broadening width of 0.05 eV. In the present study, all classical MD simulations are carried out using the GROMACS (version 2016.3) program package [67] unless stated otherwise.

A disordered thin-film morphology of 5000 CBP-molecules is generated by simulating physical vapor deposition, based on a Monte-Carlo (MC) protocol. During the deposition process, molecules are added to the simulation box (L_x = L_y = L_z = 90 Å) one after another where the flux of molecules is parallel to the z-axis and the xy-plane represents the surface of the substrate. The deposition simulation starts with a molecule at a random initial position, followed by 32 simulated annealing (SA) cycles. Within each SA-cycle, the molecules' conformation space is sampled by 130 000 MC-steps, where only molecule translations or rotations of a dihedral ($\alpha or \beta$) are considered. Based on a Metropolis criterion, MC moves are accepted and stored or rejected, where the temperature at MC-step n is given by $T_n = T_s c^n$. The $c = (T_e/T_s)^{1/N}$ determines the cooling rate as per MC step, T_s= 4000 K and T_e= 300 K denote the start- and end-temperature, respectively. After the SA-cycles are performed, the conformation with the lowest energy is accepted as the final conformation. Subsequently, the electrostatic and Lennard- Jones potential are updated. This procedure is repeated 5000 times until all molecules are deposited [68]. After deposition, an equilibrium simulation of 2 ns at 300 K and 1 bar is performed to equilibrate the temperature and pressure. The Nose–Hoover thermostat [69] and Parrinello–Rahman barostat [70] are employed to obtain a reasonable canonical ensemble.

The absorption spectra of CBP in the condensed phase are simulated using two initial sampling methods, ensemble sampling and time-series sampling. In the former approach, the vertical excitation energies of 25 excited states are computed using TD-LC- DFTB for each monomer (5000 in total) in the equilibrated CBP supercell and summed up to generate the absorption spectra. In the time-series sampling, the absorption spectra are simulated using the structures of a specific CBP molecule in 5000 snapshots uniformly selected along 5 ns MD simulation. In both cases, the electrostatic effects from the environment on the excitation energies are considered by including the MM point charges in the DFTB calculation.

In the quantum mechanics/molecular mechanical molecular dynamics (QM/MM MD) simulations, the whole system is divided into a quantum mechanical (QM) region, containing only one CBP molecule treated by DFTB3 with 3OB parameter set, and molecular mechanical (MM) region, where the remaining CBP molecules are treated on a molecular mechanics (MM) level using the modified GAFF. The equilibrated supercell obtained from the classical MD simulation is used as a starting point for a 1 ns QM/ MM simulation with a time step of 1 fs, where 5000 snapshots are taken as reference structures for the excited-state calculations of the CBP molecule in the QM region. The QM/MM MD simulations are performed with the GROMACS program package [71]. The excitation energy calculations including the effects of the electrostatic interactions from the environment are carried out with the DFTB+ program suite [49]. The experimental data [72] are digitized using the open-source tool WebPlotDigitizer [73].

The static and dynamic properties of molecular aggregations are described by the excitonic coupling between the excited states of monomers. Excitonic couplings are conventionally composed of the long-range Coulomb contributions and the short-range (exchange and overlap) contributions. In the present work, only the Coulomb contributions

are considered and the complete evaluation of excitonic coupling is planned for the future. The Coulomb coupling can be determined as the interactions between the atomic transition charges of monomers [74]. The Coulomb coupling with the nearest neighbour is considered in the present study. The atomic transition charges are computed using the TD-LC-DFTB method implemented in the DFTB+ program suite [49]. Recently, TD-LC-DFTB excitonic couplings have been successfully benchmarked for rhodopsins and light-harvesting complexes [45].

4.3 Results

Optical properties of CBP have been studied in detail in a recent work [52], where the performance of DFT approaches has been compared with GW-BSE estimates. As described for many other molecules, standard DFT-GGA and even several hybrid DFT functionals such as B3LYP or PBE0 suffer from the delocalization error, which renders their prediction for many molecules of interest unreliable. Especially for charge-transfer excited states, excitation energies are severely underestimated, which is also the case for CBP. Range-separated DFT functionals, however, can systematically improve the description of these states. In the following, TD-LC-DFTB will be tested and applied for the description of CBP excited states.

4.3.1 Bond length alternation and excitation energies

Excitation energies of conjugated organic molecules are very sensitive to the molecular structure. Dihedral angles and the BLA are two parameters which have a sizable impact on excitation energies. Recently, the importance of these structural details for excitation energies has been discussed in detail [45]. For CBP, different quantum chemical methods predict slight differences in the central geometrical parameters, as can be seen from Table 4.1. The calculated bond lengths and BLAs are listed in the Table. 4.2.

	DFTB	MP2	PBE	B3LYP	ωB97XD	HF	FF
BLA	0.014	0.017	0.020	0.021	0.025	0.031	0.036
α	43.3	53.0	53.3	56.9	55.8	94.2	54.4
β	28.0	39.4	37.4	39.0	42.0	43.4	41.9
γ	0.0	0.0	0.0	0.0	0.0	0.3	0.0

Table 4.1: Bond length alternation and dihedral angles for the CBP molecule optimized by various quantum chemistry methods. The bond length alternation is defined in Fig. 4.1b.

	Bond length [Å]							BLA
	$C_1 = C_2$	$C_2 - C_3$	$C_3 = C_4$	$C_4 - C_5$	$C_5 = C_6$	$C_6 - C_7$	$C_7 = C_8$	
FF	1.410	1.400	1.399	1.514	1.393	1.402	1.410	0.036
HF	1.388	1.380	1.382	1.488	1.382	1.380	1.389	0.031
ωB97XD	1.393	1.383	1.389	1.480	1.389	1.383	1.393	0.025
B3LYP	1.399	1.387	1.394	1.480	1.394	1.387	1.399	0.021
PBE	1.395	1.383	1.391	1.474	1.391	1.383	1.395	0.020
MP2	1.397	1.390	1.402	1.471	1.402	1.390	1.397	0.017
DFTB	1.408	1.392	1.408	1.484	1.408	1.392	1.408	0.014

Table 4.2: Bond lengths and bond-length alternation (BLA) for the CBP molecule optimized by various quantum chemistry methods.

DFTB gives the lowest value of BLA while HF leads to the highest BLA. The values for BLA obtained by hybrid methods lie in between due to the varying moderate amount of exact exchange [45, 75]. This finding is in line with an earlier work on other conjugated molecules [45]. The method for optimization of the ground state structure has a notable impact on excitation energies, as can be seen in Fig. 4.3. The vertical excitation energies computed with various quantum chemistry methods for ground state geometries are provided in the Table 4.3.

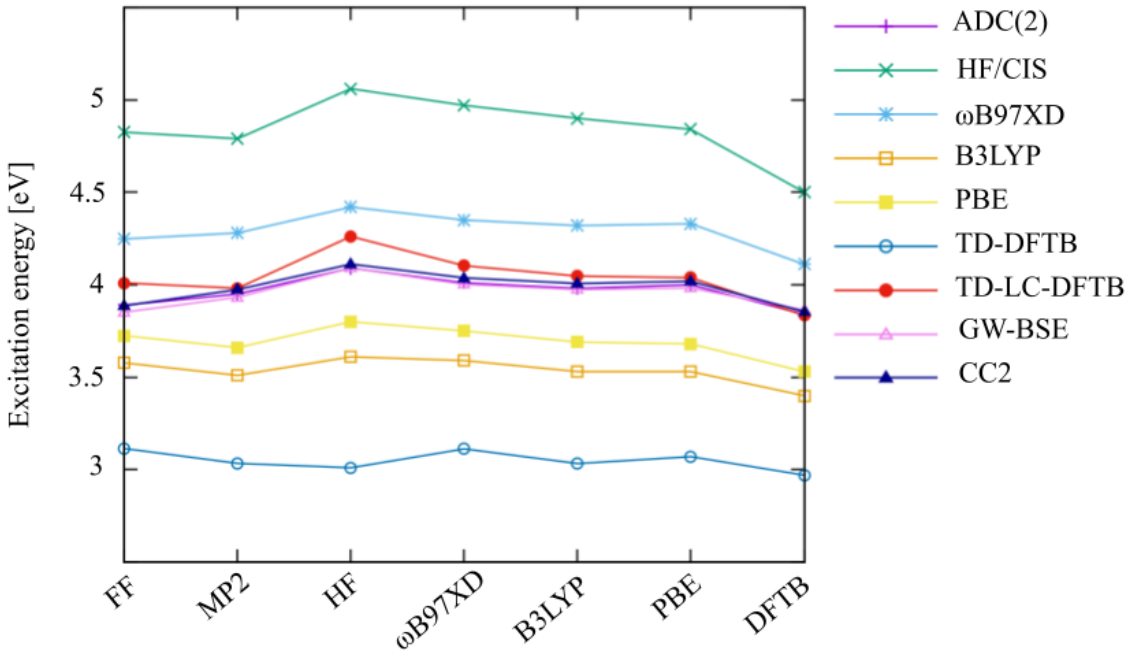

Figure 4.3: Influence of the applied methods on the computed vertical excitation energies. The x-axis shows the methods used to compute the ground state geometries; vertical excitation energies are then computed with various methods for these respective geometries. Note that, ADC(2) and GW-BSE are superimposed.

	FF	MP2	HF	ωB97XD	B3LYP	PBE	DFTB3
HF/CIS	4.82	4.79	5.06	4.97	4.90	4.84	4.50
ωB97XD	4.25	4.28	4.42	4.35	4.32	4.33	4.11
TD-LC-DFTB	4.01	3.98	4.26	4.10	4.05	4.04	3.83
CC2	3.89	3.97	4.11	4.04	4.01	4.02	3.85
ADC(2)	3.89	3.95	4.09	4.01	3.98	4.00	3.84
GW-BSE	3.85	3.93	4.09	4.00	3.97	3.98	3.86
PBE	3.72	3.66	3.80	3.75	3.69	3.68	3.53
B3LYP	3.58	3.51	3.61	3.59	3.53	3.53	3.40
TD-DFTB	3.11	3.03	3.01	3.11	3.03	3.07	2.97

Table 4.3: Vertical excitation energies (eV) of fully optimized geometries in vacuum using various quantum chemistry methods.

All methods show a slight variation with optimized structures, but differ significantly in absolute excitation energy values. As expected, HF/CIS overestimates the excitation energies for all optimized geometries, while the local and semi-local methods underestimate them due to the (semi-) local nature of the functionals. CC2, ADC(2) and GW-BSE are in excellent agreement with each other. The excitation energies computed by the range-separated ωB97XD method are slightly higher, as reported before, probably due to the amount of exact exchange used in this functional. LC-DFTB, similar to the LC-DFT methods, tends to overestimate excitation energies systematically, as has been shown for both ground state [76] as well as excited-state [77] optimized geometries, representing absorption and fluorescence energies. Different range-separated functionals have been shown to differ slightly in their predictions, and the excellent absolute agreement of LC-DFTB in this matter can be regarded as fortuitous. For the calculation of absorption spectra, this will simplify the comparison with experimental data. However, more important is the fact that the effect of structural changes on excitation energies is represented accurately, which will be investigated in the following.

As can be seen from Table 4.1, the different methods predict variations in both, BLA and dihedral angles. As it will be discussed later, the values of the dihedral angles in the bulk are determined by the intermolecular interactions. For the isolated molecule, the rotational barriers (6.5 kcal mol^{-1} and 3 kcal mol^{-1} for central and side angles, respectively, see Fig. 4.2) are low and can be overcome at room temperature; however, rotations may be constrained by the surrounding molecules in the bulk which stabilizes the rotamers. On the other hand, the BLA is found to impact excitation energies in conjugated molecules [45].

To estimate the effect of BLA on excitation energies, the CBP molecule in the gas phase is optimized with the side-, central-(α, β) and improper dihedral (γ) angles constrained to 45°, 60° and 0°, respectively. The optimizations are performed by ωB97XD/6-31+g*. As shown in Table 4.4, a clear pattern of increasing BLA with increasing amount of exact exchange is observed in the DFT methods, while the BLA tends to be more precisely predicted with MP2, since HF tends to overestimate this value [52].

	Bond length [Å]							BLA
	$C_1=C_2$	C_2-C_3	$C_3=C_4$	C_4-C_5	$C_5=C_6$	C_6-C_7	$C_7=C_8$	
FF	1.397	1.400	1.418	1.510	1.410	1.400	1.393	0.032
HF	1.376	1.383	1.391	1.490	1.391	1.383	1.386	0.030
ωB97XD	1.392	1.386	1.396	1.483	1.396	1.386	1.392	0.024
B3LYP	1.398	1.390	1.402	1.484	1.402	1.390	1.397	0.021
PBE	1.394	1.386	1.398	1.477	1.398	1.386	1.393	0.021
DFTB	1.406	1.392	1.407	1.487	1.407	1.393	1.406	0.018
MP2	1.403	1.395	1.407	1.476	1.407	1.395	1.403	0.017

Table 4.4: Bond lengths and bond-length alternation (BLA) for the constrained optimizations with the different methods. Bond length and BLA are given in Å.

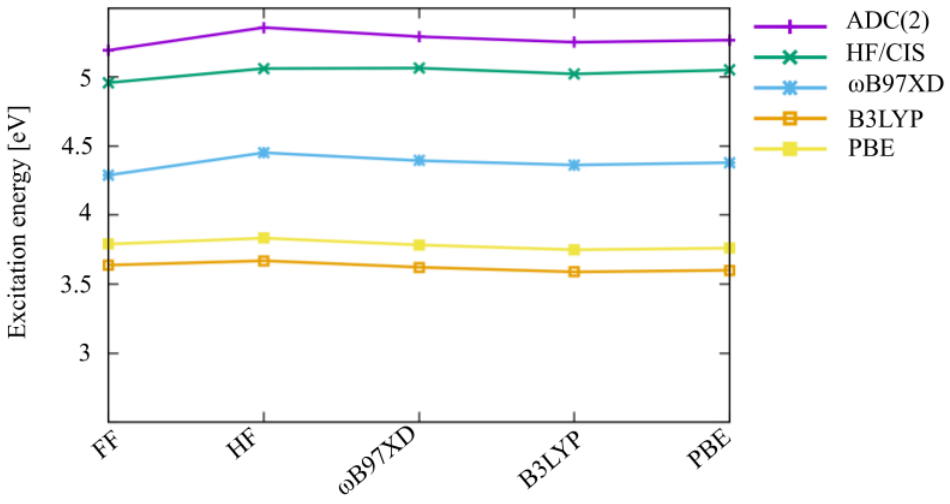

Figure 4.4: Excitation energies (eV) for different optimized geometries with constraint dihedral angles.

	FF	HF	ωB97XD	B3LYP	PBE
ADC(2)	5.195	5.360	5.294	5.254	5.269
HF/CIS	4.960	5.063	5.066	5.023	5.052
ωB97XD	4.290	4.453	4.395	4.363	4.380
B3LYP	3.638	3.669	3.622	3.588	3.601
PBE	3.790	3.833	3.784	3.749	3.761

Table 4.5: Vertical excitation energies (eV) of optimized CBP geometries in vacuum with constraint dihedral angles at 45°, 60° and 0° for α, β and γ.

The excitation energies follow the BLA trends, i.e. a blue shift with increasing BLA is observed, because the dihedral angles are the same for all methods and the vertical excitation energies only depend on the BLA. The vertical excitation energies can be found in the Fig. 4.4 and Table 4.5. A closer inspection of the bond lengths shows that the force field gives the least reliable estimates. In particular, the C–N bond-lengths deviate from the values computed by the other methods, which leads to a smaller excitation energy, as would be expected from the value of the BLA. Therefore, for the final estimation of absorption spectra, the QM/MM geometries using DFTB for the QM region are used. DFTB uses the PBE functional, and its geometrical prediction is therefore quite close to that of the other DFT methods, as discussed in detail in recent works [45, 78].

4.3.2 Absorption spectra in gas phase

Recently, a detailed study on CPB electronic structure has been published based on the GW-BSE method, which is taken as a reference here [52]. The lower panel of Fig. 4.5 shows a comparison of the gas-phase absorption spectra of CBP using TD-DFTB, TD-LC-DFTB and the GW-BSE reference (using the global minimum geometry taken from ref. [52]), respectively. As expected, TD-DFTB largely underestimates the excitation energies by about 1 eV, compared to GW-BSE, while TD-LC-DFTB reproduces the GW-BSE absorption spectrum well. The strong red-shift of TD-DFTB spectrum can be related to the well-known notorious self-interaction error of GGA functionals. It is not surprising that the introduction of long-range (LC) functionals in DFTB can reduce the errors of GGA, which leads to a good agreement between TD-LC-DFTB and GW-BSE spectra.

The upper panel of Fig. 4.5 shows the main orbital transitions in the gas-phase absorption spectrum of CBP. Some other electron transitions are shown in Fig. 4.6. The electron density of HOMO is delocalized over the whole molecule, while the lower occupied orbitals (HOMO-n, n = 2, 3, 5) exhibit a strong electron localization on the carbazole groups.

The electron density of LUMO is localized on biphenyl rings, while the electron density of higher unoccupied orbitals (LUMO–n, n = 1, 2, 6) is localized on two carbazole groups. The peak at 308 nm corre- sponds to the charge transfer (CT) from the carbazole groups to biphenyl rings, which may be sensitive to the rotation of the central dihedral angle. Two higher energy excitations (<250 nm) are related to the locally excited states in the carbazole groups. Therefore, the rotation of central and side dihedral angles may have little impact on high energy excitations, while it affects the lowest excitation energy significantly [52].

To estimate the effect of dihedral angles on excitation energies, we compute the 25 lowest vertical excitation energies and consequently the absorption spectra for different central and side angles, respectively. The dihedral angles are incremented in 10° from 0° to 90° using the ground-state optimized structure at the PBE0/def2-TZVP as the starting structure, taken from ref. [52]. For these structures, single-point energy calculations are carried out with TD-LC-DFTB and GW-BSE, respectively. Fig. 4.7(a) shows that for the central dihedral angles, the lowest-energy peak shifts from 3.91 eV to the higher energy at 4.15 eV and the intensity becomes lower with the increasing central angles, while the location and intensity of the high-energy peak at about 5.2 eV change slightly. Further information regarding the comparison between TD-LC-DFTB and GW-BSE excitation energies of the lowest-energy peaks, as well as the corresponding Kohn–Sham orbitals, is

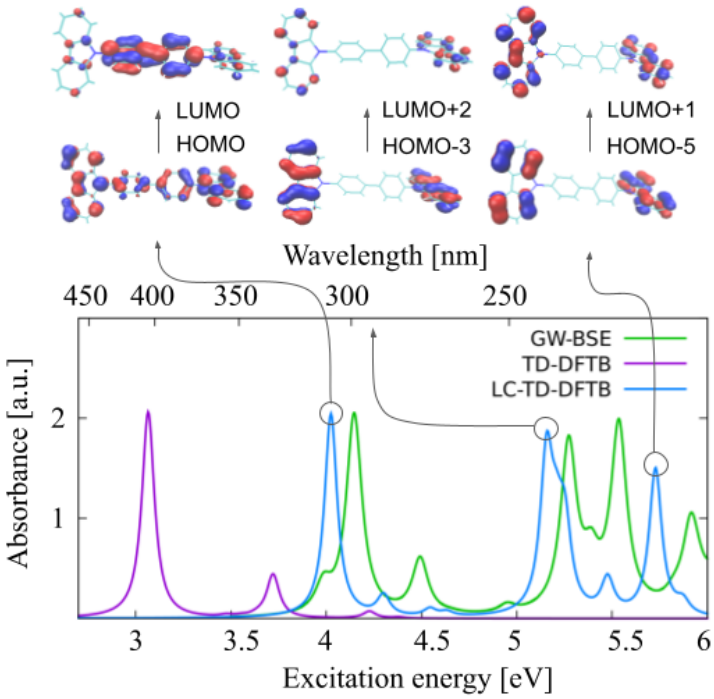

Figure 4.5: Absorption spectra of CBP in the gas phase and Kohn–Sham orbitals involved in the main orbital transitions of CBP. TD-DFTB, TD-LC-DFTB and GW-BSE calculations are shown in purple, blue and green lines, respectively. The excited states calculations are based on the global minimum geometry taken from ref. [52].

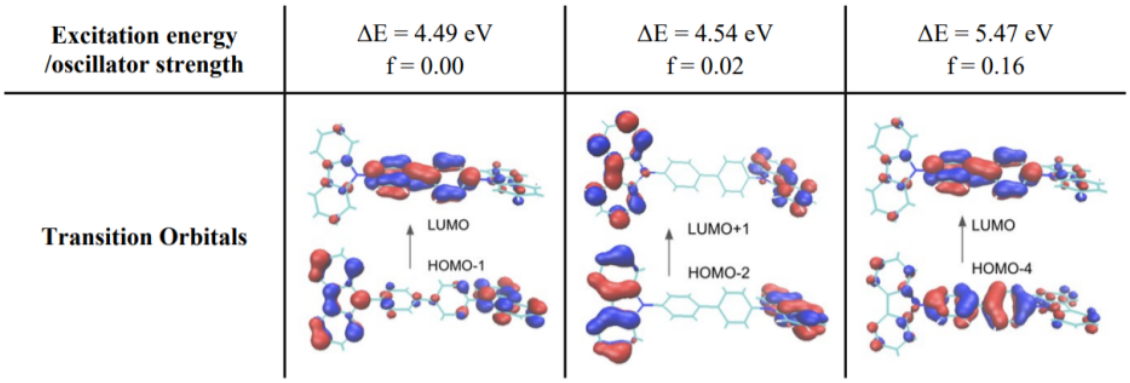

Figure 4.6: Electron transitions relevant to HOMO-n (n=1,2,4) obtained by LC-DFTB.

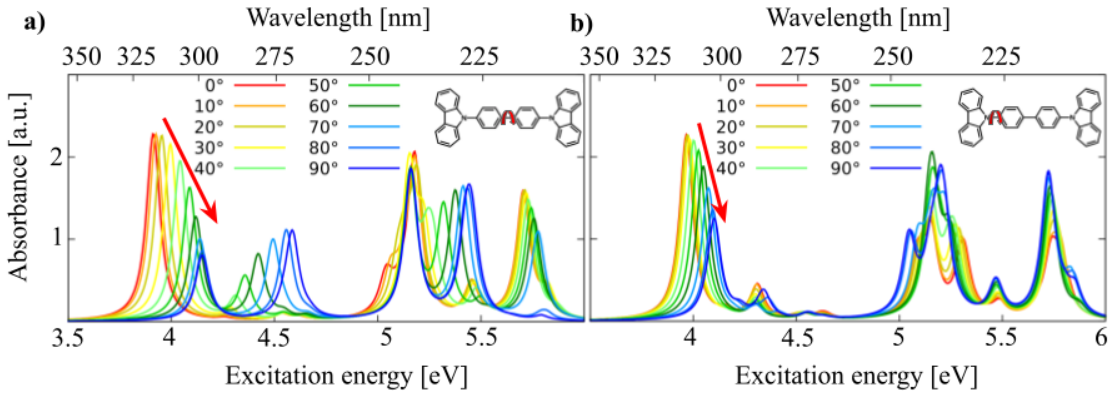

Figure 4.7: Absorption spectra computed by TD-LC-DFTB for different central (a) and side (b) dihedral angles.

	0 °	10 °	20 °	30 °	40 °	50 °	60 °	70 °	80 °	90 °
α	3.96 (3.86)	3.96 (3.87)	3.97 (3.90)	3.98 (3.94)	4.00 (3.97)	4.02 (3.98)	4.05 (3.99)	4.07 (4.00)	4.09 (4.02)	4.10 (4.01)
β	3.91 (3.92)	3.92 (3.96)	3.95 (3.98)	3.99 (3.98)	4.04 (3.99)	4.09 (3.99)	4.12 (3.97)	4.14 (3.98)	4.15 (3.98)	4.15 (3.98)

Table 4.6: Excitation energies (in eV) of the lowest-energy peak in the gas-phase static absorption spectra for side α and central α and β dihedral angles from 0° to 90° in 10 degrees obtained using TD-LC-DFTB and GW-BSE (shown in parentheses).

provided in the Table 4.6 and Fig. 4.8. It is noted that for the central angle from 0° to 90°, the lowest-peak exhibits the excitation transition from charge-transfer excitation to local excitation.

Furthermore, 4.7(b) shows a weak, blue-shifted absorption band at the lowest-energy peak in comparison to the central dihedral angle. To quantify the variation found for the different dihedral angles, the standard deviation of the lowest-energy peak has been calculated for central dihedral angle (4.04 ± 0.09 eV), which is about 2 times larger than that for side dihedral angle (4.02 ± 0.05 eV). This finding is consistent with the recent study on the excited-state properties of CBP that the rotational conformation has significant impacts on the low-energy absorption band, while it has minor effects on high-energy bands [52]. Therefore, the CT-type excitation is more sensitive to the central dihedral angle than the side dihedral angle.

4.3.3 Absorption spectra in condensed phase using force field geometries

The absorption in the bulk phase critically depends on the distribution of dihedral angles of the individual molecules, which results from the intermolecular interactions. Different values of the dihedral angles can be stabilized by steric interactions, leading to static disorder in the system. Furthermore, it is expected that dynamic disorder will lead to

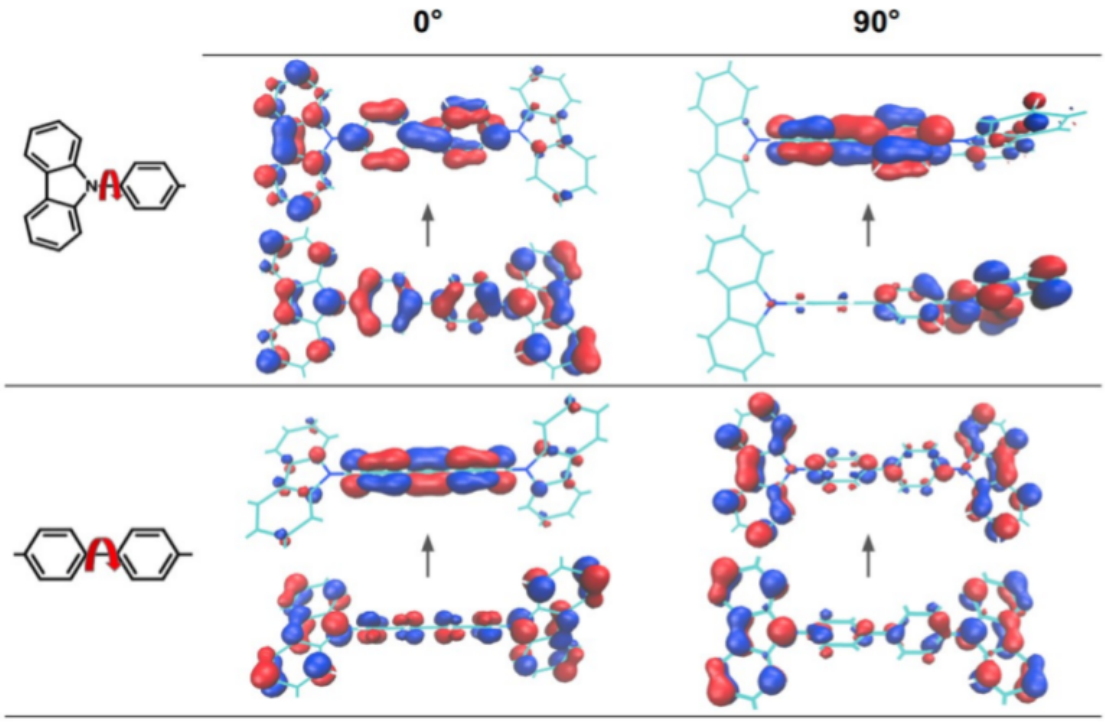

Figure 4.8: LCDFTB KohnSham orbitals involved in the excitation of the lowest-energy peak for side α and central β dihedral angles at 0°and 90°.

an additional broadening of the absorption spectrum. In principle, both effects could be included by computing excitation energies along the trajectories of all molecules in the simulation box. Since this is computationally demanding, a stepwise procedure is followed, as described below. In order to get a sufficiently large sample of molecules, force field trajectories are used, and absorption energies along each trajectory are computed with TD-LC-DFTB. Then, the trajectories using DFTB/MM are computed in order to obtain spectra based on more accurate geometries.

For one MD-snapshot containing all 5000 molecules in the supercell, the absorption energy of the bulk is then computed by successively evaluating the excitation energy of every molecule in the sample using TD-LC-DFTB, surrounded by the others using electrostatic embedding. The total spectrum is then the overlay of all 5000 single molecule spectra, as shown in Fig. 4.9(a). It is noted that the absorption spectrum is identical with the spectrum computed without considering the electrostatic interactions from surrounding molecules, which indicates that the electrostatic effects have a negligible influence on the absorption spectrum (see Fig. 4.10). As shown in Fig. 4.9(b), the static disorder is characterized by a significant spread in the distribution of the dihedral angles. The maxima of the α- and β-dihedral angles are around 60 and 40 degrees, respectively, consistent with the values of α and β for the structure optimized by ωB97XD method in the gas phase. As expected from Fig. 4.7, planarization of the molecule will lead to a red shift in the lowest absorption band, which is reflected in the absorption spectrum of the ensemble snapshot

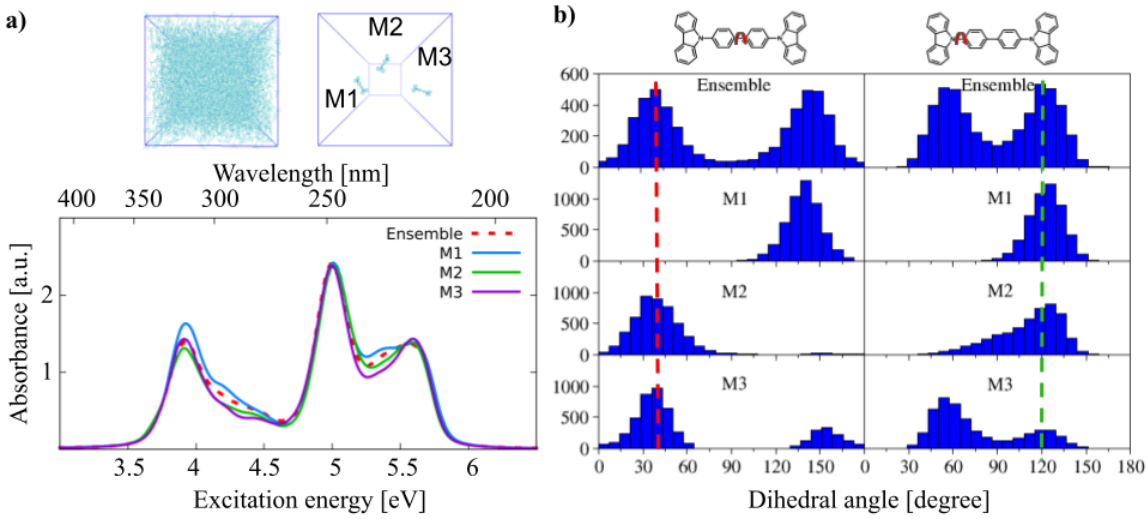

Figure 4.9: (a) Absorption spectra for the ensemble-snapshot of 5000 molecules (ensemble, displayed top at the left) and for the 5 ns trajectories of the three molecules picked from the ensemble. (b) Distribution of dihedral angles obtained for the ensemble and along the time-series of the three individual molecules. Note that the molecule is not symmetric and therefore a presentation 1–90° is not appropriate.

(red dashed line in Fig. 4.9(a)). It is red-shifted by 0.09 eV compared to the gas-phase spectrum of the optimized molecule in Fig. 4.5.

Fig. 4.10 shows the absorption spectrum of 1 MD-snapshot containing 5000 molecules with and without electrostatic interactions. The electrostatic interactions were represented by surrounding point charges. The absorption spectra are similar, indicating that the electrostatic interactions have minor effects on the absorption spectrum. This finding is not unexpected, since the environment is quite apolar. To understand this in detail, the references to other QM/MM calculations of embedded chromophores may be instructive. In a recent work [45], we computed the excitation energies of retinal and chlorophylls in their respective protein environments. The response to the environment is very different: While retinal excitation e nergies are highly tunable by the protein electrostatic environment, the excitation energies of chlorophylls are much less sensitive. This depends on (i) the electronic structure of the pigment and (ii) the polarity of the environment. Therefore, also in highly polar protein environments, the effects of color shifts can be very diverse. The protein environment in retinal proteins is specifically organized, in order to promote certain color shifts of the chromophore, which is particularly important for the process of vision: Here, different protein environments enable color shifts over 300 nm in order to absorb in the different wavelength regimes of visible light. In case of CBP, in contrast, this effect is very small, as expected, since the surrounding molecules are (i) quite apolar and (ii) randomly oriented. Please note, however, that our recent study showed [45], that some LC-DFT methods, including LC-DFT, slightly underestimate the effect of electrostatic tuning. This means, these methods should be applied to systems with care, where these

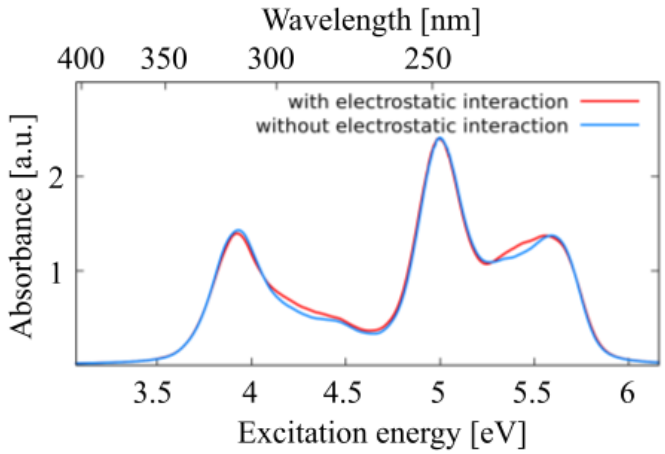

Figure 4.10: Comparison of absorption spectra for an ensemble-snapshot of 5000 molecules with and without considering electrostatic effect on excitation energy calculations. The electrostatic effects were considered by the point charge scheme.

effects are large, like retinal proteins. In systems, where this effect is small, this does not lead to a large error in the absorption spectra. In the case of chlorophylls in light-harvesting complexes, the main effects are exciton couplings, in the case of CBP, the main effects are structural changes, which are both covered quite well by LC-DFTB.

4.3.3.1 Absorption spectra along trajectories of individual molecules

To investigate the impact of dynamic disorder, three molecules (referred to as M1, M2 and M3) are selected at random positions of the supercell. Afterwards, absorption spectra are computed on a 5 ns classical MD trajectories and excitation energies are evaluated for snapshots every 1 ps, resulting in 5000 conformations in total. As shown in Fig. 4.9(a), the absorption spectra of M1, M2 and M3 are quite close to the absorption spectrum computed based on the ensemble sampling. Fig. 4.9(b) shows the comparison of the angle distributions of side and central dihedrals for M1 to M3 with the angle distributions of the ensemble. For the canonical ensemble, it is seen that the mean values of the central angle distribution are at 40° and 140°, and the mean values of the side angle distribution are at 60° and 120°. The angle distributions for M1 to M3 only exhibit one peak, showing that free rotation of the dihedral angles is impossible and the fluctuations are constrained to a limited range. It is interesting to see that individual monomers sample only a restricted part of phase space. The results on the ns time scale indicate that the computation of absorption spectra needs to be performed using longer-simulation-time trajectories until convergence. Therefore, using the same starting configurations, the classical MD trajectory is extended to 10 ns and excitation energies are evaluated for snapshots every 2 ps, leading to 5000 conformations in total. The convergence behavior is observed for M2 and M3 using the 10 ns-trajectory, whereas M1 is not converged and its respective angle distribution (mean value = 30°) is different from those obtained for M1 in the 5 ns trajectory (mean value = 40°) (see Fig. 4.11) which will lead to a stronger red shift and increased intensities

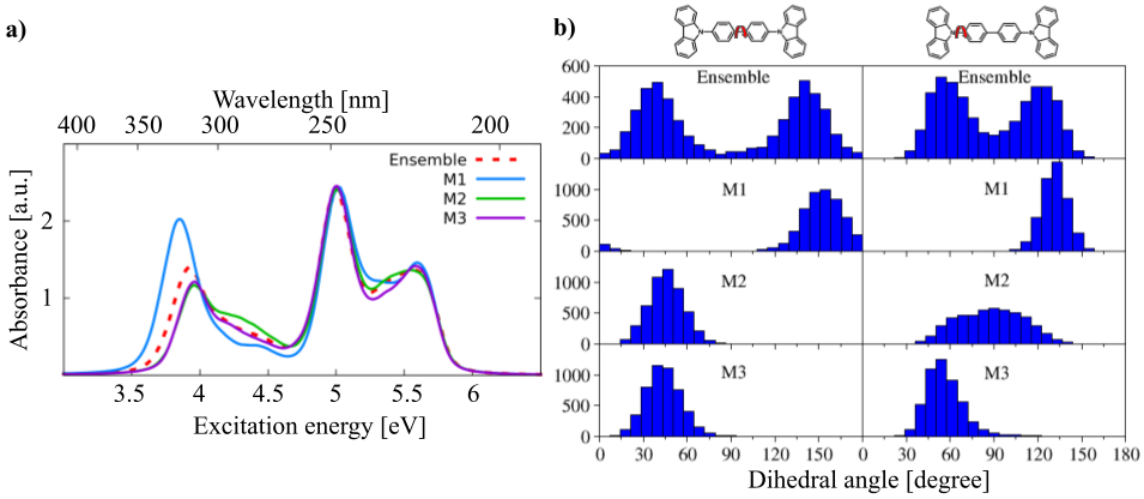

Figure 4.11: (a) Absorption spectra and (b) distribution of dihedral angles for the ensemble-snapshot of 5000 molecules and molecules M1, M2 and M3 obtained by a 10 ns trajectory.

of spectrum. In order to get further insight into the sampling methods, the absorption spectra as well as central angle distribution are examined for snapshots of molecule M1 at each nanosecond (Fig. 4.12). The importance of the central dihedral angle compared to the side dihedral angle on the CT-type excitation is demonstrated in Section 3.2. As shown in Fig. 4.12(b), the mean value of the central dihedral angle between 1–5 ns of the trajectory is around 35° whereas between 5–10 ns is around 20°.

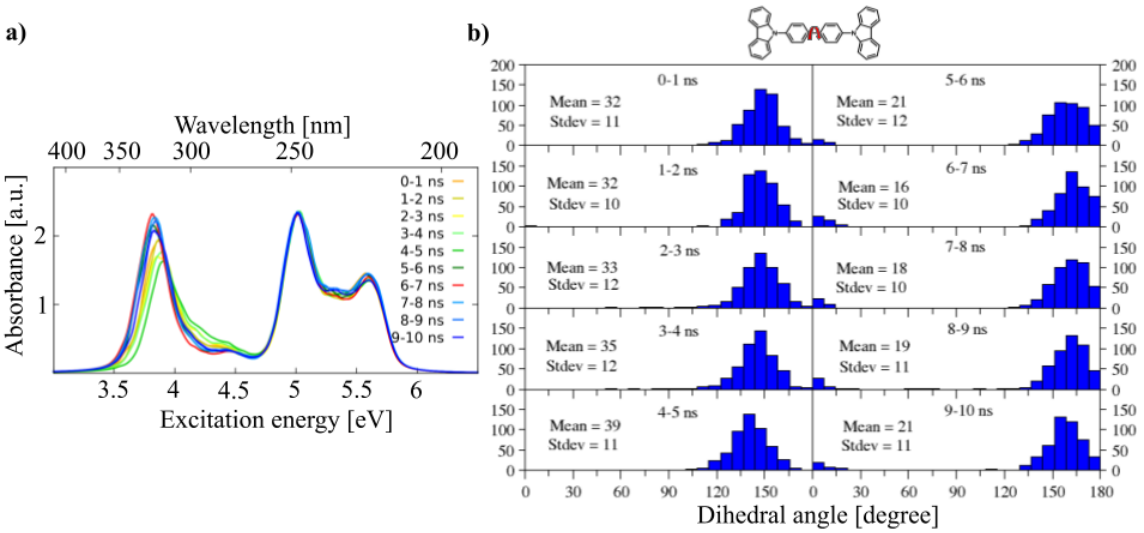

Figure 4.12: Absorption spectra (a) and central dihedral angle distributions (b) for each ns MD simulation in a 10 ns trajectory of molecule M1.

As shown in Fig. 4.5, the lowest absorbance peak is located at 4 eV for the optimized structure in the gas phase, while in the condensed phase it is red-shifted by about 0.3 eV (Fig. 4.9a). In principle, there are several factors determining the absorption maximum, which are (i) the dihedral angles, (ii) the electrostatic environment, (iii) and the exciton couplings. It is shown (see Fig. 4.10) that the electrostatic environment has a minor effect on the absorption spectrum. In the following, the effect of the other two factors will be assessed individually.

4.3.3.2 Comparison to gas-phase MD spectrum

To estimate the effect of the molecular interactions within the bulk, a MD simulation of CBP in the gas phase is performed, and the excitation energies along this trajectory are computed.

Fig. 4.13(a) shows a comparison of absorption spectra of CBP for 5000 conformations from gas-phase MD and 5000 structures from one condensed-phase MD-snapshot. The lowest-absorbance peak in the condensed-phase spectrum exhibits a red shift of 0.05 eV in comparison with the gas-phase MD spectrum. This is consistent with the central/side dihedral angle distribution shown in Fig. 4.7, i.e., more conformations with smaller angles occur in the condensed phase than in the gas phase. This indicates that intermolecular interactions in the bulk have a moderate influence on the absorption spectrum of CBP. The difference is not due to the electrostatic effect, but due to the accessible phase space.

In the gas-phase MD, the molecule can sample the full angular degrees of freedom, since rotational barriers can be overcome at room temperature. However, in condensed phase molecules may be more restrained, leading to a narrower angular distribution. Since in the bulk, the molecules sample more planar structures, a red-shift of the spectrum is observed (see Fig. 4.7).

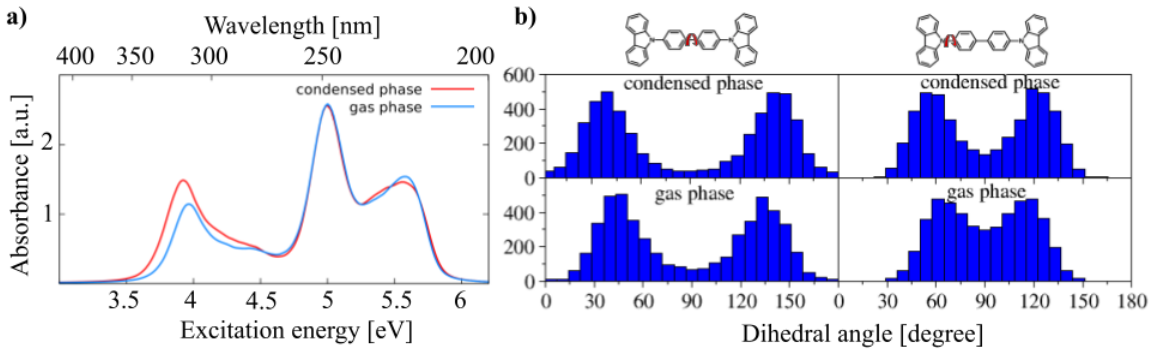

Figure 4.13: (a) Absorption spectra of CBP obtained using the conformations from gas-phase MD (blue line) and one condensed-phase MD-snapshot (red line) and (b) the corresponding central and side dihedral angle distributions.

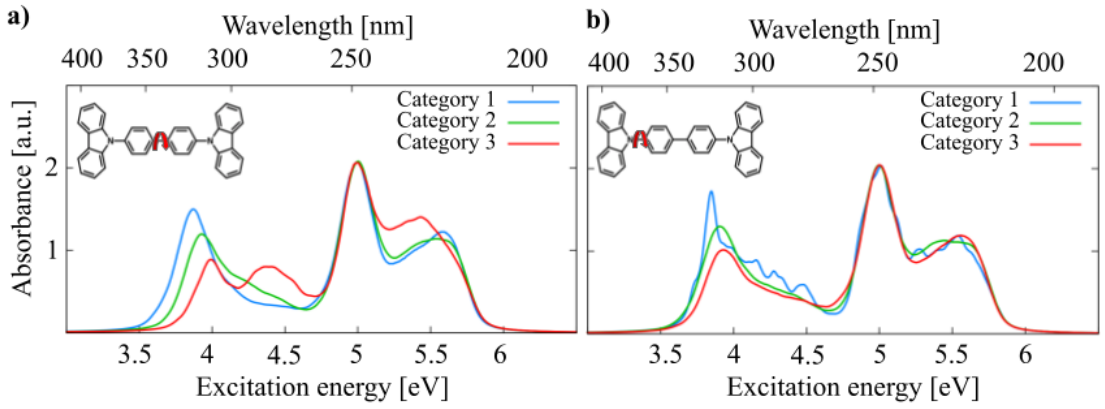

Figure 4.14: Partial absorption spectra of (a) central and (b) side dihedral angles are shown for three categories, 0°–30° and 150°–180° (blue), 30°–60° and 120°–150° (green) and 60°–90° and 90°–120° (red).

4.3.3.3 Effects of rotational conformation

The distribution of dihedral angles for the amorphous ensemble containing 5000 molecules (Fig. 4.9(b)) is split into 6 categories, where each category represents molecules with dihedral angles in increment of 30°. To obtain good statistics, the absorption spectra of each category from 0° to 90° and their complementary categories from 90 to 180 degrees are merged, e.g., structures with dihedral angles of 0°–30° and 150°–180° are pooled together.

Fig. 4.14 shows the partial absorption spectra of dihedral angles for all 3 pooled categories: Category 1: 0°–30° and 150°–180°, Category 2: 30°–60° and 120°–150° and Category 3: 60°–90° and 90°–120°. For the central dihedral angle at the peak with the lowest energy, as the angle gets closer to 0° (i.e., the planarity of biphenyl increases), the spectrum becomes more red-shifted and the intensity increases. Furthermore, it seems there are additional peaks around 4.4 and 5.4 eV for Category 3. For the side dihedral angle, it seems there is no dependency between intensity and dihedral angles. It is also noted that the curve for the side dihedral angle in Category 1 is not smooth due to the low sample size.

4.3.3.4 Absorption spectra for QM/MM sampling

As discussed above, the structures of a single molecule over a long simulation time are unable to represent all structures in the phase space. The snapshot of the ensemble, on the other hand, includes static disorder but misses the explicit treatment of dynamic disorder, which can be obtained by analysing MD trajectories. To investigate how many molecules are sufficient to represent the ensemble, 3 sets of molecules containing 10, 20 and 50 molecules are randomly selected from different locations of the supercell. A 5 ns long NPT MD simulation is performed. From this trajectory 500, 250 and 100 snapshots are taken for these 3 sets of molecules, respectively, to maintain the same number of structures in every test set. The convergence test with respect to the number of molecules (Fig. 4.15) shows that 50 molecules is sufficient to obtain converged angle distributions as well as a converged absorption spectrum.

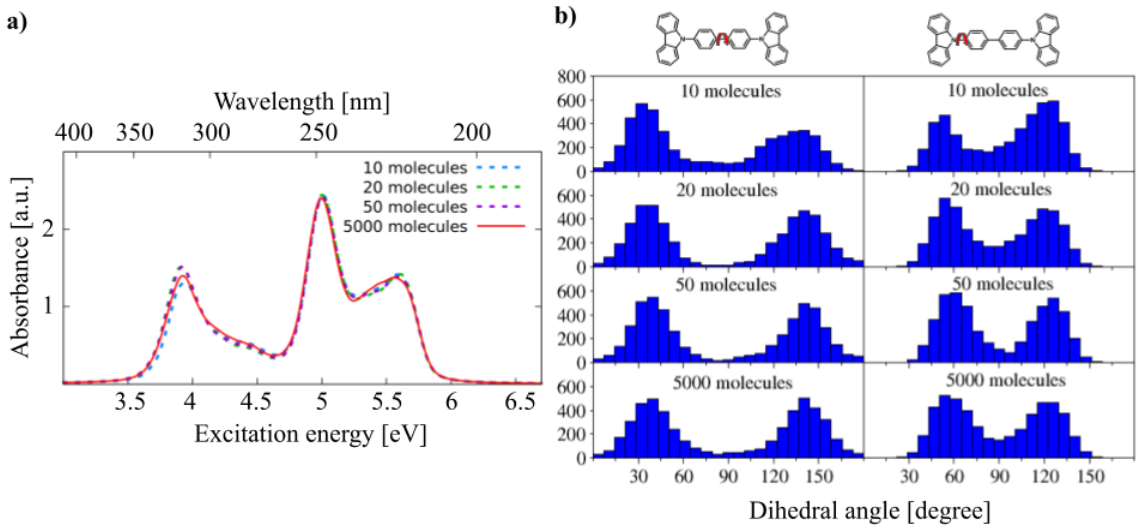

Figure 4.15: Convergence of the absorption spectra (a) and dihedral angles (b) with the number of individual molecules sampled in the supercell. From a 5 ns MD trajectory, three sets of molecules containing 10, 20 and 50 molecules are randomly selected and 500, 250 and 100 snapshots are taken for these three sets, respectively, to maintain the same number of structures in every test set.

As discussed in Section 3.1, DFTB gives a reasonably accurate estimation for the bond lengths in CBP molecules. Here, the QM/MM simulations are performed for amorphous CBP, where 50 molecules randomly distributed in the CBP supercell are treated by DFTB/3OB while the remaining molecules of the system are treated by the modified force field. Fig. 4.16(a) shows the comparison of the experimental absorption spectrum of CBP [72] with the absorption spectrum using the structures from QM/MM simulations and 5000 conformations from one MD-snapshot, respectively. The QM/MM simulation reproduces the peaks of the experimental absorption spectrum of CBP quite well. The experimental spectrum is much broader than the computed spectrum., which may be due to the defect absorption in the CBP film. A key ingredient of this good agreement for the absorption peaks is the (fortuitous) accuracy of LC-DFTB for the CBP excited states, as discussed above, which allows us to compute absolute excitation energies in this case. In particular, the BLA is sufficiently well represented by the ground state DFTB/MM calculations. In comparison to the spectrum based on the FF geometries, the lowest-energy peak of the QM/MM absorption spectrum exhibits a red shift of 0.2 eV. The red-shift of excitation energy can be attributed to the smaller BLA using GGA-type DFT method [79], in comparison to the BLA obtained by the parameterized force field (see Table 4.4). In addition, there is a slight deviation in the description of the angular distribution. Fig. 4.16(b) shows the angle distributions of CBP monomers obtained by MD and QM/ MM simulations, respectively. MD simulation with modified force field generates fewer molecules with angles smaller than 30° (larger than 150°) than DFTB/MM simulation, which indicates a more planarity of CBP conformations obtained by DFTB than force field.

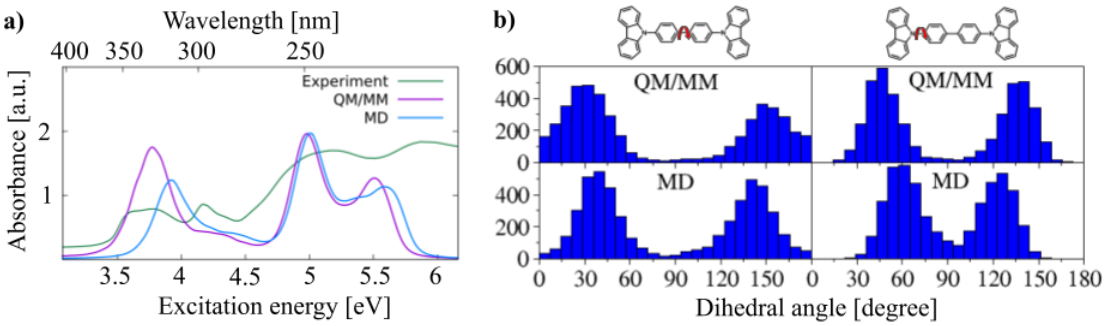

Figure 4.16: (a) A comparison of the experimental absorption spectrum of CBP taken from ref. 45 with the absorption spectra obtained using the structures from QM/MM simulations and one condensed-phase MD-snapshot. (b) Central and side dihedral angle distributions obtained by QM/MM (upper panel) and MD (lower panel) simulations.

4.3.3.5 Effects of aggregation

It is well known that the aggregation of chromophores has a significant influence on the absorption spectrum [80, 81, 82, 83]. Delocalization of excited states over two or more molecules could lead to a further red-shift of adsorption spectrum. To examine the aggregation effect on the absorption spectrum of CBP, we compute the nearest-neighbor excitonic coupling, which is an important quantity to describe the extent of molecular aggregation. For all 5000 nearest neighbours, those dimers which are doubly counted (28 dimers), are removed.

As shown in Fig. 4.17(a), the excitonic couplings exhibit a broad distribution with the average value of 30 meV, which indicates a weak aggregation effect in amorphous CBP. Moreover, all 4972 dimers are split into three categories with the excitonic couplings J<30, 30<J<60 and J>60 meV, where each contains 4226, 682 and 64 dimers, respectively. Afterwards, 25 excitation energies for each CBP monomer and 70 excitation energies for each CBP dimer are computed, in each respective category.

The absorption spectra are shown in Fig. 4.17(b). The low energy part of the monomer absorption spectra is very close to that of the dimer absorption spectra, for all coupling strengths, i.e., there is no indication for a substantial delocalization of excited states. The small couplings of J<100 meV is in the same range with the dynamical disorder, i.e., the dynamical disorder enforces localization. This is indicated by the fact that the excitation energies computed for monomers and dimers in every class are very similar. If a coupling of the low energy states occurred, an additional red-shift would be expected. Nevertheless, it is very interesting to see that a red-shift occurs which correlates with the coupling strength, although this cannot be induced by electronic delocalization. The results can be interpreted as follows: High excitonic couplings may indicate that dimers are stacked very well. This stacking induces conformations more shifted towards planar conformations, as shown in Fig. 4.17(c), and more planar conformations lead to a red-shift in the absorption spectrum.

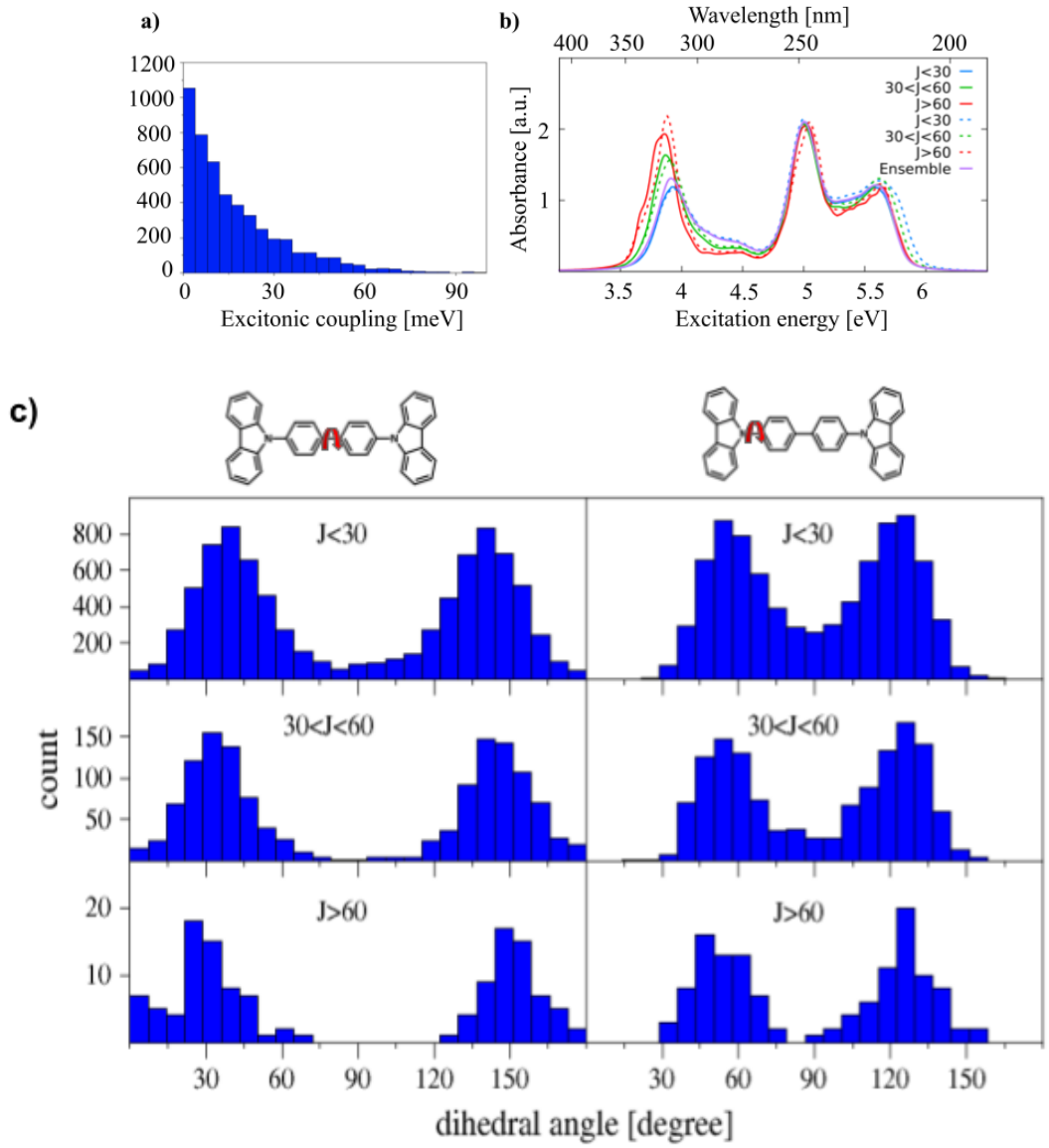

Figure 4.17: (a) Nearest-neighbor excitonic coupling distributions. (b) Excitonic coupling dependent absorption spectra of monomers (solid lines) and dimers (dashed lines). (c) Central and side dihedral angle distributions.

4.4 Conclusions

The absorption spectrum of CBP molecules is significantly altered in the amorphous phase due to interactions among the monomers. While electrostatic interactions as well as excitonic couplings turn out to be of minor importance, structural effects, in particular torsion around the main dihedral angles play a major role. Steric interactions induce a planarization of the molecules in the ensemble, which leads to an absorption red-shift of about 0.3 eV w.r.t. a gas phase absorption spectrum.

Conformational sampling is a key to capture the static and dynamic disorder in the system. Due to the packing in the amorphous phase, the individual monomers show only restricted motions, however, relevant conformational changes appear also on the nanosecond timescale, which requires efficient sampling techniques.

Standard force field parameters have to be taken with some care; we found that a major reparametrization of dihedral potentials is required for a realistic model of the amorphous structure. If these important degrees of freedom are modelled too soft or too stiff, the molecular ensembles may be largely misrepresented, since certain parts of the conformational space may be under- or oversampled. This, however, would show up in the absorption spectrum, since excitation energies are very sensitive to these degrees of freedom.

Our simulations could successfully reproduce the experimental absorption spectrum which may indicate that our structural model is quite accurate. We can deduce this from the computed spectrum, since the applied LC-DFTB method very accurately reproduces the excitation energies of high-level quantum chemical methods as GW-BSE, CC2 or ADC(2). Further, the ground state structures have been sampled with DFTB, which shows a very good agreement for the molecular structures, particularly, for the BLA.

The structural model derived here will be used in future work to investigate charge and exciton transfer processes in CBP, which will allow study of the processes behind the degradation of this material.

5 Effects of dynamic disorder on eletron transfer for OSCs

5.1 Introduction

Electron transfer (ET), or the act of moving an electron from one center (donor) to another one (acceptor), plays a crucial role in chemistry and electronics. To understand the electronics functionality, it is essential to investigate the mechanism of ET. The following scheme shows a typical electron transfer process.

$$D + A \xrightarrow{ET} D^{+} + A^{-} \tag{5.1}$$

In the ET reaction, to form the resonant state, donor (D) and acceptor (A) require the reorganization energy (λ) which is defined as the energy required to reorganize the structure from initial to final coordinates, without making the charge transfer. This energy arises from structural differences between the equilibrium configurations of the reactant and product states. At resonance or transition states of electron transfer reaction, the electron propagates from D to A (Fig. 5.1) [84, 85].

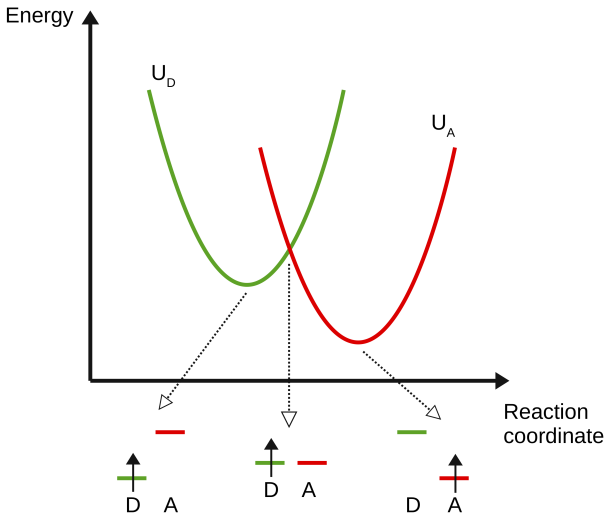

Figure 5.1: Donor and acceptor potential surfaces. ET takes place when D and A are at resonance conformation.

The nuclear motion not only brings D and A into electronic resonance using reorganization, but also causes donor-acceptor (DA) electronic interactions to fluctuate. Most molecular structures are dynamic and have a wide range of local and global conformations

at room temperature. Since DA electronic interactions are sensitive to conformational changes, it is expected that the structural fluctuations have a large influence on room temperature DA electronic couplings. When the structural fluctuations influence the DA electronic coupling and occur on faster time scales, the failure of Franck–Condon approximations is not surprising. Therefore, to assess the impact of the aforementioned parts on the observed rate, it is not adequate to only compute T_{DA} using a static method because it is also the time scale of coupling fluctuations which determines the observed rate. There are several important questions associated with structural fluctuations, averaging and ET rates:

- Is the fluctuation of the coupling (dynamic disorder) important in ET?
- How do fluctuation of the coupling affect the ET rate?
- Which molecular modes dominate the dynamics disorder?

Early theoretical analysis indicates that variation in the electronic coupling caused by nuclear motion can affect ET rates due to failure of the Born-Oppenheimer [86] and Franck-Condon [87, 88] approximations. These nuclear motions can cause the fluctuations in T_{DA}, influencing on tunneling pathways [89, 90, 91, 92, 93, 94]. More recently, other studies investigate the ET kinetics in systems with fluctuating donor–acceptor T_{DA} [95, 96]. To our knowledge, recent theoretical studies explore the dynamical effects on nonadiabatic ET reactions only for biological system. In this thesis, we extend the previous theoretical studies in several important organic semiconductors (OSCs). Dynamical issues in nonadiabatic ET in semiconductor materials are the focus of this work.

In organic solids, where molecules are weakly bounded by van der Waals interactions, the electronic coupling between D and A is weak. Thus, the ET rate can be expressed within the framework of perturbation theory in terms of Fermi's golden rule [97]. This approach provides the basis for the study of nonadiabatic ET reaction; the product of the square of T_{DA}, as expected from perturbation theory and the probability of the D and A forming a resonant state [98, 99, 100].

$$k_{ET} = \frac{2\pi}{\hbar}|T_{DA}|^2\rho_{FC} \tag{5.2}$$

where T_{DA} is the donor-acceptor (DA) electronic coupling interaction and ρ_{FC} is the thermally weighted Franck–Condon density between initial and final vibronic levels.

k_{ET} in Eq. 5.3 is the Fourier transform of the Franck-Condon correlation function $C_{FC}(t)$ and the electronic coupling correlation function $C_{T_{DA}}(t)$ product. A big advantage of the time-dependent view is that it is very well suited for the description of decay processes [101, 102]. Thus, the decay times of $C_{FC}(t)$ and $C_{T_{DA}}(t)$ can be associated with structural fluctuations, by using molecular dynamics (MD) simulations. By derivation of the semi-classical rate from the quantum formulation, the nonadiabatic ET rate is: [103]

$$k_{ET} = \frac{1}{\hbar^2}\int_{-\infty}^{+\infty} \mathrm{d}t\ e^{i[U_D^{min}-U_A^{min}]t/\hbar}\ C_{T_{DA}}(t)\ C_{FC}(t) \tag{5.3}$$

where $C_{T_{DA}}(t)$, the correlation function of DA coupling and $C_{FC}(t)$, the time-dependent Franck-Condon factor, are given by:

$$C_{T_{DA}}(t) = \langle \hat{T}_{DA}(t)\hat{T}_{DA}(0)\rangle = \sum_{i_D} P_{i_A}\langle i_A|\ e^{i\hat{H}_A^{vi}t/h}\ \hat{T}_{DA}(0)\ e^{-i\hat{H}_A^{vi}t/h}\ \hat{T}_{DA}(t)|i_A\rangle \tag{5.4}$$

$$C_{FC}(t) = \langle\ e^{i\hat{H}_D^{vi}t/\hbar}\ e^{-i\hat{H}_A^{vi}t/\hbar}\ \rangle_D = \sum_{i_D} P_{i_D}\langle i_D|\ e^{i\hat{H}_D^{vi}t/\hbar}\ e^{-i\hat{H}_A^{vi}t/\hbar}\ |i_D\rangle. \tag{5.5}$$

$\hat{H}_D$=$U_D^{min}|D\rangle\langle D|$+ $\hat{H}_D^{vi}$ and $\hat{H}_A$=$U_A^{min}|A\rangle\langle A|$+ $\hat{H}_A^{vi}$, where $\hat{H}_D^{vi}$ and $\hat{H}_D^{vi}$ are the vibrational Hamiltonian for the donor and acceptor energy surfaces. $C_{FC}(t)$ is the classical thermal average of initial nuclear wave function propagated with the electron in the D state and the same wave function propagated with the electron in the A state (Fig. 2) [104, 105], i.e.,

$$C_{FC}(t) = \langle\langle \psi^D(t)\,|\,\psi^A(t)\rangle\rangle. \tag{5.6}$$

The time it takes for two nuclear wave functions to lose overlap when they are at crossing region due to DA thermal fluctuations is often called the Franck-Condon time $\tau_{FC} \approx \hbar/\sigma_{\Delta U} = \hbar/\sqrt{\lambda K_B T}$ where $\sigma_{\Delta U} = \hbar/\sqrt{\lambda K_B T}$ is the rms fluctuation in $\Delta U = U_A - U_D$. [96]. τ_{FC} is $\hbar$ over the energy gap fluctuations, which provides the duration of time the gap is in resonance.

In the classical limit, the electronic coupling (T_{DA}) depends on the nuclear trajectories, and the correlation function is approximated by:

$$C_{T_{DA}}(t) = \langle T_{DA}(t)\, T_{DA}(0)\rangle \tag{5.7}$$

where $T_{DA}(t)$ is computed for successive nuclear conformations along classical trajectories, and $\langle\ldots\rangle$ denote the classical thermal average. The decay time for $C_{T_{DA}}$ (Eq. 5.7) is the coherence time τ_{coh}, which contains information about how fast coherence is lost due to the coupling fluctuation.

Figure 5.2 illustrates small versus large times limits. For small times compared with τ_{coh}, we obtain the maximum amplitude of $C_{T_{DA}}(t)$, the mean square value of coupling ($\langle T_{DA}^2\rangle$) which is independent of time, and for large times compared with τ_{coh}, $C_{T_{DA}}(t)$ approaches $\langle T_{DA}\rangle^2$.

$$C_{T_{DA}} \approx \sigma_{T_{DA}}^2\, e^{-t/\tau_{coh}} + \langle T_{DA}\rangle^2 \tag{5.8}$$

To describe the effects of dynamical disorder on the electronic coupling (the magnitude of T_{DA} fluctuations), Balabin and Onuchic [90] introduced the coherence parameter, which is characterized by

$$R_{coh} = \frac{\langle T_{DA}\rangle^2}{\langle T_{DA}^2\rangle} = \frac{\langle T_{DA}\rangle^2}{\langle T_{DA}\rangle^2 + \sigma_{T_{DA}}^2} = \frac{1}{1 + \frac{\sigma_{T_{DA}}^2}{\langle T_{DA}\rangle^2}} \tag{5.9}$$

According to Eq. 5.9, the coherence parameter falls in the range between zero and one. In the limit where coupling fluctuations ($\sigma_{T_{DA}}^2$) are large in comparison with the average

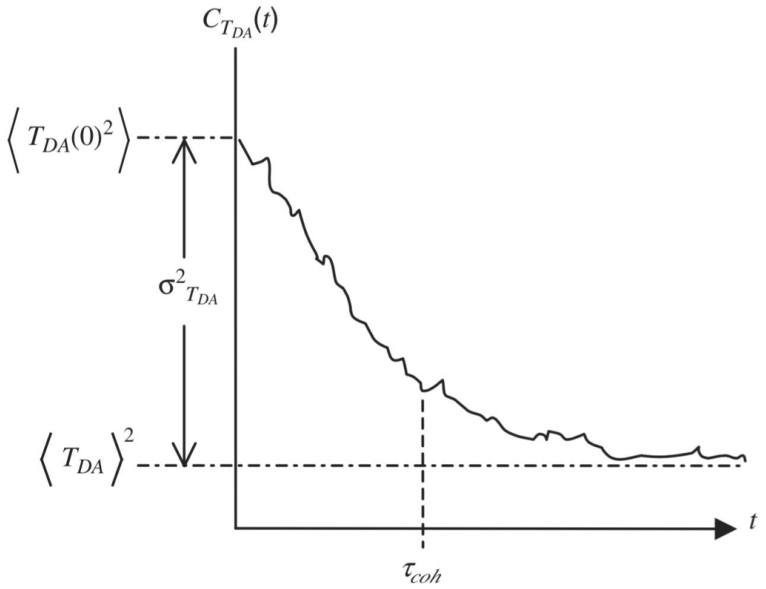

Figure 5.2: Decay time (τ_{coh}) of $C_{T_{DA}}(t)$ (Reprinted from [24]).

coupling $\langle T_{DA} \rangle$, R_{coh} is small ($R_{coh} \ll 1$), whereas when the coupling fluctuations are small compared with the average, R_{coh} approaches 1.

Qualitative consideration of coupling fluctuations

In nonadiabatic rate constant expression, the Franck–Condon approximation may become invalid in systems with fluctuating T_{DA} [106]. There have been several studies [94, 96, 107] characterizing nonadiabatic *ET* reactions in terms of distinct rate regimes (Fig. 5.3).

Regime I: $\tau_{coh} > \tau_{FC}$ (slow coupling fluctuation)

In this regime, the coupling does not have time to fluctuate while the D and A are in resonance. Thus, D and A see a static coupling at the time of the crossing (i.e., the Franck-Condon approximation is valid). Therefore, the ET rate is given by the Marcus–like rate constant ($k_{ET} \propto \rho_{FC}$), where one finds two limits (assuming timescales are longer than the ET time ($\tau_{coh} \gg 1/k_{ET}$), [108]):

a) $R_{coh} \approx 1$ (weak coupling fluctuations): In this situation, thermal fluctuations of the structure do not change T_{DA} significantly. Then $\langle T_{DA}^2 \rangle \approx \langle T_{DA} \rangle^2$ and the rate becomes:

$$k_{ET} \propto \langle T_{DA} \rangle^2 \rho_{FC}. \tag{5.10}$$

b) $R_{coh} \ll 1$ (strong coupling fluctuations): In the opposite limit, it is expected that nuclear dynamics will greatly affect T_{DA}. Therefore, $C_{T_{DA}}$ in Eq. 5.3 should be replaced by $\langle T_{DA}^2 \rangle$. Equation 5.11 captures the effect of structural averaging of various conformations.

$$k_{ET} \propto \langle T_{DA}^2 \rangle \rho_{FC}. \tag{5.11}$$

Regime II: $\tau_{coh} < \tau_{FC}$ (fast coupling fluctuation)

Here, the coupling has time to fluctuate while the D and A states are resonant. Therefore, the Franck–Condon approximation is not valid in this regime as the coupling can not be assumed to be independent of nuclear dynamics. Thus, the rate is more complex than it is suggested by Eq. 5.3 because the decay times of $C_{FC}(t)$ and $C_{T_{DA}}(t)$ are similar [23, 109, 110]. Recently, there have been several studies to demonstrate the existence of different kinetic regimes [23, 111, 112].

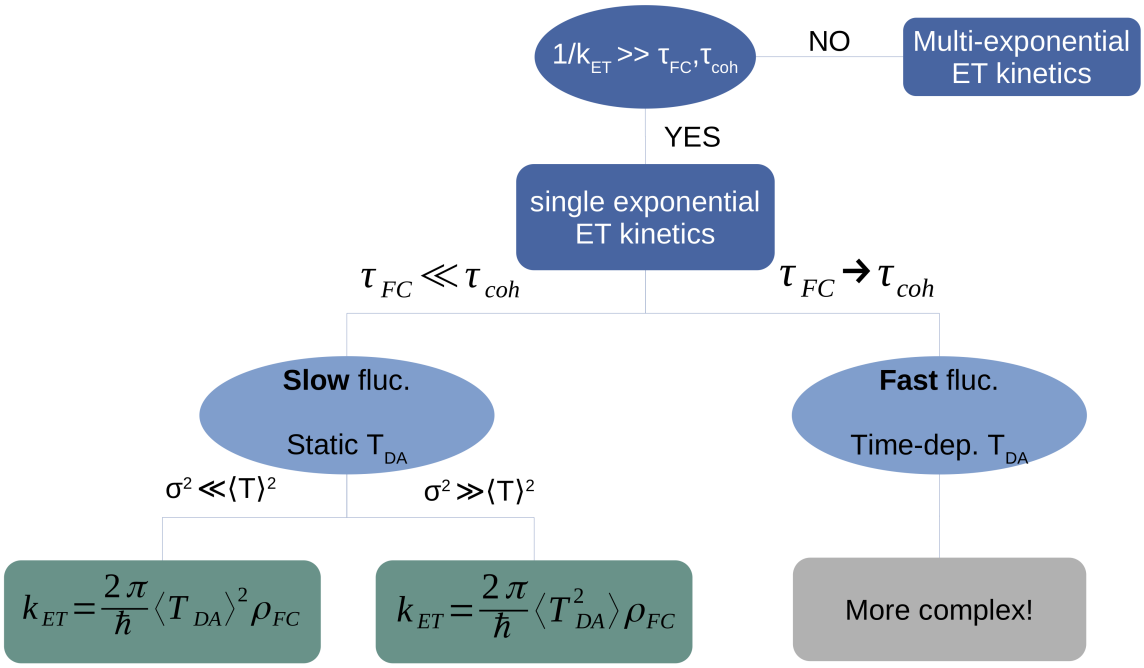

Figure 5.3: Workflow of nonadiabatic ET rate regimes.

In this work, we aim to study the aforementioned regimes that are valid for OSCs. In addition we discuss how structure and importantly structural fluctuations influence ET reaction rates.

5.2 Computational Details

Classical molecular dynamics (MD) simulations are performed to generate thermal fluctuation of molecular structures, and then electronic coupling between donor (D) and acceptor (A) is calculated by quantum chemical calculations for each snapshot of the MD simulations.

Amorphous morphology of 1000 molecules is constructed by simulating physical vapor deposition, based on a Monte-Carlo (MC) protocol. The GROMACS 5.0.4 package [113, 114] was used to set up the system and to perform classical MD simulations. The force field parameters are obtained from the general AMBER force field (GAFF), which has been showed to proivde good results and should describe correctly the conjugated molecules governed by $\pi - \pi$ stacking [59, 60]. The atomic charges are generated by the restrained electrostatic potential fitting procedure (RESP) [61, 62] calculated at the HF/6-31g* [63,

64] level using the Gaussian09 software [115]. The energy of the system is minimized using steepest descent (SD), and from this geometry, a 2 ns equilibration process leads to the starting trajectory points. The *Nosé–Hoover* thermostat [66] and *Parrinello–Rahman* barostat [70] are employed to equilibrate temperature and pressure at 300 K and 1 bar, respectively.

To compute charge transfer (CT) parameters (ϵ_i and T_{DA}), we pick up five random molecules (D_i , $i = 1, ..., 5$) with different environments and find their 10 nearest neighbours (A_{ij} , $j = 1, ..., 10$). Afterwards, we perform a combined quantum mechanics/molecular mechanics (QM/MM) approach using GROMACS [116], which has become a standard approach for these analyses [117] to generate trajectories. These trajectories with the time step of 1 fs for 10 ps are used to evaluate both CT parameters, i.e., we obtain 10,000 data points for all quantities of interest to analyze. It is worth noting that the short-time trajectories provide clearer picture of T_{DA} fluctuations since the decay of Franck–Condon time is very rapid. Since our simulations require several millions of quantum chemical calculations, ab initio or DFT-type methods are not reasonable. For this purpose, we use the nonself-consistent (non-SCC) variant of density functional tight-binding method (DFTB) because it provides the best compromise between accuracy and speed. Since T_{DA} enters with the square in the ET rate constant 5.2, the accuracy of k_{ET} strongly depends on the value of the electronic coupling. The accuracy of the electronic couplings computed by DFTB are demonstrated in [118, 119]. DFTB electronic couplings are scaled by a factor of 1.54 for hole transport to reach the accuracy of the second-order couple cluster (CC2) calculations [120]. The tight binding Hamiltonian, containing the CT parameters, is computed for 10,000 conformations sampled at every 1 fs in the QM/MM simulations.

5.3 Results and Discussion

In the current study, to identify nonadiabatic *ET* rate regimes and compute $\langle T_{DA} \rangle$ and/or $\langle T_{DA}^2 \rangle$, we apply the presented workflow (Fig. 5.3) for four organic semiconductors (OSCs) shown in Figure 5.4, namely the hole-transport materials 4,4'-bis(carbazol-9-yl)-2,2-biphenyl (CBP), N,N'-di(biphenyl-4-yl)-N,N'-diphenyl-[1,1'-biphenyl]-4,4'-diamine (p-BPD), 4,4',4"-tris(N-carbazolyl) triphenylamine (TCTA), and 5,10,15-triphenyl-5H-diindolo [3,2-a:3',2'-c] carbazole (TPDI).

In the following, we compute CT parameters for the above OSCs and afterwards τ_{FC}, τ_{coh} and R_{coh} via Eqs (5.6), (5.8) and (5.9) to distinguish between ET rate regimes. In addition, we analyze the impact of structural fluctuations on ϵ_i (ionization potential (IP)) and T_{DA}. Moreover, we discuss the critical timescales which play an important role in ET reactions with fluctuating behaviour. Among aforementioned OSCs, TCTA is used as a typical example since other materials have the similar pattern.

5.3.1 Site energy (ϵ_i)

As discussed above, we calculate the room-temperature Franck-Condon time (given by $\tau_{FC} \approx \hbar/\sigma_{\Delta U} = \hbar/\sqrt{\lambda K_B T}$) of 4 amorphous OSCs shown in Fig. 5.4.

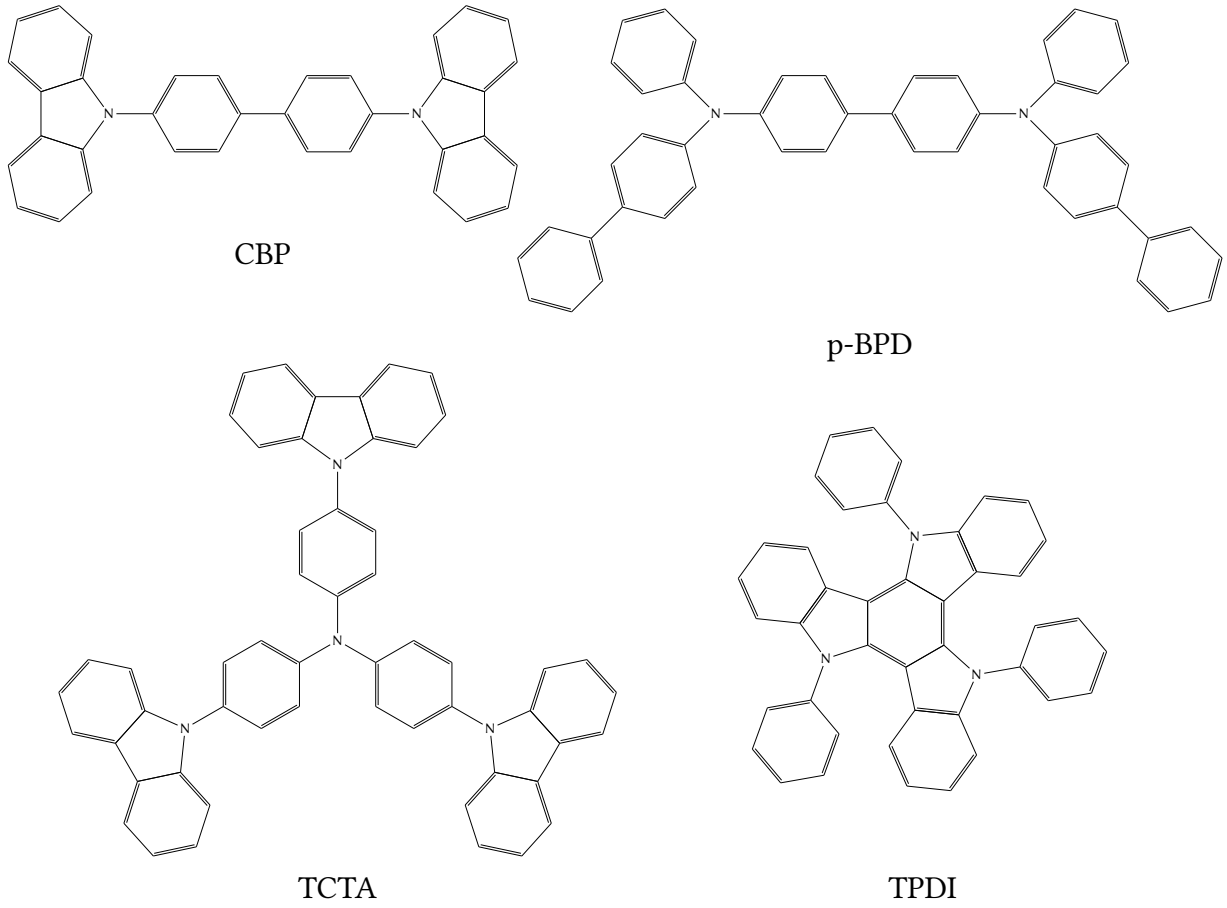

Figure 5.4: Schematic structures of the hole-transport materials characterized in this work.

$$\begin{aligned} \tau_{FC\,CBP}(\lambda = 0.134\ eV) &= 8.06\,\text{fs}, \\ \tau_{FC\,TPDI}(\lambda = 0.145\ eV) &= 7.63\,\text{fs}, \\ \tau_{FC\,p-BPD}(\lambda = 0.173\ eV) &= 6.98\,\text{fs}, \\ \tau_{FC\,TCTA}(\lambda = 0.206\ eV) &= 6.40\,\text{fs}. \end{aligned} \tag{5.12}$$

The room-temperature τ_{FC} are very short and this is due to small relaxation energy ($\lambda \approx 0.1$ eV). As can be seen in Eq. (5.12), τ_{FC} are quite close due to similar λ values. The calculations above assume that site energy fluctuations are uncorrelated Gaussians. It has been shown that structural fluctuations produce distributions of HOMO/LUMO energies which are approximately Gaussian distributed ([121]).

Fig. 5.5a and 5.5b show the time series and distributions of site energy of 5 individual molecules (D1-D5) of TCTA along a 10 ps QM/MM trajectories. It should be noted that a similar pattern arises for the other OSCs studied, which are shown in *Appendix*. As can be seen, site energies of TCTA are not static quantities and fluctuate significantly when evaluated along the trajectory. Here, the first problem is that the distributions of IP are

Table 5.1: Fitted single exponential values of $C_{FC}(t)$.

		A_0	A_1	A_2	Correlation coefficient
TCTA	D1	0.597222	62.7551	3.39337e-10	0.542082
	D2	0.829677	41.8224	7.27016e-11	0.623581
	D3	0.47053	96.248	1.82471e-10	0.677689
	D4	0.704801	41.0612	5.60474e-11	0.618929
	D5	0.602502	88.2157	6.0544e-11	0.689138

quite different due to incorrect DFTB method for site energy calculations, we may have to go to the ab initio method.

One of the interesting questions regarding the CT mechanism is that whether site energies are correlated or fluctuate independently. However, quantitative simulations of Elstner in DNA demonstrate that the site energy fluctuations are considerably correlated [122, 121]. Thus, the correlation of site-energy fluctuations breaks the simple connections between $\sigma_{\Delta U}, \lambda, K_B T$ in $\sigma_{\Delta U} \approx \sqrt{\lambda K_B T}$. As a consequence, we ignore τ_{FC} which is based on the harmonic approximation and focus on thermal structural fluctuations. Therefore, on the basis of the calculated time series of site energy, we evaluate the correlation function $C_{FC}(t) = \langle\langle \psi^D(t) \,|\, \psi^A(t) \rangle\rangle$ in the 10 ps QM/MM trajectory. The data in Fig. 5.5c show the exponential decay of correlation function of site energies. By comparing the decay time of $C_{FC}(t)$to that of $C_{T_{DA}}(t)$, it can be determined how fast or slow the fluctuations are. Therefore, to obtain the decay time, $C_{FC}(t)$ is fitted to a single exponential equation $y = A_0\, exp(-x/A_1) + A_2$ (the red line). Table 6.1 shows the prefactors (A_0 and A_2), the decay times (A_1) and the correlation coefficient values of the fitted single-exponential curve. The decay time (τ_{FC}) obtained from the fitting, is much longer than that of computed using reorganization energy ($\tau_{FC} = \hbar/\sqrt{\lambda K_B T}$), indicating that simple model may not be suitable and more normal modes may be involved in ϵ_i fluctuations.

To study the relationship between the structural characteristics with the couplings and site energy, and investigate which structural characteristics (e.g. dihedral angles) determine the magnitudes and time scales of T_{DA} fluctuations, we perform the Fourier transform (FT) of correlation function. In particular, we aim to assess the relationship among frequency, ϵ_i and T_{DA} and dihedral angles. To obtain the frequency, the FT is used for the conversion of time-domain signal into frequency-domain signal. Fig. 5.5d shows the Fourier transform of site energies. The frequency of 1600 cm^{-1} (20 fs) is typical for the double bond vibrations of the molecular skeleton [122]. However, the Fourier transform analyses of TCTA indicate that the site energies oscillate with a frequency of 1800 cm^{-1}. In OSCs, C-C stretching is the most dominant mode in the fluctuations of site energy. However, we obtained the τ_{FC} which is much longer than the period of C-C stretching.

5.3.2 Electronic coupling (T_{DA})

We aim to explore the time dependence of T_{DA} arising from structural fluctuations by choosing five molecules from QM/MM trajectories. In this regard, we pick up 5 random molecules (D_i , $i = 1, ..., 5$) with different environments from the snapshots along QM/MM

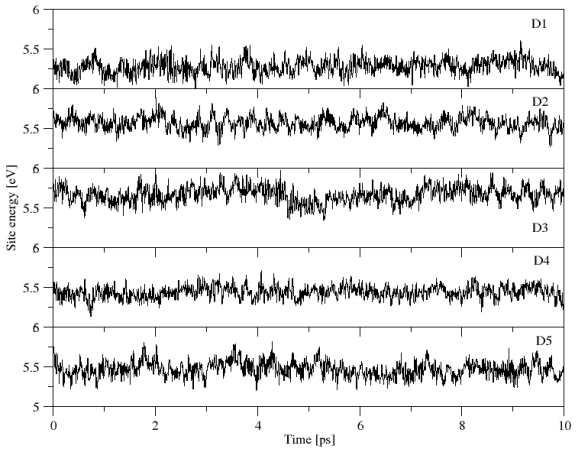

(a) Site energies.

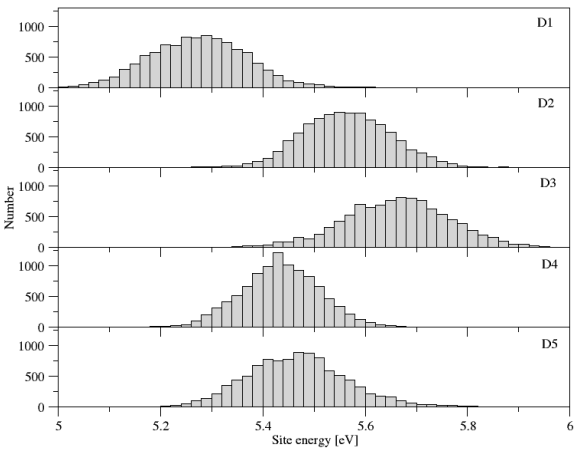

(b) Distribution of site energies.

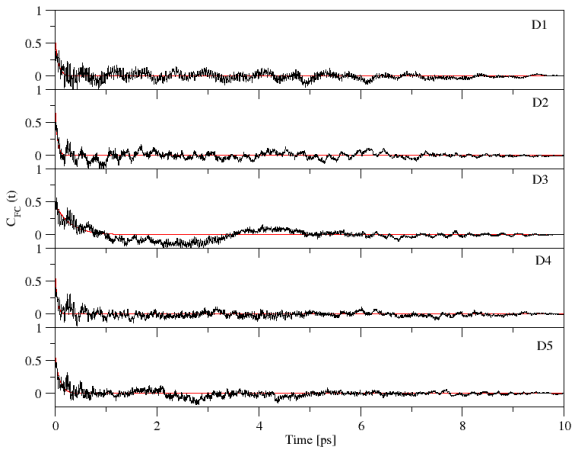

(c) $C_{FC}(t) = \langle\langle \psi^D(t) \,|\, \psi^A(t) \rangle\rangle$.

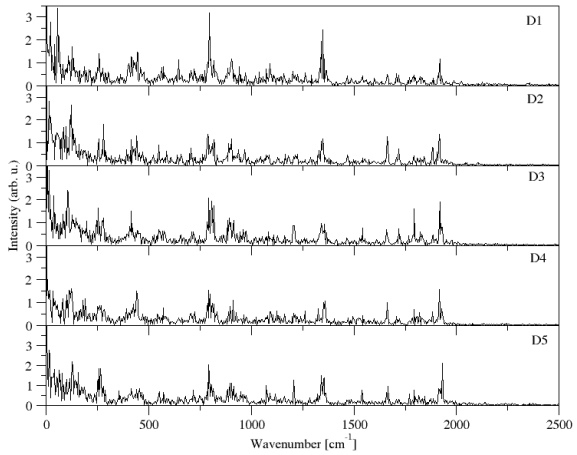

(d) FT of site energies.

Figure 5.5: a) Site energies and b) Distribution of site energies. c) $C_{FC}(t) = \langle\langle \psi^D(t) \,|\, \psi^A(t) \rangle\rangle$ for five individual molecules (D1-D5) of TCTA. Fitted single exponential function are plotted with a red line. d) FT of site energies.

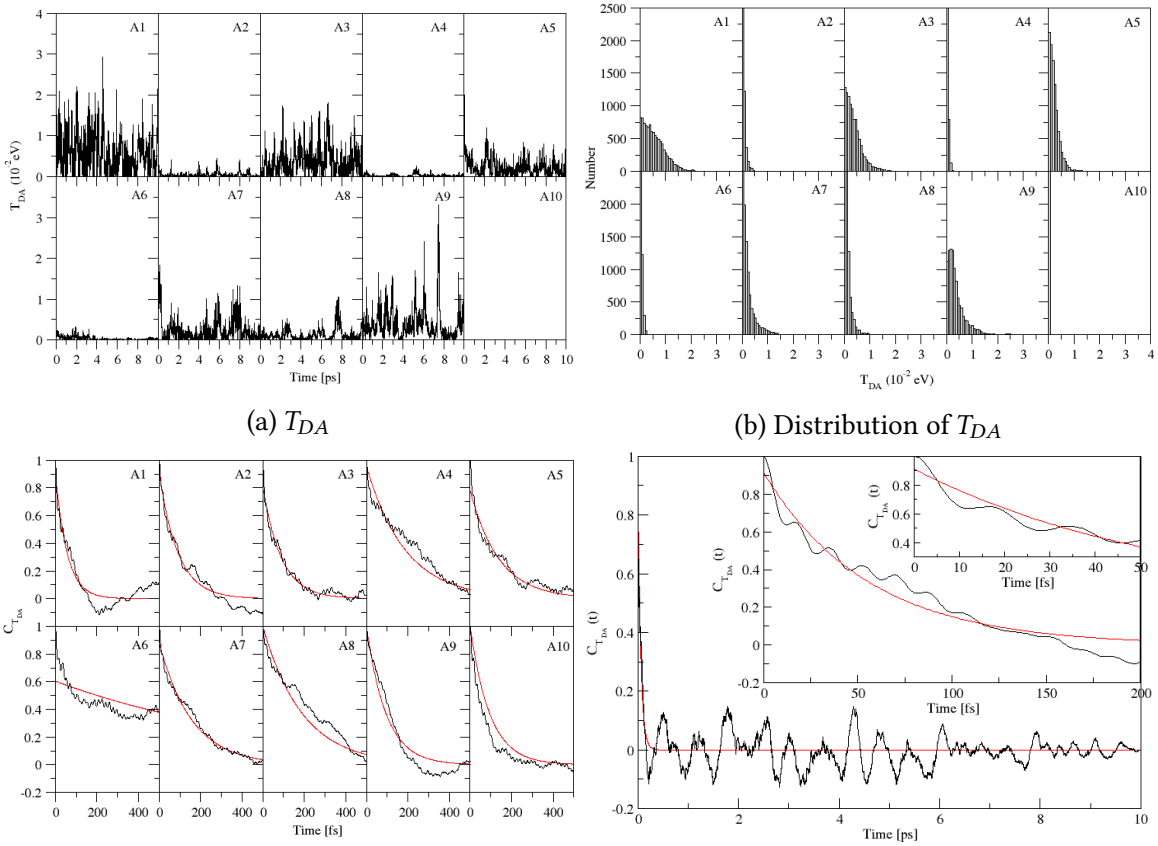

(a) T_{DA}

(b) Distribution of T_{DA}

(c) $C_{T_{DA}}$

(d) Fitting of A1

Figure 5.6: a) Time series of T_{DA} of molecule D1 of **TCTA** with 10 neighbours (A1-A10). The value of T_{DA} is computed using the conformation at every 1 fs for 10 ps. b) Distribution of T_{DA}. c) $C_{T_{DA}}$. d) The black curve represents $C_{T_{DA}}$ of A1 calculated using the simulation data of T_{DA}. The red line obtained by the fit to the black line with use of a function made of single exponentials.

trajectories and find their 10 nearest neighbours (A_{ij} , $j = 1, ..., 10$). The calculation of coupling (T_{DA}) is based on the same sampling procedures using QM/MM simulations, as discussed earlier. Fig. 5.6a shows the time series of electronic coupling of D1 to D5 for TCTA with their 10 nearest neighbours. It has to be noted that, these simulations exhibit a similar pattern for all four OSCs. Amorphous OSCs, which are highly disordered, have small T_{DA}. However, the electronic couplings exhibit large fluctuations. From a practical point of view, the distributions of T_{DA} are almost described by the Gaussian distribution function (Fig. 5.6b). According to this property, $T_{DA}(t)$ should be expressed as a sum of many independently fluctuating elements.

In the following, coherence time (τ_{coh}) and coherence parameter (R_{coh}) are computed to investigate the time scale and the amplitude of fluctuating behavior which may affect the observed ET rate constant. To obtain the fluctuations time scale, T_{DA} fluctuations can be properly characterized by the correlation function of coupling $\langle T_{DA}(t)\, T_{DA}(0)\rangle$, plotted in Fig. 5.6c, 5.6d for TCTA. In the early time region, $C_{T_{DA}}(t)$ decays by an exponentially

Table 5.2: Fitted parameters for $C_{T_{DA}}$ using $y = A0 * exp(-x/A1) + A2$.

			A_0	A_1	A_2	Correlation coefficient
TCTA	D1	A1	0.911871	55.6189	1.87199e-10	0.695020
		A2	0.914399	89.8389	3.13798e-11	0.774433
		A3	0.815112	89.0426	3.459e-10	0.711222
		A4	0.956006	187.095	0.717928	0.717928
		A5	0.779408	139.676	1.28214e-10	0.833046
		A6	0.60339	175.04	2.35593e-11	0.889891
		A7	0.884397	157.034	6.52334e-11	0.765733
		A8	0.9998	191.725	1.16039e-11	0.813569
		A9	0.9988	94.8061	3.97463e-11	0.771426
		A10	0.999999	94.8061	4.93932e-07	0.777399

decreasing function, which indicates that the fluctuating of $T_{DA}(t)$ is based on the nuclear motions. This result indicates that the coherence of nuclear motions is destroyed within $\approx$ 127 fs. Table. 5.2 provides information on the time scale of the coupling fluctuation (lifetime of $T_{DA}(t)$), based on the fitted single-exponential of $C_{T_{DA}}$ using 10,000 snapshots. τ_{coh} values are similar for all materials in this study and is in the same order of magnitude of τ_{FC} (τ_{coh} is a few tens to 100 fs). This characterization of $T_{DA}(t)$ is useful for determining the mechanism of the ET.

According to the aforementioned workflow 5.3, to determine the ET rate regime, firstly we should have a slow variation timescale in the couplings which means that coherence time much larger than FC time, and this is true for all of this system because the reorganization energy is about 0.1 eV. Table. 6.1 shows that the lifetimes of site energy is shorter than the T_{DA} lifetimes in Table. 5.2, indicating that we deal with the slow T_{DA} fluctuation regime. Secondly is the fluctuation strength which is defined by R_{coh} 5.9. To measure the magnitude of T_{DA} fluctuation and consequently investigate how to modify the electronic part in the Marcus theory ($\langle T_{DA} \rangle$ and/or $\langle T_{DA}^2 \rangle$), we compute R_{coh} which is the ratio between the rms of coupling and the square mean of the coupling $\langle T_{DA} \rangle^2 / \langle T_{DA}^2 \rangle$ (Fig. 5.2). This parameter is close to 1 when Frank-Condon approximation is valid and approaches 0 when the coupling strongly depends on the molecular structures. The calculated values of $\langle T_{DA} \rangle^2$, $\langle T_{DA}^2 \rangle$ and R_{coh} for TCTA are shown in Table. 5.6. As can be seen, the coherence parameters vary from $R_{coh} \leq 0.64$ for A1 (strong T_{DA} fluctuations) to 0.28 for A10. Furthermore, the value of R_{coh} in Table. 5.6 indicates that the magnitude of T fluctuations are mostly large. Therefore, the ET rates in the presence of strong fluctuating couplings, can be described by Eq. (5.11) where $C_{T_{DA}}$ in Eq. (5.3) should be replaced by $\langle T_{DA}^2 \rangle$.

Moreover, we compute the instantaneous Marcus rate. As depicted in Fig. 5.7, T_{DA} modulation by molecular dynamics can alter the instantaneous Marcus rates. Particularly, structural fluctuations may enhance or reduce the T_{DA} and consequently alter the observed ET rate.

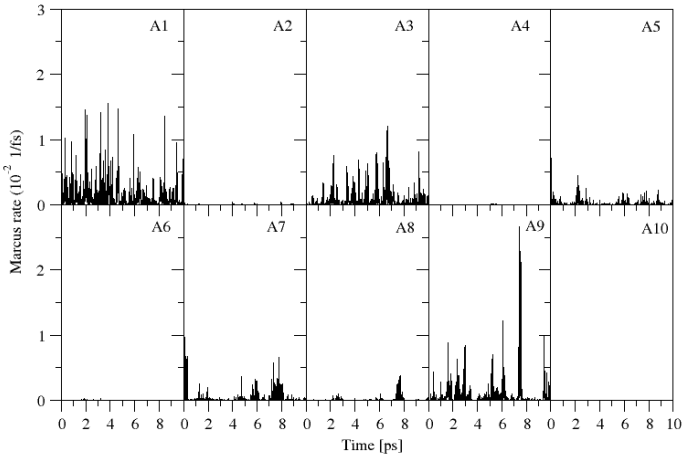

Figure 5.7: Time series of instantaneous Marcus rate (k_{ET}) of an individual molecule D1 of **TCTA** with 10 neighbours (A1-A10). The value of k_{ET} is computed using the conformation at every 1 fs for 10 ps.

Table 5.3: $\langle T_{DA} \rangle$ (10^{-3} eV), $\sqrt{\langle T_{DA}^2 \rangle}$ (10^{-3} eV) and R_{coh}

			$\langle T_{DA} \rangle$	$\sqrt{\langle T_{DA}^2 \rangle}$	R_{coh}
CBP	D1	A1	60	65	0.84
		A2	2.5	3.4	0.57
		A3	0.10	0.14	0.52
		A4			
		A5			
		A6			
		A7			
		A8			
		A9			
		A10			

Table 5.4: $\langle T_{DA} \rangle$ (10^{-3} eV), $\sqrt{\langle T_{DA}^2 \rangle}$ (10^{-3} eV) and R_{coh}

			$\langle T_{DA} \rangle$	$\sqrt{\langle T_{DA}^2 \rangle}$	R_{coh}
p-BPD	D1	A1	3.0	4.5	0.43
		A3	4.3	6.5	0.44
		A4	2.4	3.3	0.52
		A5			
		A6			
		A7			
		A8			
		A9			
		A10			

Table 5.5: $\langle T_{DA} \rangle$ (10^{-3} eV), $\sqrt{\langle T_{DA}^2 \rangle}$ (10^{-3} eV) and R_{coh}

			$\langle T_{DA} \rangle$	$\sqrt{\langle T_{DA}^2 \rangle}$	R_{coh}
TCTA	D1	A1	5.59	6.97	0.64
		A2	0.45	0.73	0.38
		A3	3.73	4.81	0.60
		A4	0.28	0.42	0.45
		A5	2.24	2.99	0.56
		A6	0.35	0.54	0.42
		A7	2.23	3.40	0.43
		A8	1.21	1.82	0.44
		A9	3.90	5.47	0.51
		A10	0.0005	0.0009	0.28

Table 5.6: $\langle T_{DA} \rangle$ (10^{-3} eV), $\sqrt{\langle T_{DA}^2 \rangle}$ (10^{-3} eV) and R_{coh}

			$\langle T_{DA} \rangle$	$\sqrt{\langle T_{DA}^2 \rangle}$	R_{coh}
TPDI	D1	A1	17	21	0.65
		A2	40	50	0.62
		A3	4	6	0.54
		A4			
		A5			
		A6			
		A7			
		A8			
		A9			
		A10			

5.4 Conclusion and outlook

In the current ongoing research project, we aim to study the influence of molecular structure and dynamical disorders on the charge transfer process in amorphous organic semiconductors. The sensitivity of the charge transfer process to structural fluctuations is very well studied in biological systems and in this chapter, we study this effect in organic semiconductors. To describe the dynamical effects, site energies and electronic couplings are calculated along QM/MM trajectories. For four OSCs studied, we found that all computed Franck–Condon decay time (τ_{FC}) values are shorter than τ_{coh}, which indicates that the charge relaxation is much faster than the charge transfer. Moreover, we observed that the average of time scale of coupling fluctuations is ≈ 0.12 ps, which indicates that coupling fluctuations are fast compared to ET time ($\tau_{coh} < 1/k_{ET}$) and slow compared to site energy fluctuations ($\tau_{coh} > \tau_{FC}$). This time scale is sufficiently slow to confine ourselves to slow coupling fluctuation regime.

Moreover, to measure the amplitude of coupling fluctuation, we compute the coherence parameter, defined as the ratio between $\langle T_{DA} \rangle^2$ and $\langle T_{DA}^2 \rangle$. The results show that the coherence parameter is moderately small (≈ 0.5), which indicates that we may have to include the RMS of the coupling in the calculation of rate constant, instead of the coupling average.

The future step in this ongoing research is to investigate the decoherence behaviour by studying the dependence of τ_{coh} on dihedral angle motion. In addition, which structural characteristics determine the magnitudes and time scales of DA coupling fluctuations.

Bibliography

[1] David J Gundlach. “Low power, high impact”. In: *Nature materials* 6.3 (2007), pp. 173–174.

[2] Eleni Stavrinidou, Roger Gabrielsson, Eliot Gomez, Xavier Crispin, Ove Nilsson, Daniel T Simon, and Magnus Berggren. “Electronic plants”. In: *Science advances* 1.10 (2015), e1501136.

[3] Franky So, Junji Kido, and Paul Burrows. “Organic light-emitting devices for solid-state lighting”. In: *MRS bulletin* 33.7 (2008), pp. 663–669.

[4] Sebastian Reineke, Frank Lindner, Gregor Schwartz, Nico Seidler, Karsten Walzer, Björn Lüssem, and Karl Leo. “White organic light-emitting diodes with fluorescent tube efficiency”. In: *Nature* 459.7244 (2009), pp. 234–238.

[5] Yen-Ju Cheng, Sheng-Hsiung Yang, and Chain-Shu Hsu. “Synthesis of conjugated polymers for organic solar cell applications”. In: *Chemical reviews* 109.11 (2009), pp. 5868–5923.

[6] Yanming Sun, Gregory C Welch, Wei Lin Leong, Christopher J Takacs, Guillermo C Bazan, and Alan J Heeger. “Solution-processed small-molecule solar cells with 6.7% efficiency”. In: *Nature materials* 11.1 (2012), pp. 44–48.

[7] Huanli Dong, Xiaolong Fu, Jie Liu, Zongrui Wang, and Wenping Hu. “25th anniversary article: key points for high-mobility organic field-effect transistors”. In: *Advanced materials* 25.43 (2013), pp. 6158–6183.

[8] ME Gershenson, Vitaly Podzorov, and AF Morpurgo. “Colloquium: Electronic transport in single-crystal organic transistors”. In: *Reviews of modern physics* 78.3 (2006), p. 973.

[9] P. Hohenberg and W. Kohn. “Inhomogeneous Electron Gas”. In: *Phys. Rev.* 136.3B (Nov. 1964), B864–B871. DOI: 10.1103/PhysRev.136.B864.

[10] James F Janak. “Proof that E n i= ε in density-functional theory”. In: *Physical Review B* 18.12 (1978), p. 7165.

[11] Ralf Stowasser and Roald Hoffmann. “What do the Kohn- Sham orbitals and eigenvalues mean?” In: *Journal of the american chemical society* 121.14 (1999), pp. 3414–3420.

[12] JF Adams and SB Priddy. “Mathematical proceedings of the cambridge philosophical society”. In: (1927).

[13] M Turkyilmazoglu. “Solution of the Thomas–Fermi equation with a convergent approach”. In: *Communications in Nonlinear Science and Numerical Simulation* 17.11 (2012), pp. 4097–4103.

[14] Walter Kohn and Lu Jeu Sham. "Self-consistent equations including exchange and correlation effects". In: *Physical review* 140.4A (1965), A1133.

[15] David M Ceperley and Berni J Alder. "Ground state of the electron gas by a stochastic method". In: *Physical review letters* 45.7 (1980), p. 566.

[16] John P Perdew, Kieron Burke, and Matthias Ernzerhof. "Generalized gradient approximation made simple". In: *Physical review letters* 77.18 (1996), p. 3865.

[17] Dirk Porezag, Th Frauenheim, Th Köhler, Gotthard Seifert, and R Kaschner. "Construction of tight-binding-like potentials on the basis of density-functional theory: Application to carbon". In: *Physical Review B* 51.19 (1995), p. 12947.

[18] Marcus Elstner, Dirk Porezag, G Jungnickel, J Elsner, M Haugk, Th Frauenheim, Sandor Suhai, and Gotthard Seifert. "Self-consistent-charge density-functional tight-binding method for simulations of complex materials properties". In: *Physical Review B* 58.11 (1998), p. 7260.

[19] JJ Kwiatkowski, J Nelson, H Li, Jean-Luc Bredas, W Wenzel, and C Lennartz. "Simulating charge transport in tris (8-hydroxyquinoline) aluminium (Alq 3)". In: *Physical Chemistry Chemical Physics* 10.14 (2008), pp. 1852–1858.

[20] Pascal Friederich, Velimir Meded, Angela Poschlad, Tobias Neumann, Vadim Rodin, Vera Stehr, Franz Symalla, Denis Danilov, Gesa Lüdemann, Reinhold F Fink, et al. "Molecular origin of the charge carrier mobility in small molecule organic semiconductors". In: *Advanced Functional Materials* 26.31 (2016), pp. 5757–5763.

[21] Pascal Kordt, Jeroen JM van der Holst, Mustapha Al Helwi, Wolfgang Kowalsky, Falk May, Alexander Badinski, Christian Lennartz, and Denis Andrienko. "Modeling of organic light emitting diodes: From molecular to device properties". In: *Advanced Functional Materials* 25.13 (2015), pp. 1955–1971.

[22] Victor Rühle, Alexander Lukyanov, Falk May, Manuel Schrader, Thorsten Vehoff, James Kirkpatrick, Björn Baumeier, and Denis Andrienko. "Microscopic simulations of charge transport in disordered organic semiconductors". In: *Journal of chemical theory and computation* 7.10 (2011), pp. 3335–3345.

[23] Alessandro Troisi, Abraham Nitzan, and Mark A Ratner. "A rate constant expression for charge transfer through fluctuating bridges". In: *The Journal of chemical physics* 119.12 (2003), pp. 5782–5788.

[24] Spiros S Skourtis, Jianping Lin, and David N Beratan. "The effects of bridge motion on electron transfer reactions mediated by tunneling". In: *Modern Methods for Theoretical Physical Chemistry of Biopolymers*. Elsevier, 2006, pp. 357–382.

[25] Samaneh Inanlou, Rodrigo Cortés-Mejıa, Ali Deniz Özdemir, Sebastian Höfener, Wim Klopper, Wolfgang Wenzel, Weiwei Xie, and Marcus Elstner. "Understanding excited state properties of host materials in OLEDs: simulation of absorption spectrum of amorphous 4, 4-bis (carbazol-9-yl)-2, 2-biphenyl (CBP)". In: *Physical Chemistry Chemical Physics* 24.7 (2022), pp. 4576–4587.

[26] Qi Wang, Bin Sun, and Hany Aziz. “Exciton–Polaron-induced aggregation of wide-bandgap materials and its implication on the electroluminescence stability of phosphorescent organic light-emitting devices”. In: *Advanced Functional Materials* 24.20 (2014), pp. 2975–2985.

[27] Ramanaskanda Braveenth, Hasu Jung, Keunhwa Kim, Bo Mi Kim, Il-Ji Bae, Miyoung Kim, and Kyu Yun Chai. “Fluorene–Triphenylamine-Based Bipolar Materials: Fluorescent Emitter and Host for Yellow Phosphorescent OLEDs”. In: *Applied Sciences* 10.2 (2020), p. 519.

[28] Takashi Ito, Hisahiro Sasabe, Yuji Nagai, Yuichiro Watanabe, Natsuki Onuma, and Junji Kido. “A Series of Dibenzofuran-Based n-Type Exciplex Host Partners Realizing High-Efficiency and Stable Deep-Red Phosphorescent OLEDs”. In: *Chemistry–A European Journal* 25.30 (2019), pp. 7308–7314.

[29] Junji Kido, Masato Kimura, and Katsutoshi Nagai. “Multilayer white light-emitting organic electroluminescent device”. In: *Science* 267.5202 (1995), pp. 1332–1334.

[30] Ramanaskanda Braveenth, Hyeong Woo Bae, Ik Jang Ko, Wu Qiong, Quynh Pham Bao Nguyen, Pothupitiya Gamage Sudesh Jayashantha, Jang Hyuk Kwon, and Kyu Yun Chai. “Thermally stable efficient hole transporting materials based on carbazole and triphenylamine core for red phosphorescent OLEDs”. In: *Organic Electronics* 51 (2017), pp. 463–470.

[31] Bo Mi Kim, Quynh Pham Bao Nguyen, Jin Guo Fan, Mi Jin Kim, Ramanaskanda Braveenth, Gyeong Woo Kim, Jang Hyuk Kwon, and Kyu Yun Chai. “Novel Star-shaped Hole-transporting Materials Based on Triphenylamine Cores End-capped with Carbazole and Triarylamine Derivatives for use in OLEDs”. In: *Bulletin of the Korean Chemical Society* 36.4 (2015), pp. 1303–1306.

[32] Youtian Tao, Chuluo Yang, and Jingui Qin. “Organic host materials for phosphorescent organic light-emitting diodes”. In: *Chemical Society Reviews* 40.5 (2011), pp. 2943–2970.

[33] Jia-Xiong Chen, Wen-Wen Tao, Ya-Fang Xiao, Shuang Tian, Wen-Cheng Chen, Kai Wang, Jia Yu, Feng-Xia Geng, Xiao-Hong Zhang, and Chun-Sing Lee. “Isomeric thermally activated delayed fluorescence emitters based on indolo [2, 3-b] acridine electron-donor: a compromising optimization for efficient orange–red organic light-emitting diodes”. In: *Journal of Materials Chemistry C* 7.10 (2019), pp. 2898–2904.

[34] Peter Strohriegl and Juozas V Grazulevicius. “Charge-transporting molecular glasses”. In: *Advanced Materials* 14.20 (2002), pp. 1439–1452.

[35] Roland Schmechel and Heinz Von Seggern. “Electronic traps in organic transport layers”. In: *Physica status solidi (a)* 201.6 (2004), pp. 1215–1235.

[36] Yingjie Zhang and Hany Aziz. “Influence of the guest on aggregation of the host by exciton–polaron interactions and its effects on the stability of phosphorescent organic light-emitting devices”. In: *ACS Applied Materials & Interfaces* 8.22 (2016), pp. 14088–14095.

[37] Marcus Elstner and Gotthard Seifert. "Density functional tight binding". In: *Philosophical Transactions of the Royal Society A: Mathematical, Physical and Engineering Sciences* 372.2011 (2014), p. 20120483.

[38] Tomas Kubar, Zoltan Bodrog, Michael Gaus, Christof Köhler, Balint Aradi, Thomas Frauenheim, and Marcus Elstner. "Parametrization of the SCC-DFTB Method for Halogens". In: *Journal of Chemical Theory and Computation* 9.7 (2013), pp. 2939–2949.

[39] Thomas A Niehaus. "Approximate time-dependent density functional theory". In: *Journal of Molecular Structure: THEOCHEM* 914.1-3 (2009), pp. 38–49.

[40] John P Perdew, Matthias Ernzerhof, and Kieron Burke. "Rationale for mixing exact exchange with density functional approximations". In: *The Journal of chemical physics* 105.22 (1996), pp. 9982–9985.

[41] Tomás Kubar, P Benjamin Woiczikowski, Gianaurelio Cuniberti, and Marcus Elstner. "Efficient calculation of charge-transfer matrix elements for hole transfer in DNA". In: *The Journal of Physical Chemistry B* 112.26 (2008), pp. 7937–7947.

[42] Qiang Cui, Marcus Elstner, Efthimios Kaxiras, Thomas Frauenheim, and Martin Karplus. "A QM/MM implementation of the self-consistent charge density functional tight binding (SCC-DFTB) method". In: *The Journal of Physical Chemistry B* 105.2 (2001), pp. 569–585.

[43] Van Quan Vuong, Jissy Akkarapattiakal Kuriappan, Maximilian Kubillus, Julian J Kranz, Thilo Mast, Thomas A Niehaus, Stephan Irle, and Marcus Elstner. "Parametrization and benchmark of long-range corrected DFTB2 for organic molecules". In: *Journal of Chemical Theory and Computation* 14.1 (2018), pp. 115–125.

[44] Julian J Kranz, Marcus Elstner, Bálint Aradi, Thomas Frauenheim, Vitalij Lutsker, Adriel Dominguez Garcia, and Thomas A Niehaus. "Time-dependent extension of the long-range corrected density functional based tight-binding method". In: *Journal of Chemical Theory and Computation* 13.4 (2017), pp. 1737–1747.

[45] Beatrix M Bold, Monja Sokolov, Sayan Maity, Marius Wanko, Philipp M Dohmen, Julian J Kranz, Ulrich Kleinekathöfer, Sebastian Höfener, and Marcus Elstner. "Benchmark and performance of long-range corrected time-dependent density functional tight binding (LC-TD-DFTB) on rhodopsins and light-harvesting complexes". In: *Physical Chemistry Chemical Physics* 22.19 (2020), pp. 10500–10518.

[46] Yasuhiko Shirota and Hiroshi Kageyama. "Charge carrier transporting molecular materials and their applications in devices". In: *Chemical reviews* 107.4 (2007), pp. 953–1010.

[47] Michael Gaus, Albrecht Goez, and Marcus Elstner. "Parametrization and benchmark of DFTB3 for organic molecules". In: *Journal of Chemical Theory and Computation* 9.1 (2013), pp. 338–354.

[48] Nils Schieschke, Beatrix M Bold, Philipp M Dohmen, Daniel Wehl, Marvin Hoffmann, Andreas Dreuw, Marcus Elstner, and Sebastian Höfener. "Geometry dependence of excitonic couplings and the consequences for configuration-space sampling". In: *Journal of Computational Chemistry* 42.20 (2021), pp. 1402–1418.

[49] Ben Hourahine, Bálint Aradi, Volker Blum, F Bonafé, A Buccheri, Cristopher Camacho, Caterina Cevallos, MY Deshaye, T Dumitrică, A Dominguez, et al. "DFTB+, a software package for efficient approximate density functional theory based atomistic simulations". In: *The Journal of chemical physics* 152.12 (2020), p. 124101.

[50] *TURBOMOLE V7.0 2015, a Development of University of Karlsruhe and Forschungszentrum Karlsruhe GmbH, 1989-2007, TURBOMOLE GmbH, since 2007, Available from http://www.turbomole.com.*

[51] Michael J. Frisch et al. *Gaussian 09*. Wallingford, CT, USA: Gaussian, Inc., 2009.

[52] Rodrigo Cortés-Mejıa, Sebastian Höfener, and Wim Klopper. "Effects of rotational conformation on electronic properties of 4, 4-bis (carbazol-9-yl) biphenyl (CBP): the single-molecule picture and beyond". In: *Molecular Physics* 119.8 (2021), e1876936.

[53] Katharina Krause and Wim Klopper. *Implementation of the Bethe- Salpeter equation in the TURBOMOLE program*. 2017.

[54] Xin Gui, Christof Holzer, and Wim Klopper. "Accuracy assessment of GW starting points for calculating molecular excitation energies using the Bethe–Salpeter formalism". In: *Journal of Chemical Theory and Computation* 14.4 (2018), pp. 2127–2136.

[55] Carlo Adamo and Vincenzo Barone. "Toward reliable density functional methods without adjustable parameters: The PBE0 model". In: *The Journal of chemical physics* 110.13 (1999), pp. 6158–6170.

[56] Florian Weigend and Reinhart Ahlrichs. "Balanced basis sets of split valence, triple zeta valence and quadruple zeta valence quality for H to Rn: Design and assessment of accuracy". In: *Physical Chemistry Chemical Physics* 7.18 (2005), pp. 3297–3305.

[57] Ansgar Schäfer, Christian Huber, and Reinhart Ahlrichs. "Fully optimized contracted Gaussian basis sets of triple zeta valence quality for atoms Li to Kr". In: *The Journal of Chemical Physics* 100.8 (1994), pp. 5829–5835.

[58] Michiel J van Setten, Florian Weigend, and Ferdinand Evers. "The GW-method for quantum chemistry applications: Theory and implementation". In: *Journal of chemical theory and computation* 9.1 (2013), pp. 232–246.

[59] Junmei Wang, Romain M Wolf, James W Caldwell, Peter A Kollman, and David A Case. "Development and testing of a general amber force field". In: *Journal of computational chemistry* 25.9 (2004), pp. 1157–1174.

[60] Junmei Wang, Wei Wang, Peter A Kollman, and David A Case. "Automatic atom type and bond type perception in molecular mechanical calculations". In: *Journal of molecular graphics and modelling* 25.2 (2006), pp. 247–260.

[61] U Chandra Singh and Peter A Kollman. "An approach to computing electrostatic charges for molecules". In: *Journal of computational chemistry* 5.2 (1984), pp. 129–145.

[62] Brent H Besler, Kenneth M Merz Jr, and Peter A Kollman. "Atomic charges derived from semiempirical methods". In: *Journal of computational chemistry* 11.4 (1990), pp. 431–439.

[63] aGA Petersson, Andrew Bennett, Thomas G Tensfeldt, Mohammad A Al-Laham, William A Shirley, and John Mantzaris. "A complete basis set model chemistry. I. The total energies of closed-shell atoms and hydrides of the first-row elements". In: *The Journal of chemical physics* 89.4 (1988), pp. 2193–2218.

[64] GA Petersson and Mohammad A Al-Laham. "A complete basis set model chemistry. II. Open-shell systems and the total energies of the first-row atoms". In: *The Journal of chemical physics* 94.9 (1991), pp. 6081–6090.

[65] Sundaram Arulmozhiraja and Toshihiro Fujii. "Torsional barrier, ionization potential, and electron affinity of biphenyl—A theoretical study". In: *The Journal of Chemical Physics* 115.23 (2001), pp. 10589–10594.

[66] Denis J Evans and Brad Lee Holian. "The nose–hoover thermostat". In: *The Journal of chemical physics* 83.8 (1985), pp. 4069–4074.

[67] Berk Hess, Carsten Kutzner, David Van Der Spoel, and Erik Lindahl. "GROMACS 4: algorithms for highly efficient, load-balanced, and scalable molecular simulation". In: *Journal of chemical theory and computation* 4.3 (2008), pp. 435–447.

[68] Tobias Neumann, Denis Danilov, Christian Lennartz, and Wolfgang Wenzel. "Modeling disordered morphologies in organic semiconductors". In: *Journal of computational chemistry* 34.31 (2013), pp. 2716–2725.

[69] D. J. Evans and B. L. Holian. "The Nose–Hoover Thermostat". en. In: *J. Chem. Phys.* 83.8 (1985), p. 4069. ISSN: 00219606. DOI: 10.1063/1.449071.

[70] Michele Parrinello and Aneesur Rahman. "Polymorphic transitions in single crystals: A new molecular dynamics method". In: *Journal of Applied physics* 52.12 (1981), pp. 7182–7190.

[71] Tomáš Kubař, Kai Welke, and Gerrit Groenhof. *New QM/MM implementation of the DFTB3 method in the gromacs package*. 2015.

[72] Liang Zhou, Hongjie Zhang, Ruiping Deng, Zhefeng Li, Jiangbo Yu, and Zhiyong Guo. "Conversion process of the dominant electroluminescence mechanism in a molecularly doped organic light-emitting device with only electron trapping". In: *Journal of Applied Physics* 102.6 (2007), p. 064504.

[73] Ankit Rohatgi. "Webplotdigitizer version 4.2, 2019". In: *URL https://automeris.io/WebPlotDigitizer* (2020).

[74] Per-Arno Plötz, Thomas Niehaus, and Oliver Kühn. "A new efficient method for calculation of Frenkel exciton parameters in molecular aggregates". In: *The Journal of Chemical Physics* 140.17 (2014), p. 174101.

[75] Monja Sokolov, Beatrix M Bold, Julian J Kranz, Sebastian Hofener, Thomas A Niehaus, and Marcus Elstner. "Analytical Time-Dependent Long-Range Corrected Density Functional Tight Binding (TD-LC-DFTB) Gradients in DFTB+: Implementation and Benchmark for Excited-State Geometries and Transition Energies". In: *Journal of Chemical Theory and Computation* 17.4 (2021), pp. 2266–2282.

[76] Julian J Kranz, Marcus Elstner, Bálint Aradi, Thomas Frauenheim, Vitalij Lutsker, Adriel Dominguez Garcia, and Thomas A Niehaus. "Time-Dependent Extension of the Long-Range Corrected Density Functional Based Tight-Binding Method". In: *J Chem Theory Comput* 13.4 (2017), pp. 1737–1747.

[77] Monja Sokolov, Beatrix M. Bold, Julian J. Kranz, Sebastian Höfener, Thomas A. Niehaus, and Marcus Elstner. "Analytical Time-Dependent Long-Range Corrected Density Functional Tight Binding (TD-LC-DFTB) Gradients in DFTB+: Implementation and Benchmark for Excited-State Geometries and Transition Energies". In: *J. Chem. Theory Comput.* 17.4 (Apr. 2021), pp. 2266–2282. ISSN: 1549-9618. DOI: 10.1021/acs.jctc.1c00095.

[78] Marius Wanko, Michael Hoffmann, Paul Strodel, Axel Koslowski, Walter Thiel, Frank Neese, Thomas Frauenheim, and Marcus Elstner. "Calculating absorption shifts for retinal proteins: computational challenges". In: *The Journal of Physical Chemistry B* 109.8 (2005), pp. 3606–3615.

[79] ME Madjet, A Abdurahman, and Th Renger. "Intermolecular Coulomb couplings from ab initio electrostatic potentials: application to optical transitions of strongly coupled pigments in photosynthetic antennae and reaction centers". In: *The Journal of Physical Chemistry B* 110.34 (2006), pp. 17268–17281.

[80] Carsten Olbrich, Thomas LC Jansen, Jörg Liebers, Mortaza Aghtar, Johan Strümpfer, Klaus Schulten, Jasper Knoester, and Ulrich Kleinekathöfer. "From atomistic modeling to excitation transfer and two-dimensional spectra of the FMO light-harvesting complex". In: *The Journal of Physical Chemistry B* 115.26 (2011), pp. 8609–8621.

[81] Qi Wang and Hany Aziz. "Exciton–Polaron-Induced Aggregation of Organic Electroluminescent Materials: A Major Degradation Mechanism in Wide-Bandgap Phosphorescent and Fluorescent Organic Light-Emitting Devices". In: *Advanced Optical Materials* 3.7 (2015), pp. 967–975.

[82] Kuk-Youn Ju, Martin C Fischer, and Warren S Warren. "Understanding the role of aggregation in the broad absorption bands of eumelanin". In: *ACS nano* 12.12 (2018), pp. 12050–12061.

[83] GR Suman, Mayank Pandey, and AS Jeevan Chakravarthy. "Review on new horizons of aggregation induced emission: from design to development". In: *Materials Chemistry Frontiers* 5.4 (2021), pp. 1541–1584.

[84] Spiros S Skourtis, David H Waldeck, and David N Beratan. "Fluctuations in biological and bioinspired electron-transfer reactions". In: *Annual review of physical chemistry* 61 (2010), pp. 461–485.

[85] Harry B Gray and Jay R Winkler. "Electron tunneling through proteins". In: *Quarterly reviews of biophysics* 36.3 (2003), pp. 341–372.

[86] David N Beratan and JJ Hopfield. "Failure of the Born–Oppenheimer and Franck–Condon approximations for long distance electron transfer rate calculations". In: *The Journal of chemical physics* 81.12 (1984), pp. 5753–5759.

[87] Kurt V Mikkelsen, Jens Ulstrup, and Merab G Zakaraya. "Free energy-dependence of the electronic factor in biological long-range electron transfer". In: *Journal of the American Chemical Society* 111.4 (1989), pp. 1315–1319.

[88] José Nelson Onuchic, David N Beratan, and JJ Hopfield. "Some aspects of electron-transfer reaction dynamics." In: *The Journal of Physical Chemistry* 90.16 (1986), pp. 3707–3721.

[89] Spiros S Skourtis, Georgios Archontis, and Qian Xie. "Electron transfer through fluctuating bridges: On the validity of the superexchange mechanism and time-dependent tunneling matrix elements". In: *The Journal of Chemical Physics* 115.20 (2001), pp. 9444–9462.

[90] Ilya A Balabin and José N Onuchic. "Dynamically controlled protein tunneling paths in photosynthetic reaction centers". In: *Science* 290.5489 (2000), pp. 114–117.

[91] Marshall D Newton. "Modeling donor/acceptor interactions: combined roles of theory and computation". In: *International Journal of Quantum Chemistry* 77.1 (2000), pp. 255–263.

[92] Alessandro Troisi and Giorgio Orlandi. "Hole migration in DNA: a theoretical analysis of the role of structural fluctuations". In: *The journal of physical chemistry B* 106.8 (2002), pp. 2093–2101.

[93] Tsutomu Kawatsu, Toshiaki Kakitani, and Takahisa Yamato. "Destructive interference in the electron tunneling through protein media". In: *The Journal of Physical Chemistry B* 106.43 (2002), pp. 11356–11366.

[94] Alessandro Troisi, Mark A Ratner, and Matthew B Zimmt. "Dynamic nature of the intramolecular electronic coupling mediated by a solvent molecule: A computational study". In: *Journal of the American Chemical Society* 126.7 (2004), pp. 2215–2224.

[95] Alessandro Troisi, Abraham Nitzan, and Mark A. Ratner. "A rate constant expression for charge transfer through fluctuating bridges". In: *The Journal of Chemical Physics* 119.12 (2003), pp. 5782–5788. DOI: 10.1063/1.1601600. eprint: https://doi.org/10.1063/1.1601600. URL: https://doi.org/10.1063/1.1601600.

[96] Spiros S Skourtis, Ilya A Balabin, Tsutomu Kawatsu, and David N Beratan. "Protein dynamics and electron transfer: Electronic decoherence and non-Condon effects". In: *Proceedings of the National Academy of Sciences* 102.10 (2005), pp. 3552–3557.

[97] Neil R Kestner, Jean Logan, and Joshua Jortner. "Thermal electron transfer reactions in polar solvents". In: *The Journal of Physical Chemistry* 78.21 (1974), pp. 2148–2166.

[98] Rudolph A Marcus and Norman Sutin. "Electron transfers in chemistry and biology". In: *Biochimica et Biophysica Acta (BBA)-Reviews on Bioenergetics* 811.3 (1985), pp. 265–322.

[99] Noel Sydney Hush. “Adiabatic theory of outer sphere electron-transfer reactions in solution”. In: *Transactions of the Faraday Society* 57 (1961), pp. 557–580.

[100] Rudolph A Marcus. “On the theory of electron-transfer reactions. VI. Unified treatment for homogeneous and electrode reactions”. In: *The Journal of Chemical Physics* 43.2 (1965), pp. 679–701.

[101] E Pahl, H-D Meyer, LS Cederbaum, D Minelli, and F Tarantelli. “Adiabatic and nonadiabatic effects of nuclear dynamics in spectra of decaying states: Auger spectrum of HF”. In: *The Journal of chemical physics* 105.20 (1996), pp. 9175–9181.

[102] E Pahl, J Brand, LS Cederbaum, and F Tarantelli. “Impact of narrow-band excitation on resonant decay spectra”. In: *Physical Review A* 60.2 (1999), p. 1079.

[103] Melvin Lax. “The Franck-Condon principle and its application to crystals”. In: *The Journal of chemical physics* 20.11 (1952), pp. 1752–1760.

[104] Eyal Neria and Abraham Nitzan. “Semiclassical evaluation of nonadiabatic rates in condensed phases”. In: *The Journal of chemical physics* 99.2 (1993), pp. 1109–1123.

[105] Oleg V Prezhdo and Peter J Rossky. “Evaluation of quantum transition rates from quantum-classical molecular dynamics simulations”. In: *The Journal of chemical physics* 107.15 (1997), pp. 5863–5878.

[106] J Tang. “Effects of a fluctuating electronic coupling matrix element on electron transfer rate”. In: *The Journal of chemical physics* 98.8 (1993), pp. 6263–6266.

[107] Hirotaka Nishioka, Akihiro Kimura, Takahisa Yamato, Tsutomu Kawatsu, and Toshiaki Kakitani. “Interference, fluctuation, and alternation of electron tunneling in protein media. 1. Two tunneling routes in photosynthetic reaction center alternate due to thermal fluctuation of protein conformation”. In: *The Journal of Physical Chemistry B* 109.5 (2005), pp. 1978–1987.

[108] M. Bixon and J. Jortner. “Effects of Configurational Fluctuation on Electronic Coupling for Charge Transfer Dynamics”. In: *Russian Journal of Electrochemistry* 39.1 (Jan. 2003), pp. 3–8. ISSN: 1023-1935. DOI: 10.1023/A:1021951109933.

[109] M Bixon and J Jortner. “Effects of configurational fluctuation on electronic coupling for charge transfer dynamics”. In: *Russian journal of electrochemistry* 39.1 (2003), pp. 3–8.

[110] Yuri A Berlin, Ferdinand C Grozema, Laurens DA Siebbeles, and Mark A Ratner. “Charge transfer in donor-bridge-acceptor systems: Static disorder, dynamic fluctuations, and complex kinetics”. In: *The Journal of Physical Chemistry C* 112.29 (2008), pp. 10988–11000.

[111] JL Liao and Gregory A Voth. “Numerical approaches for computing nonadiabatic electron transfer rate constants”. In: *The Journal of chemical physics* 116.21 (2002), pp. 9174–9187.

[112] Anatoli Milischuk and Dmitry V Matyushov. “Non-Condon theory of nonadiabatic electron transfer reactions in V-shaped donor–bridge–acceptor complexes”. In: *The Journal of chemical physics* 118.12 (2003), pp. 5596–5606.

[113] Herman JC Berendsen, David van der Spoel, and Rudi van Drunen. "GROMACS: A message-passing parallel molecular dynamics implementation". In: *Computer physics communications* 91.1-3 (1995), pp. 43–56.

[114] Mark James Abraham, Teemu Murtola, Roland Schulz, Szilárd Páll, Jeremy C Smith, Berk Hess, and Erik Lindahl. "GROMACS: High performance molecular simulations through multi-level parallelism from laptops to supercomputers". In: *SoftwareX* 1 (2015), pp. 19–25.

[115] MJ Frisch, GW Trucks, HB Schlegel, GE Scuseria, MA Robb, JR Cheeseman, G Scalmani, V Barone, B Mennucci, GA Petersson, et al. "Gaussian 09; Gaussian, Inc". In: *Wallingford, CT* 32 (2009), pp. 5648–5652.

[116] Stefano Markidis, Erwin Laure, S Markidis, and E Laure. "Solving software challenges for Exascale". In: *International Conference on Exascale Applications and Software*. Springer. 2015, pp. 3–27.

[117] Hans Martin Senn and Walter Thiel. "QM/MM studies of enzymes". In: *Current opinion in chemical biology* 11.2 (2007), pp. 182–187.

[118] Adam Kubas, Felix Hoffmann, Alexander Heck, Harald Oberhofer, Marcus Elstner, and Jochen Blumberger. "Electronic couplings for molecular charge transfer: Benchmarking CDFT, FODFT, and FODFTB against high-level ab initio calculations". In: *The Journal of chemical physics* 140.10 (2014), p. 104105.

[119] Orestis George Ziogos, Adam Kubas, Zdenek Futera, Weiwei Xie, Marcus Elstner, and Jochen Blumberger. "HAB79: A new molecular dataset for benchmarking DFT and DFTB electronic couplings against high-level ab initio calculations". In: *The Journal of Chemical Physics* 155.23 (2021), p. 234115.

[120] Adam Kubas, Fruzsina Gajdos, Alexander Heck, Harald Oberhofer, Marcus Elstner, and Jochen Blumberger. "Electronic couplings for molecular charge transfer: benchmarking CDFT, FODFT and FODFTB against high-level ab initio calculations. II". In: *Physical Chemistry Chemical Physics* 17.22 (2015), pp. 14342–14354.

[121] Tomáš Kubař, Ulrich Kleinekathöfer, and Marcus Elstner. "Solvent fluctuations drive the hole transfer in DNA: a mixed quantum- classical study". In: *The Journal of Physical Chemistry B* 113.39 (2009), pp. 13107–13117.

[122] Tomas Kubar and Marcus Elstner. "What governs the charge transfer in DNA? The role of DNA conformation and environment". In: *The Journal of Physical Chemistry B* 112.29 (2008), pp. 8788–8798.

List of Figures

1.1 The working principle of a typical OLED: 1. injection of electrons and holes, 2. transport of the two types of carriers, 3. formation of the exciton between the two organic layers, 4. the emission of light. 2

3.1 Illustration of the formation of delocalized π orbitals in ethene. Both carbon atoms contribute in the formation of sp^2 (s, p_x and p_y) hybrid orbitals. These hybrid orbitals are aligned in the xy-palne, whereas p_z orbital is perpendicular to the sp^2 plane. (source:https://www.heftfilme.de/) 22
3.2 Illustration of the energy between the HOMO and LUMO in ethene. The gap between the HOMO and LUMO determines the semicondution nature of the organic material. (source:https://chem.libretexts.org/) 23
3.3 Donor and acceptor potential surfaces and accepting mode vibrational energies (Reprinted from [24]). 26

4.1 (a) Schematic representation of the 4,4'-bis(N-carbazolyl)-1,1'- biphenyl (CBP). α , β and γ are the side dihedral angle, central dihedral angle, and improper dihedral angle. (b) Marked bonds in red are considered in calculation of BLA. 33
4.2 a) Distributions of central (upper panel), and side (center panel) and improper (lower panel) angles obtained by MD sampling using original GAFF and reparameterized GAFF force fields. b) Potential energy relaxed scans along central (upper panel), and side (center panel) and improper (lower panel) angles using ωB97XD/6-311g+(d,p) (black) and original GAFF (red) and reparameterized GAFF (green). 35
4.3 Influence of the applied methods on the computed vertical excitation energies. The x-axis shows the methods used to compute the ground state geometries; vertical excitation energies are then computed with various methods for these respective geometries. Note that, ADC(2) and GW-BSE are superimposed. 38
4.4 Excitation energies (eV) for different optimized geometries with constraint dihedral angles. 40
4.5 Absorption spectra of CBP in the gas phase and Kohn–Sham orbitals involved in the main orbital transitions of CBP. TD-DFTB, TD-LC-DFTB and GW-BSE calculations are shown in purple, blue and green lines, respectively. The excited states calculations are based on the global minimum geometry taken from ref. [52]. 42
4.6 Electron transitions relevant to HOMO-n (n=1,2,4) obtained by LC-DFTB. 42

4.7 Absorption spectra computed by TD-LC-DFTB for different central (a) and side (b) dihedral angles. 43
4.8 LCDFTB KohnSham orbitals involved in the excitation of the lowest-energy peak for side α and central β dihedral angles at 0°and 90°. 44
4.9 (a) Absorption spectra for the ensemble-snapshot of 5000 molecules (ensemble, displayed top at the left) and for the 5 ns trajectories of the three molecules picked from the ensemble. (b) Distribution of dihedral angles obtained for the ensemble and along the time-series of the three individual molecules. Note that the molecule is not symmetric and therefore a presentation 1–90° is not appropriate. 45
4.10 Comparison of absorption spectra for an ensemble-snapshot of 5000 molecules with and without considering electrostatic effect on excitation energy calculations. The electrostatic effects were considered by the point charge scheme. 46
4.11 (a) Absorption spectra and (b) distribution of dihedral angles for the ensemble-snapshot of 5000 molecules and molecules M1, M2 and M3 obtained by a 10 ns trajectory. 47
4.12 Absorption spectra (a) and central dihedral angle distributions (b) for each ns MD simulation in a 10 ns trajectory of molecule M1. 47
4.13 (a) Absorption spectra of CBP obtained using the conformations from gas-phase MD (blue line) and one condensed-phase MD-snapshot (red line) and (b) the corresponding central and side dihedral angle distributions. 48
4.14 Partial absorption spectra of (a) central and (b) side dihedral angles are shown for three categories, 0°–30° and 150°–180° (blue), 30°–60° and 120°–150° (green) and 60°–90° and 90°–120° (red). 49
4.15 Convergence of the absorption spectra (a) and dihedral angles (b) with the number of individual molecules sampled in the supercell. From a 5 ns MD trajectory, three sets of molecules containing 10, 20 and 50 molecules are randomly selected and 500, 250 and 100 snapshots are taken for these three sets, respectively, to maintain the same number of structures in every test set. 50
4.16 (a) A comparison of the experimental absorption spectrum of CBP taken from ref. 45 with the absorption spectra obtained using the structures from QM/MM simulations and one condensed-phase MD-snapshot. (b) Central and side dihedral angle distributions obtained by QM/MM (upper panel) and MD (lower panel) simulations. 51
4.17 (a) Nearest-neighbor excitonic coupling distributions. (b) Excitonic coupling dependent absorption spectra of monomers (solid lines) and dimers (dashed lines). (c) Central and side dihedral angle distributions. 52

5.1 Donor and acceptor potential surfaces. ET takes place when D and A are at resonance conformation. 55
5.2 Decay time (τ_{coh}) of $C_{T_{DA}}(t)$ (Reprinted from [24]). 58
5.3 Workflow of nonadiabatic ET rate regimes. 59

5.4 Schematic structures of the hole-transport materials characterized in this work. 61
5.5 a) Site energies and b) Distribution of site energies. c) $C_{FC}(t) = \langle\langle \psi^D(t) \mid \psi^A(t)\rangle\rangle$ for five individual molecules (D1-D5) of TCTA. Fitted single exponential function are plotted with a red line. d) FT of site energies. 63
5.6 a) Time series of T_{DA} of molecule D1 of **TCTA** with 10 neighbours (A1-A10). The value of T_{DA} is computed using the conformation at every 1 fs for 10 ps. b) Distribution of T_{DA}. c) $C_{T_{DA}}$. d) The black curve represents $C_{T_{DA}}$ of A1 calculated using the simulation data of T_{DA}. The red line obtained by the fit to the black line with use of a function made of single exponentials. 64
5.7 Time series of instantaneous Marcus rate (k_{ET}) of an individual molecule D1 of **TCTA** with 10 neighbours (A1-A10). The value of k_{ET} is computed using the conformation at every 1 fs for 10 ps. 66

6.1 Time series of site energy for five molecules (D1-D5) of CBP, p-BPD, TCTA and TPDI. 85
6.2 $C_{FC}(t) = \langle\langle \psi^D(t) \mid \psi^A(t)\rangle\rangle$ for five individual molecules (D1-D5) of CBP, p-BPD and TCTA. Single exponential fitting function plotted with a red line. 86
6.3 FT of site energies of CBP, p-BPD and TCTA. 87
6.4 Time series of electronic coupling of 5 individual molecules (D1-D5) of **CBP** with 10 neighbours (A1-A10). The value of T_{DA} is computed using the conformation at every 1 fs for 10 ps. 88
6.4 Time series of electronic coupling of 5 individual molecules (D1-D5) of **p-BPD** with 10 neighbours (A1-A10). The value of T_{DA} is computed using the conformation at every 1 fs for 10 ps. 89
6.4 Time series of electronic coupling of 5 individual molecules (D1-D5) of **TCTA** with 10 neighbours (A1-A10). The value of T_{DA} is computed using the conformation at every 1 fs for 10 ps. 90
6.4 Time series of electronic coupling of 5 individual molecules (D1-D5) of **TPDI** with 10 neighbours (A1-A10). The value of T_{DA} is computed using the conformation at every 1 fs for 10 ps. 91
6.5 $C_{T_{DA}}(t) = \langle T_{DA}(t)\, T_{DA}(0)\rangle$ for 5 CBP molecules (D1-D5). Single exponential fitting function plotted with a red line. 92
6.6 $C_{T_{DA}}(t) = \langle T_{DA}(t)\, T_{DA}(0)\rangle$ for 5 p-BPD molecules (D1-D5). Single exponential fitting function plotted with a red line. 93
6.7 Time series of instantaneous Marcus rate of 5 individual molecules (D1-D5) of **CBP** with 10 neighbours (A1-A10). The value of k_{ET} is computed using the conformation at every 1 fs for 10 ps. 95
6.7 Time series of instantaneous Marcus rate of 5 individual molecules (D1-D5) of **p-BPD** with 10 neighbours (A1-A10). The value of k_{ET} is computed using the conformation at every 1 fs for 10 ps. 96
6.7 Time series of instantaneous Marcus rate of 5 individual molecules (D1-D5) of **TCTA** with 10 neighbours (A1-A10). The value of k_{ET} is computed using the conformation at every 1 fs for 10 ps. 97

6.7 Time series of instantaneous Marcus rate of 5 individual molecules (D1-D5) of **TPDI** with 10 neighbours (A1-A10). The value of k_{ET} is computed using the conformation at every 1 fs for 10 ps. 98

List of Tables

4.1 Bond length alternation and dihedral angles for the CBP molecule optimized by various quantum chemistry methods. The bond length alternation is defined in Fig. 4.1b. . . . 37
4.2 Bond lengths and bond-length alternation (BLA) for the CBP molecule optimized by various quantum chemistry methods. . . . 38
4.3 Vertical excitation energies (eV) of fully optimized geometries in vacuum using various quantum chemistry methods. . . . 39
4.4 Bond lengths and bond-length alternation (BLA) for the constrained optimizations with the different methods. Bond length and BLA are given in Å. . . . 40
4.5 Vertical excitation energies (eV) of optimized CBP geometries in vacuum with constraint dihedral angles at 45°, 60° and 0° for α, β and γ. . . . 40
4.6 Excitation energies (in eV) of the lowest-energy peak in the gas-phase static absorption spectra for side α and central α and β dihedral angles from 0° to 90° in 10 degrees obtained using TD-LC-DFTB and GW-BSE (shown in parentheses). . . . 43

5.1 Fitted single exponential values of $C_{FC}(t)$. . . . 62
5.2 Fitted parameters for $C_{T_{DA}}$ using $y = A0 * exp(-x/A1) + A2$. . . . 65
5.3 $\langle T_{DA} \rangle$ (10^{-3} eV), $\sqrt{\langle T_{DA}^2 \rangle}$ (10^{-3} eV) and R_{coh} . . . 66
5.4 $\langle T_{DA} \rangle$ (10^{-3} eV), $\sqrt{\langle T_{DA}^2 \rangle}$ (10^{-3} eV) and R_{coh} . . . 66
5.5 $\langle T_{DA} \rangle$ (10^{-3} eV), $\sqrt{\langle T_{DA}^2 \rangle}$ (10^{-3} eV) and R_{coh} . . . 67
5.6 $\langle T_{DA} \rangle$ (10^{-3} eV), $\sqrt{\langle T_{DA}^2 \rangle}$ (10^{-3} eV) and R_{coh} . . . 67

6.1 Single exponential fitting values for site energy fluctuations. . . . 87
6.2 Fitting parameters for $\langle T_{DA}(t)\, T_{DA}(0) \rangle$ using $y = A0 * exp(-x/A1) + A2$ -CBP . . . 94
6.3 Fitting parameters for $\langle T_{DA}(t)\, T_{DA}(0) \rangle$ using $y = A0 * exp(-x/A1) + A2$ -p-BPD . . . 94
6.4 Fitting parameters for $\langle T_{DA}(t)\, T_{DA}(0) \rangle$ using $y = A0 * exp(-x/A1) + A2$ -TCTA . . . 94

6 Appendix

6.1 Site energy (ϵ_i)

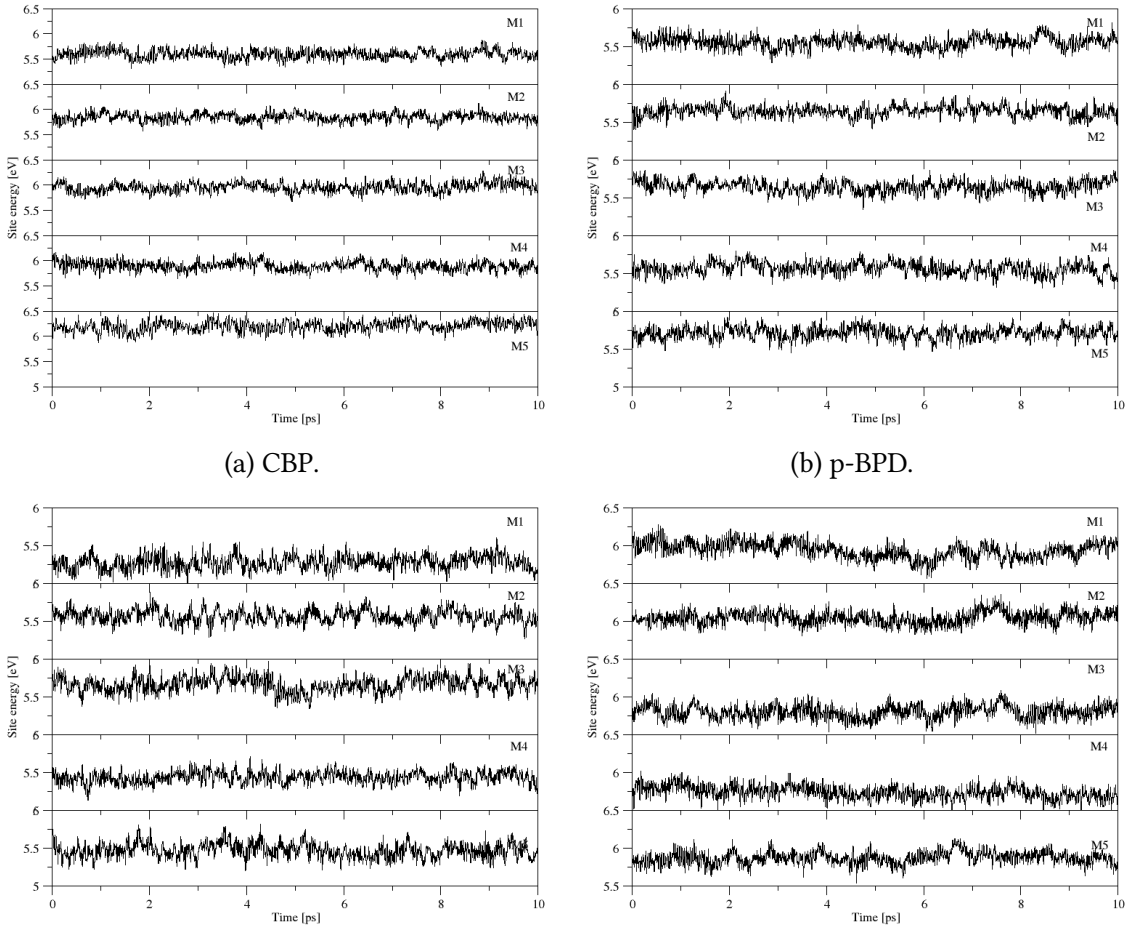

(a) CBP.

(b) p-BPD.

(c) TCTA.

(d) TPDI.

Figure 6.1: Time series of site energy for five molecules (D1-D5) of CBP, p-BPD, TCTA and TPDI.

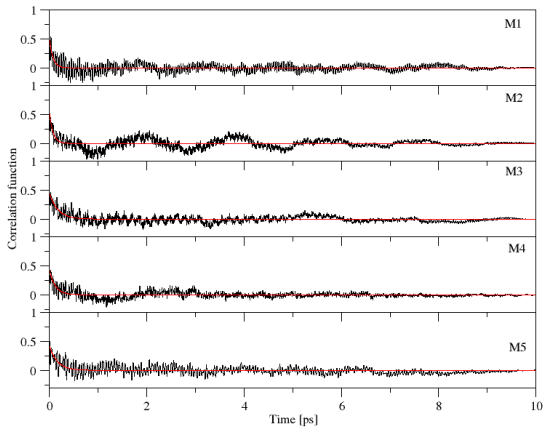

(a) CBP.

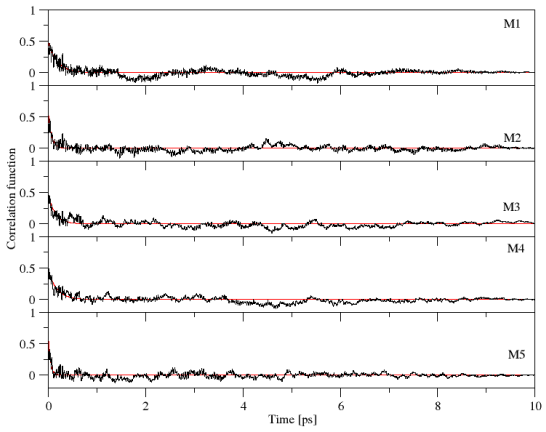

(b) p-BPD.

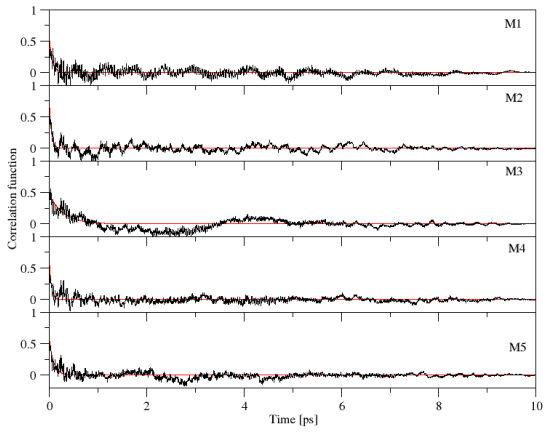

(c) TCTA.

Figure 6.2: $C_{FC}(t) = \langle\langle \psi^D(t) \mid \psi^A(t) \rangle\rangle$ for five individual molecules (D1-D5) of CBP, p-BPD and TCTA. Single exponential fitting function plotted with a red line.

Table 6.1: Single exponential fitting values for site energy fluctuations.

		A_0	A_1	A_2	Correlation coefficient
CBP	D1	0.550973	71.6265	5.43543e-06	0.473797
	D2	0.590564	73.42	1.98853e-09	0.454203
	D3	0.459157	175.34	4.65848e-07	0.652551
	D4	0.454901	117.094	2.01818e-08	0.603395
	D5	0.43841	164.415	2.62047e-10	0.557034
p-BPD	D1	0.493513	184.814	2.78567e-08	0.711653
	D2	0.600389	65.123	4.88144e-10	0.63341
	D3	0.47121	148.034	1.22191e-10	0.673293
	D4	0.472653	177.893	2.94448e-11	0.727724
	D5	0.693888	43.5723	4.5524e-10	0.655280
TCTA	D1	0.597222	62.7551	3.39337e-10	0.542082
	D2	0.829677	41.8224	7.27016e-11	0.623581
	D3	0.47053	296.248	1.82471e-10	0.677689
	D4	0.704801	41.0612	5.60474e-11	0.618929
	D5	0.602502	88.2157	6.0544e-11	0.689138

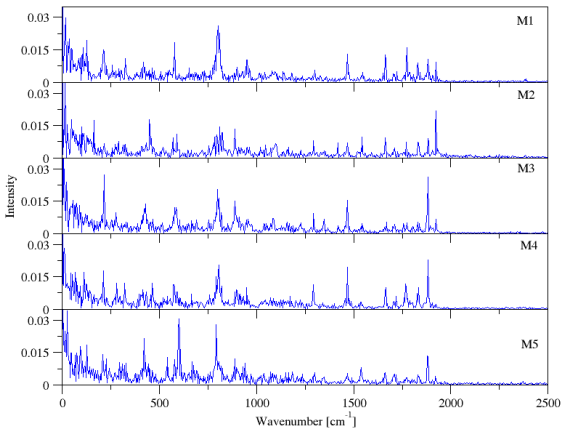

(a) **CBP**

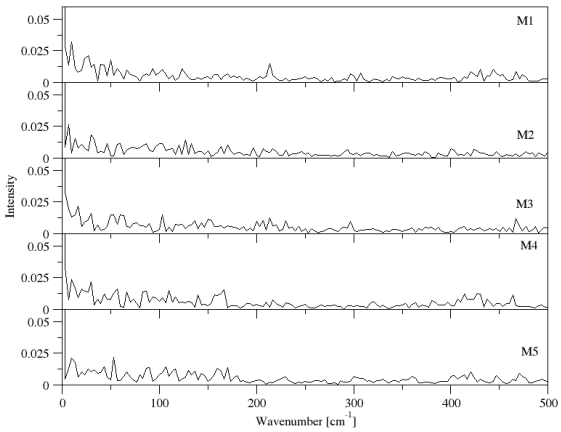

(b) **p-BPD**

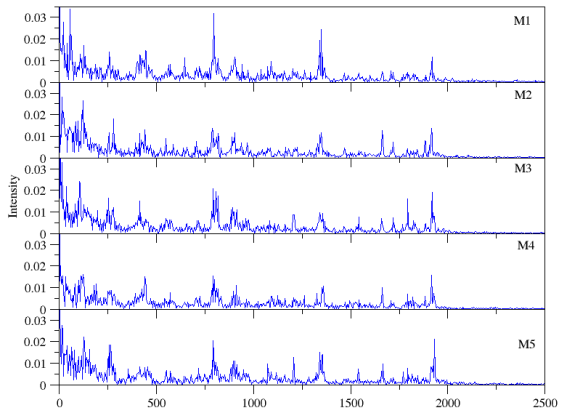

(c) **TCTA**

Figure 6.3: FT of site energies of CBP, p-BPD and TCTA.

6.2 Electronic coupling (T_{DA})

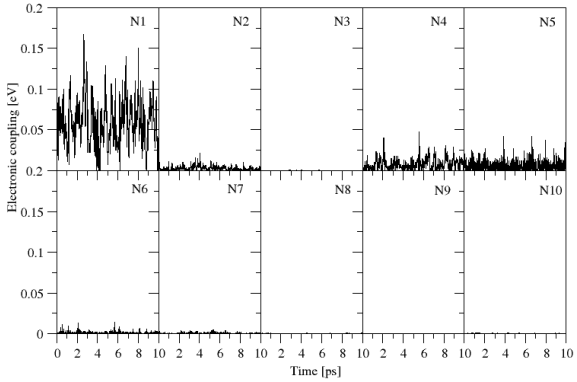

(a) CBP-D1.

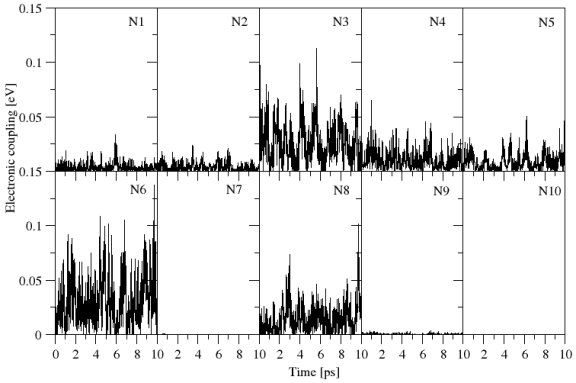

(b) CBP-D2.

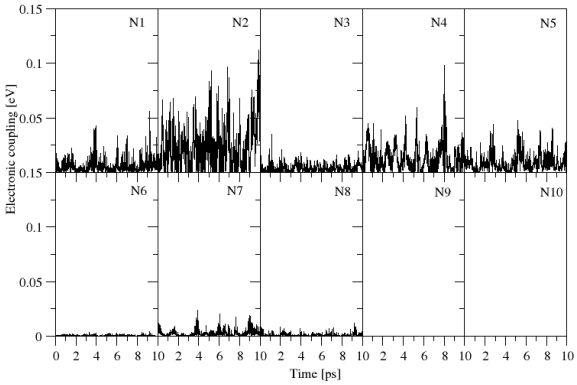

(c) CBP-D3.

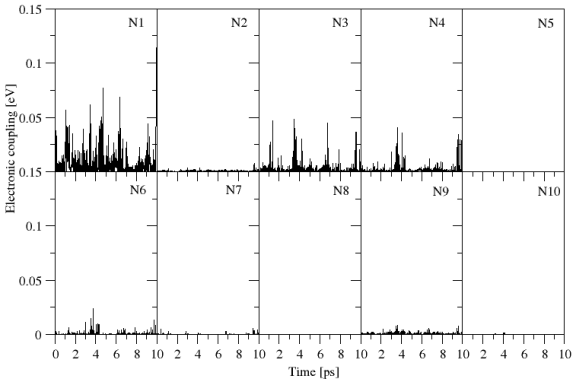

(d) CBP-D4.

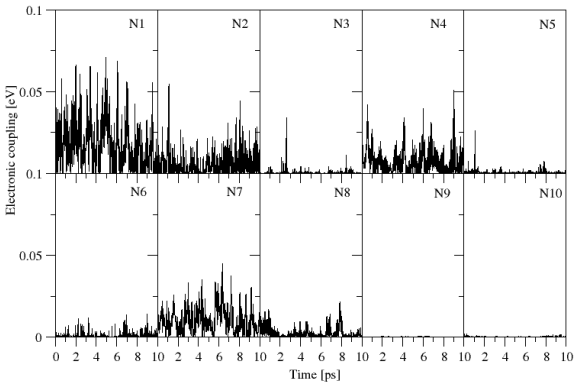

(e) CBP-D5.

Figure 6.4: Time series of electronic coupling of 5 individual molecules (D1-D5) of **CBP** with 10 neighbours (A1-A10). The value of T_{DA} is computed using the conformation at every 1 fs for 10 ps.

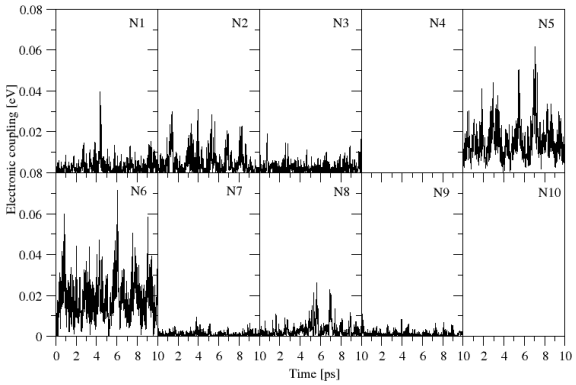

(f) p-BPD-D1.

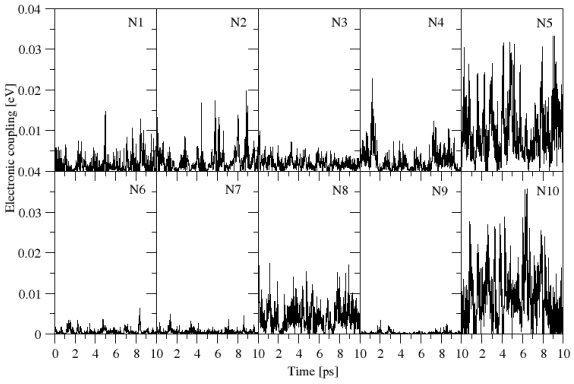

(g) p-BPD-D2.

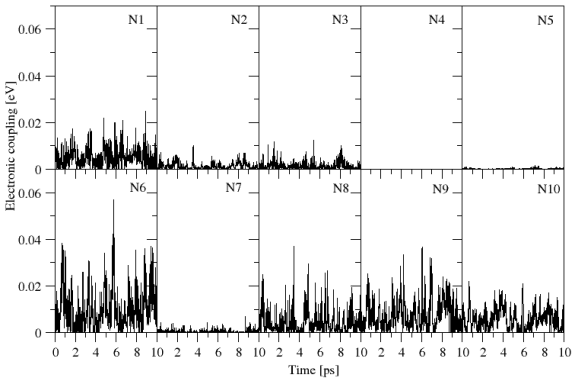

(h) p-BPD-D3.

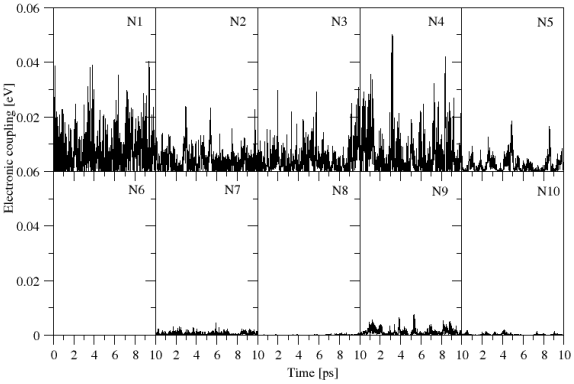

(i) p-BPD-D4.

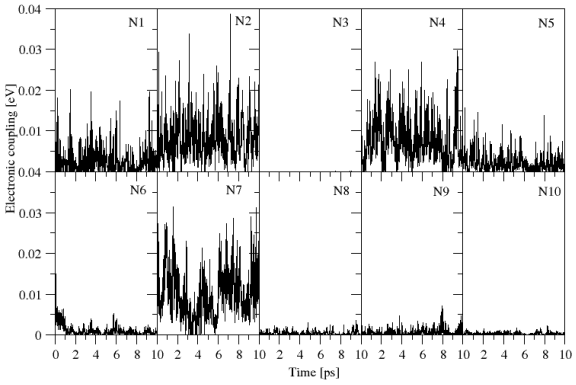

(j) p-BPD-D5.

Figure 6.4: Time series of electronic coupling of 5 individual molecules (D1-D5) of **p-BPD** with 10 neighbours (A1-A10). The value of T_{DA} is computed using the conformation at every 1 fs for 10 ps.

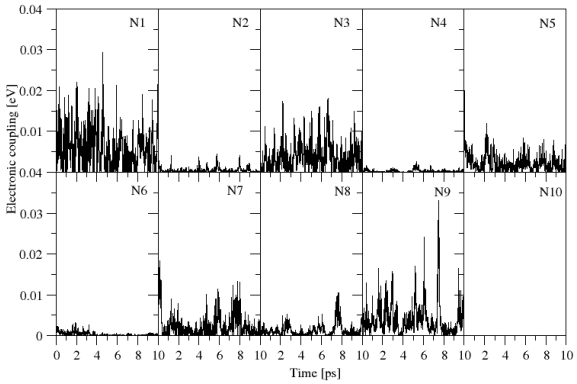

(k) TCTA-D1.

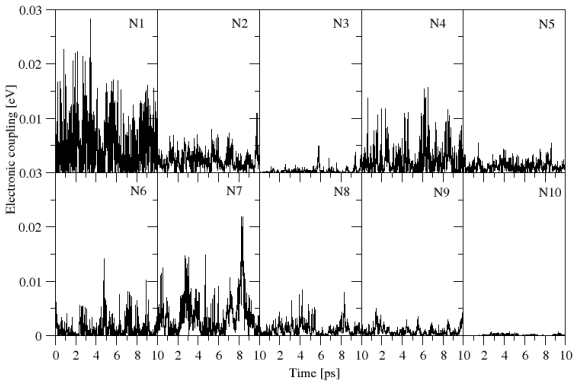

(l) TCTA-D2.

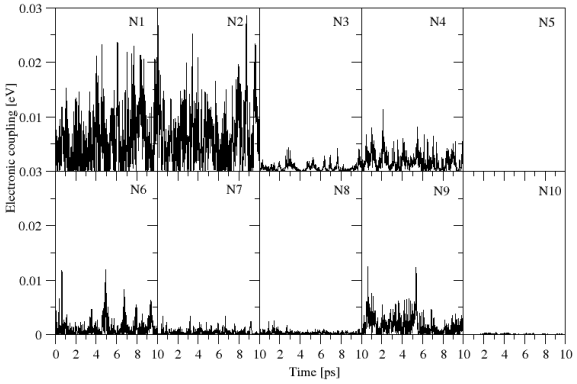

(m) TCTA-D3.

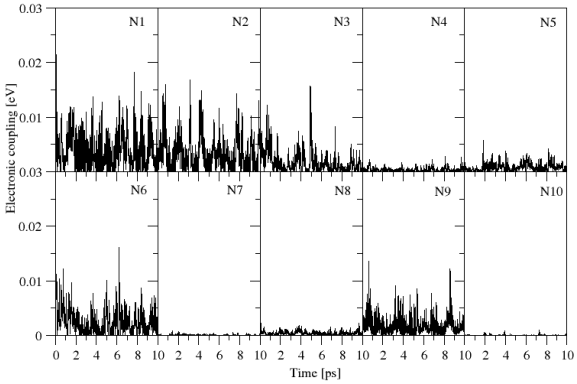

(n) TCTA-D4.

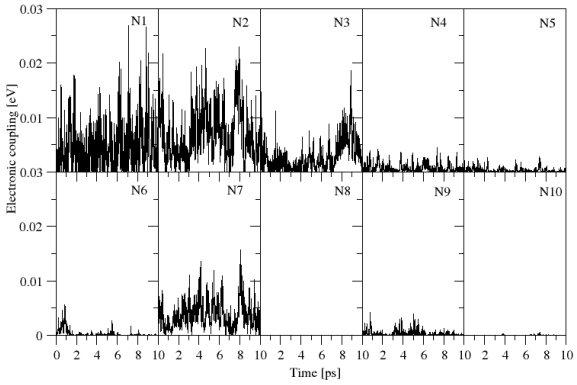

(o) TCTA-D5.

Figure 6.4: Time series of electronic coupling of 5 individual molecules (D1-D5) of **TCTA** with 10 neighbours (A1-A10). The value of T_{DA} is computed using the conformation at every 1 fs for 10 ps.

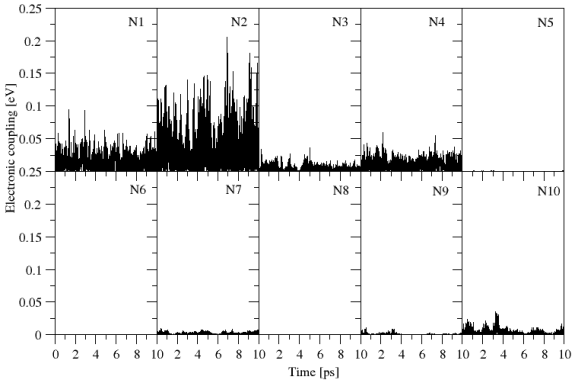

(p) TPDI-D1.

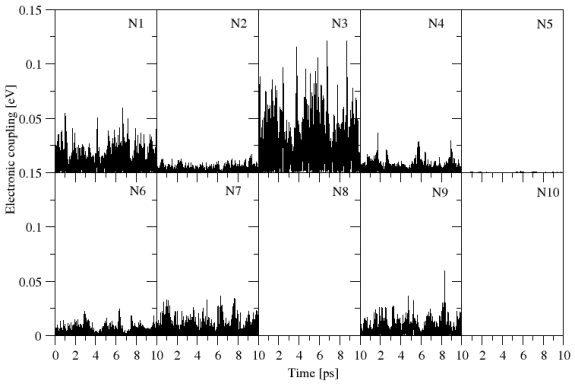

(q) TPDI-D2.

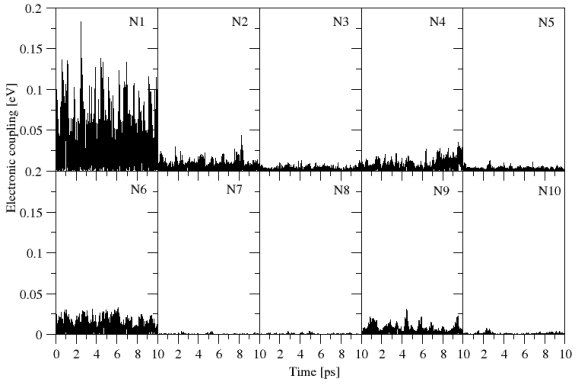

(r) TPDI-D3.

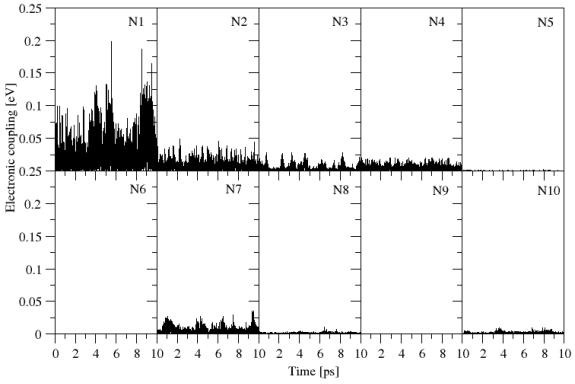

(s) TPDI-D4.

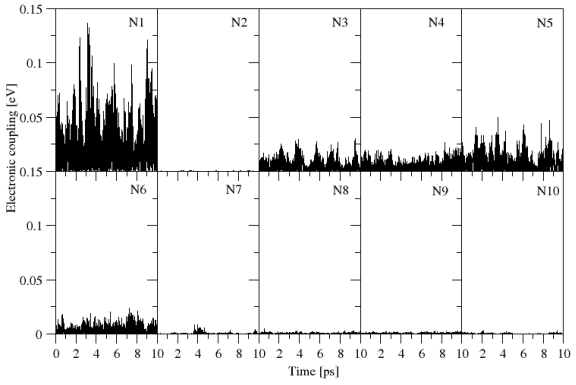

(t) TPDI-D5.

Figure 6.4: Time series of electronic coupling of 5 individual molecules (D1-D5) of **TPDI** with 10 neighbours (A1-A10). The value of T_{DA} is computed using the conformation at every 1 fs for 10 ps.

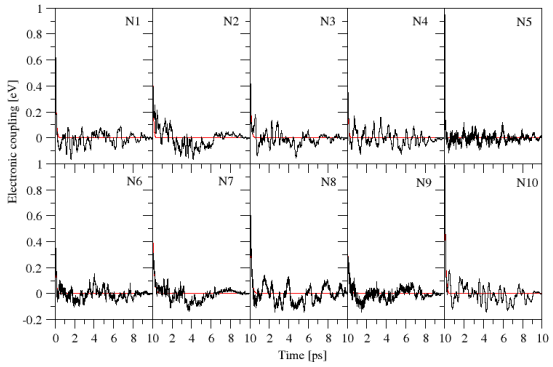

(a) D1.

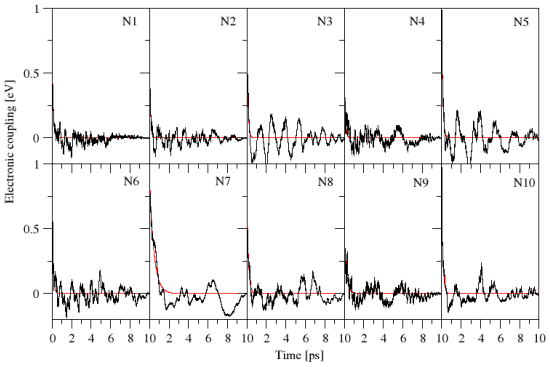

(b) D2.

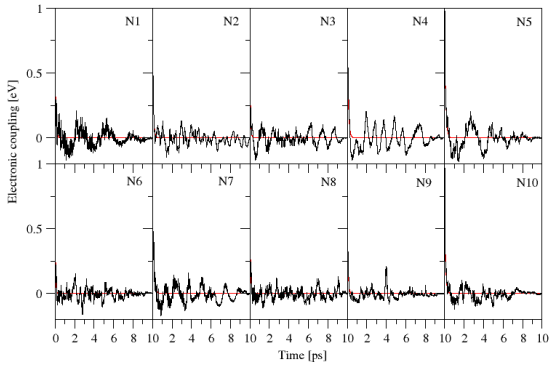

(c) D3.

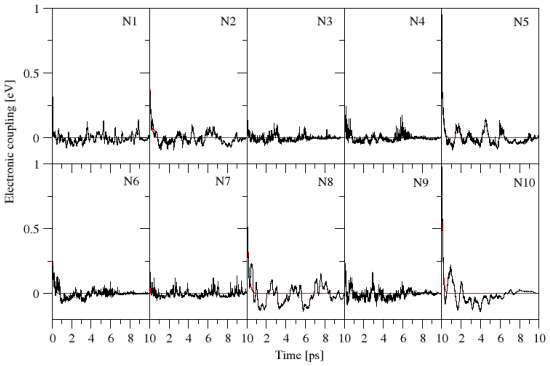

(d) D4.

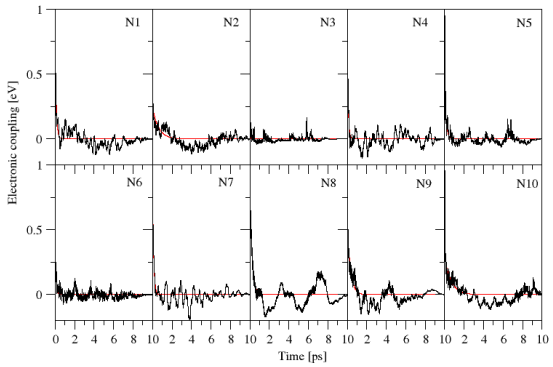

(e) D5.

Figure 6.5: $C_{T_{DA}}(t) = \langle T_{DA}(t)\, T_{DA}(0) \rangle$ for 5 CBP molecules (D1-D5). Single exponential fitting function plotted with a red line.

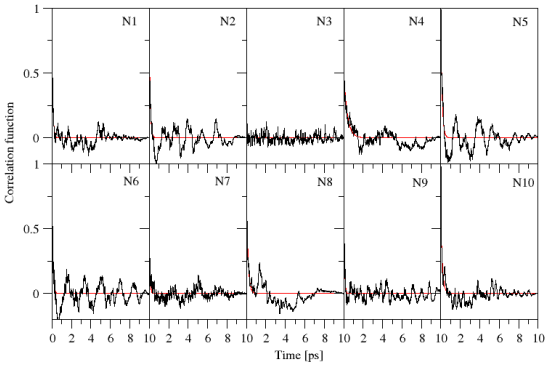

(a) D1.

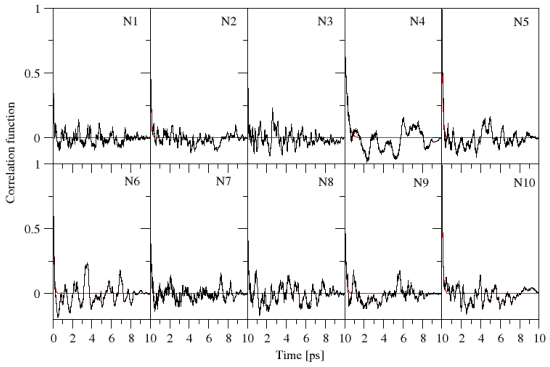

(b) D2.

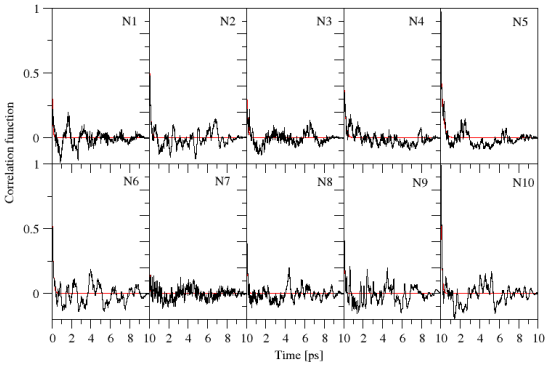

(c) D3.

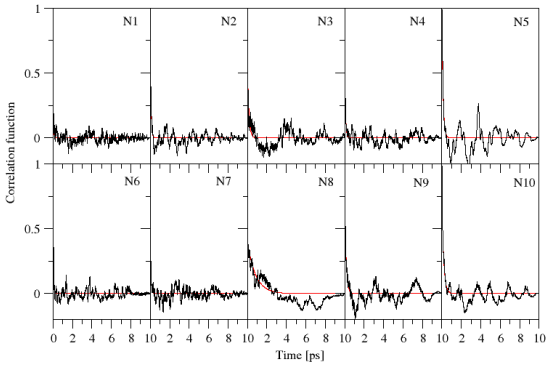

(d) D4.

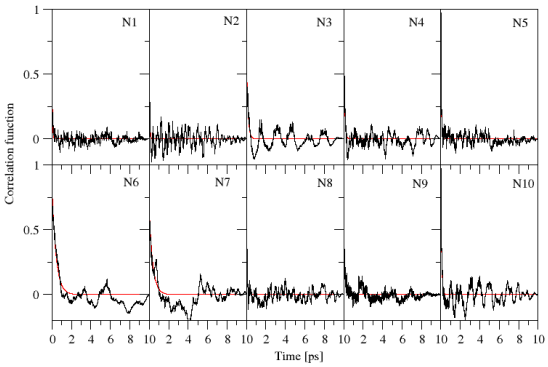

(e) D5.

Figure 6.6: $C_{T_{DA}}(t) = \langle T_{DA}(t)\, T_{DA}(0) \rangle$ for 5 p-BPD molecules (D1-D5). Single exponential fitting function plotted with a red line.

Table 6.2: Fitting parameters for $\langle T_{DA}(t)\, T_{DA}(0)\rangle$ using $y = A0 * exp(-x/A1) + A2$ -CBP

			A_0	A_1	A_2	Correlation coefficient
CBP	D1	A1	0.999238	77.1032	3.54788e-07	0.821288
		A2	0.999192	64.4403	1.53012e-08	0.652003
		A3	0.881951	83.7292	2.47722e-10	0.770008
		A4	0.999694	64.3133	7.50793e-11	0.753685
		A5	0.755422	33.554	5.70966e-08	0.699050
		A6	0.716209	72.5366	5.73534e-11	0.755159
		A7	0.595452	139.557	1.27178e-09	0.769938
		A8	0.909583	117.135	1.67013e-10	0.764032
		A9	0.482154	137.959	1.72087e-09	0.709445
		A10	0.994902	86.5269	3.33347e-09	0.765309

Table 6.3: Fitting parameters for $\langle T_{DA}(t)\, T_{DA}(0)\rangle$ using $y = A0 * exp(-x/A1) + A2$ -p-BPD

			A_0	A_1	A_2	Correlation coefficient
p-BPD	D1	A1	0.782436	93.2935	3.73994e-08	0.796140
		A2	0.832813	101.413	2.82906e-11	0.693034
		A3	0.938295	27.6096	4.41127e-06	0.761652
		A4	0.517111	361.884	1.91929e-10	0.845337
		A5	0.892454	133.333	8.90922e-11	0.713302
		A6	0.850954	93.8256	3.54007e-11	0.635665
		A7	0.629614	68.3761	1.29324e-10	0.706607
		A8	0.845197	155.672	2.28237e-11	0.771248
		A9	0.805421	73.8767	3.10905e-10	0.774406
		A10	0.577905	166.991	3.39247e-11	0.764205

Table 6.4: Fitting parameters for $\langle T_{DA}(t)\, T_{DA}(0)\rangle$ using $y = A0 * exp(-x/A1) + A2$ -TCTA

			A_0	A_1	A_2	Correlation coefficient
	D1	A1	0.911871	55.6189	1.87199e-10	0.695020
		A2	0.914399	89.8389	3.13798e-11	0.774433
		A3	0.815112	89.0426	3.459e-10	0.711222
		A4	0.956006	187.095	0.717928	0.717928
		A5	0.779408	139.676	1.28214e-10	0.833046
		A6	0.60339	1075.04	2.35593e-11	0.889891
		A7	0.884397	157.034	6.52334e-11	0.765733
		A8	0.9998	191.725	1.16039e-11	0.813569
		A9	0.9988	94.8061	3.97463e-11	0.771426
		A10	0.999999	94.8061	4.93932e-07	0.777399

6.3 Instantaneous Marcus rate

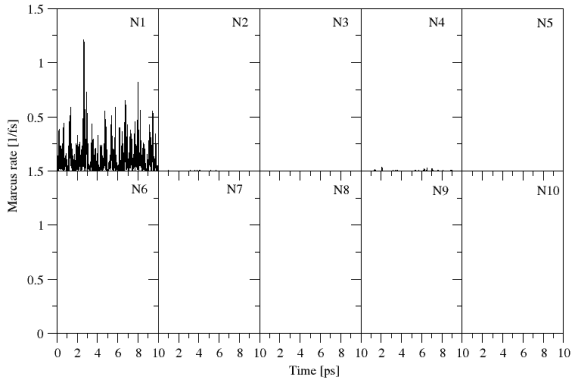

(a) CBP-D1.

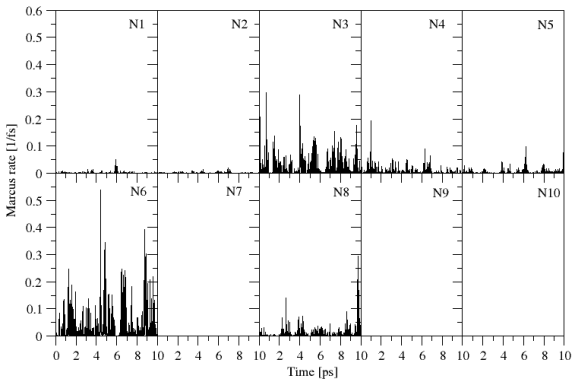

(b) CBP-D2.

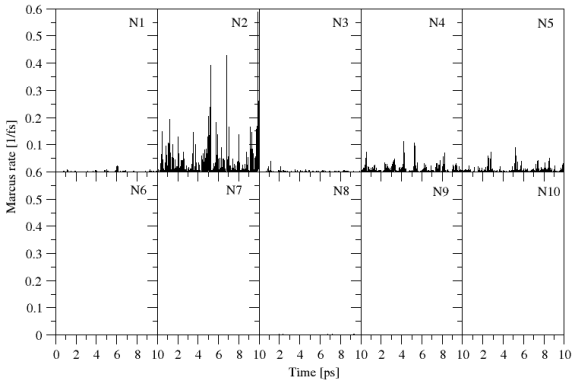

(c) CBP-D3.

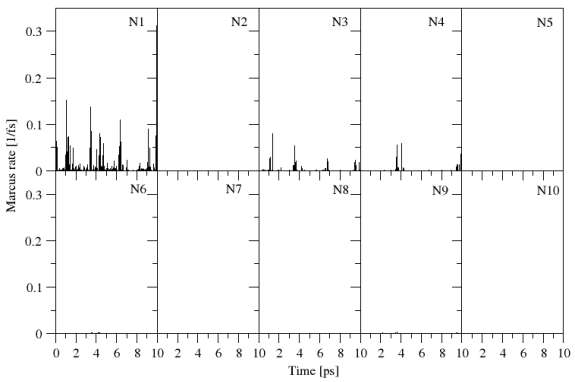

(d) CBP-D4.

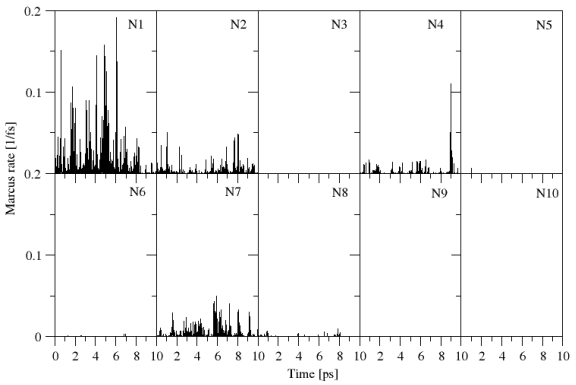

(e) CBP-D5.

Figure 6.7: Time series of instantaneous Marcus rate of 5 individual molecules (D1-D5) of **CBP** with 10 neighbours (A1-A10). The value of k_{ET} is computed using the conformation at every 1 fs for 10 ps.

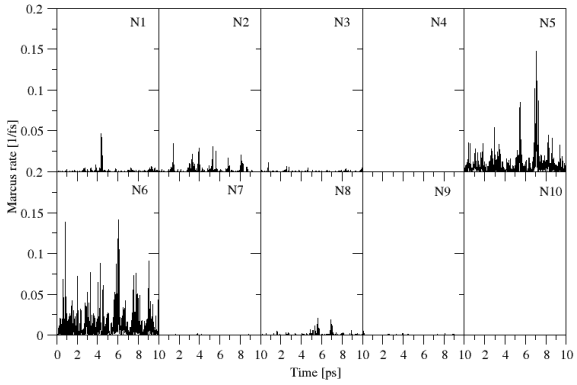

(f) p-BPD-D1.

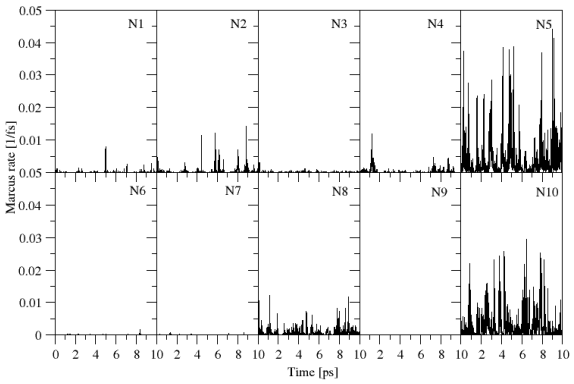

(g) p-BPD-D2.

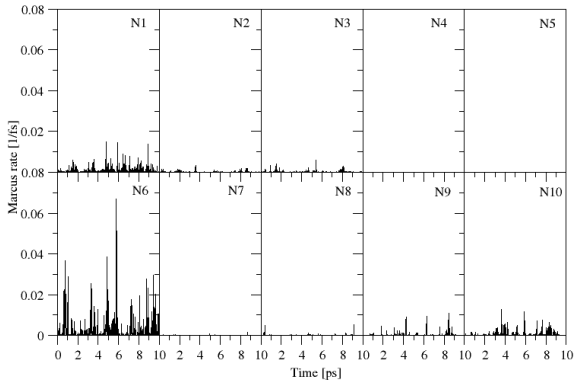

(h) p-BPD-D3.

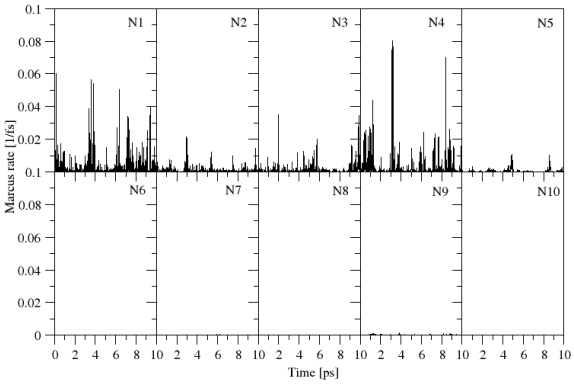

(i) p-BPD-D4.

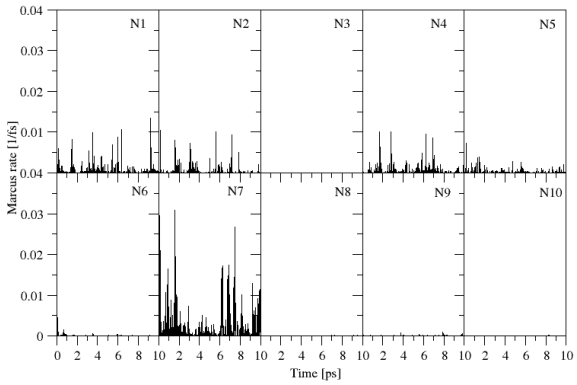

(j) p-BPD-D5.

Figure 6.7: Time series of instantaneous Marcus rate of 5 individual molecules (D1-D5) of **p-BPD** with 10 neighbours (A1-A10). The value of k_{ET} is computed using the conformation at every 1 fs for 10 ps.

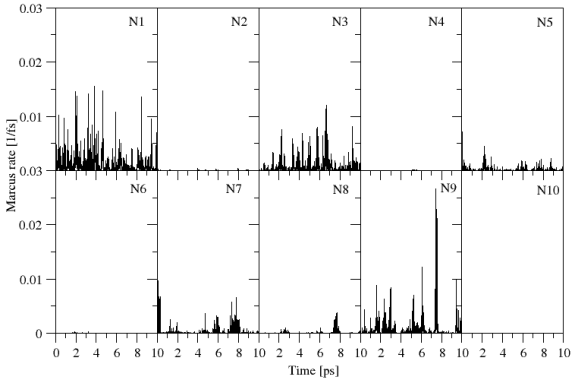

(k) TCTA-D1.

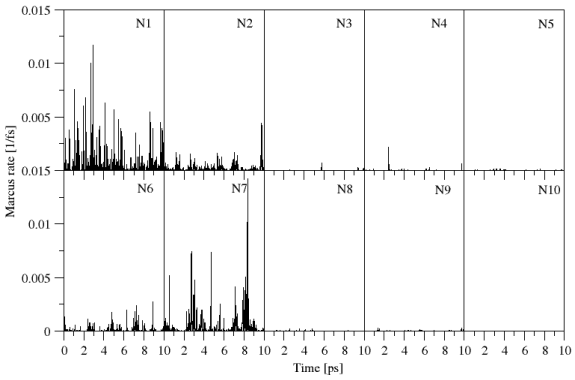

(l) TCTA-D2.

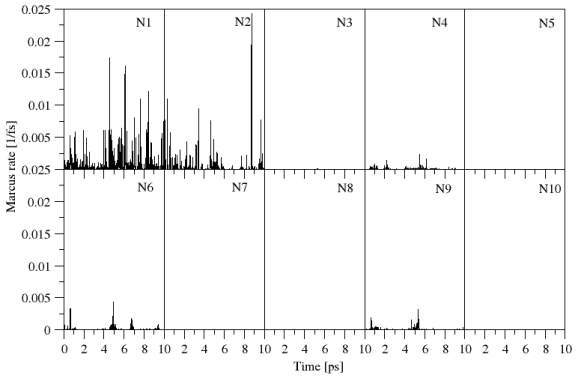

(m) TCTA-D3.

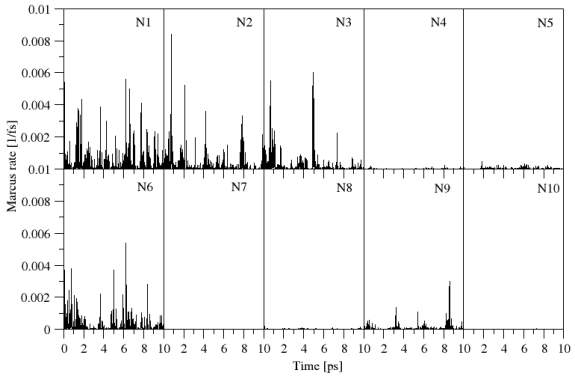

(n) TCTA-D4.

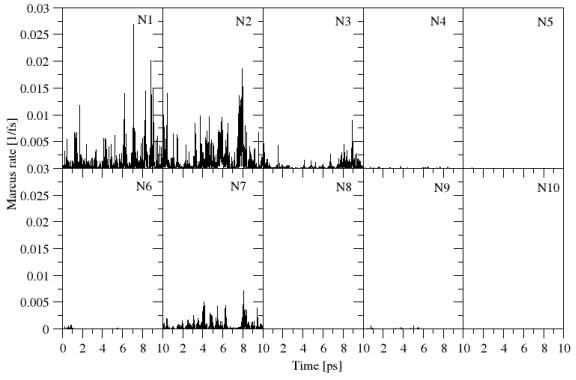

(o) TCTA-D5.

Figure 6.7: Time series of instantaneous Marcus rate of 5 individual molecules (D1-D5) of **TCTA** with 10 neighbours (A1-A10). The value of k_{ET} is computed using the conformation at every 1 fs for 10 ps.

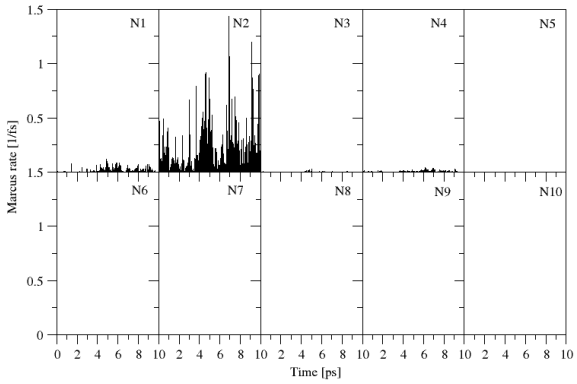

(p) TPDI-D1.

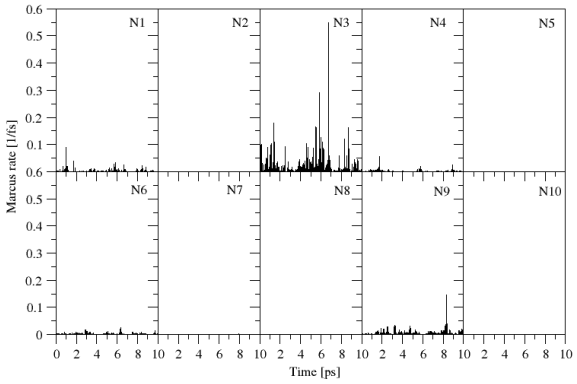

(q) TPDI-D2.

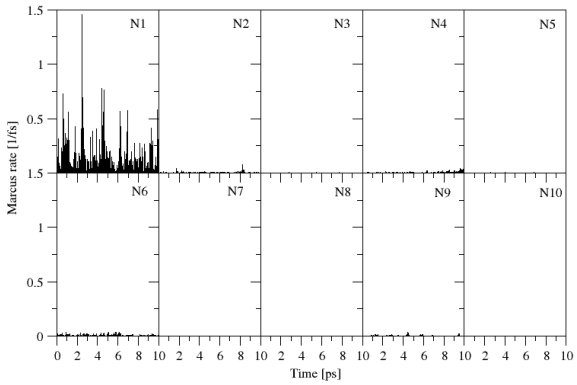

(r) TPDI-D3.

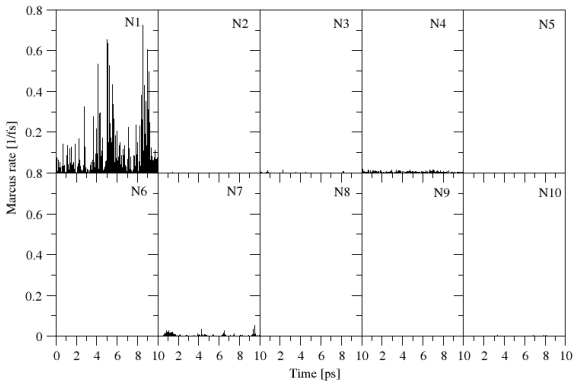

(s) TPDI-D4.

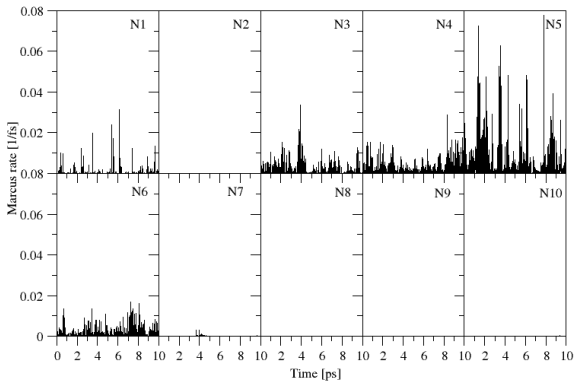

(t) TPDI-D5.

Figure 6.7: Time series of instantaneous Marcus rate of 5 individual molecules (D1-D5) of **TPDI** with 10 neighbours (A1-A10). The value of k_{ET} is computed using the conformation at every 1 fs for 10 ps.